Interner Bericht

DLR-IB-SY-BS-2026-44

Funktionsnachweis eines Klebstoffsystems zur inhärenten Strukturüberwachung von strukturellen Klebverbindungen

Masterarbeit

Lukas Hampel

Deutsches Zentrum für Luft- und Raumfahrt

Institut für Systemleichtbau

Deutsches Zentrum
DLR für Luft- und Raumfahrt

Dokumenteigenschaften

Titel	Funktionsnachweis eines Klebstoffsystems zur inhärenten Strukturüberwachung von strukturellen Klebverbindungen
Betreff	Masterarbeit
Institut	Systemleichtbau
Erstellt von	Lukas Hampel
Beteiligte	Dr.-Ing. Maximilian Jux; Vinzenz Ginster, M. Sc.
Geprüft von	Prof. Dr.-Ing. Uwe Reisgen
Freigabe von	Prof. Dr.-Ing. Peter Wierach
Zugänglichkeit	☒ Stufe 1: Allgemein zugänglich (in elib ohne Zugangsbeschränkung)
	☐ Stufe 2: DLR intern zugänglich (in elib mit Beschränkung „nur DLR-intern zugänglich“)
Datum	11.05.2026
Version	1.0
Datei Info	IB_2026_44_MA_Hampel.pdf

Diese Arbeit wurde vorgelegt am Institut für Schweißtechnik und Fügetechnik

Funktionsnachweis eines Klebstoffsystems zur inhärenten Strukturüberwachung von strukturellen Klebverbindungen

Performance verification of an adhesive system for inherent structural monitoring of structural adhesive bonds

Masterarbeit

des Herrn Lukas Hampel

Matrikelnummer: 392005

Institutsleiter: Univ.- Prof. Dr.-Ing. U. Reisgen

Betreuer: Vinzenz Ginster, M.Sc.

Betreuer: Maximilian Jux, Dr.

Aachen, im May 2026

Abstract

The objective of this work is to determine the effect various metal mesh geometries have on bond strength, as well as determining if damage can be detected and localized within an adhesive layer using resistance measurements. The parameters of open area, wire diameter and wire material were investigated. Open area does not influence bond strength, while there is an inverse relationship between wire diameter and bond strength. The young's module is directly related to bond strength. The electrical resistance measurements showed that large adhesive, cohesive and mixed damage which covers the area of the entire contact can be identified. The multiplexer system which might be used for the development of a structural health monitoring system was also shown to be able to detect damage, and possible improvements were identified.

Keywords: Modified adhesive, Damage detection, Damage localization, Carbon based nanoparticles, Resistive measurement, embedded metal mesh

I. Table of Contents

II. List of Figures

III. List of Tables

IV. **Abbreviations**

Adh	Adhesive failure
Al	Aluminium
ASTM	American Society for Testing and Materials
CF	Carbon fiber
CFRP	Carbon fiber reinforced polymer
CNT	Carbon nano tubes
Co	Cobalt
Coh	Cohesive failure
Cr	Chromium
Cu	Copper
DCB	Double cantilever beam
DIN	Deutschen Instituts für Normung
DLR	Deutsches Zentrum für Luft- und Raumfahrt e. V.
DSC	Differential Scanning Calorimetry
EDX	Energy-dispersive X-ray spectroscopy
GF	Glass fiber
GFRP	Glass fiber reinforced polymer
LSS	Lap shear strength
Mix	Mixed failure
MUX	Multiplexer
MWCNT	Multiwall carbon nanotubes
NDT	Non-destructive testing methods
Ni	Nickel
PCB	Printed circuit board
PEEK	Polyetheretherketon
PEI	Polyethylenimin
PETG	Polyethylene terephthalate glycol
PPS	Polyphenylensulfid
SEM	Scanning electron microscope
SHM	Structrual health monitoring
SLS	Single lap shear
SN- Curve	Wöhler Curve
SS	Stainless steel
TGA	Thermogravimetric analysis
VARI	Vacuum assisted resin infusion

V. Formula Symbols

a	Crack length	mm
A_{open}	Open area of the Mesh	mm^2
A_{total}	Area of one	mm^2
d	Wire diameter	mm
d	Displacement at crack delamination onset	mm
E	E-Modul or young's module	Mpa
G_{IIC}	Fracture toughness	J/mm^2
L	Span length	mm
m	Slope of force displacement graph	N/mm
mw	Mesh width	mm
p	Critical load for crack initiation	N
p	Pearson correlation value	-
r	Residual	-
R_1	Resistance of measurement path	Ω
R_{ref}	Reference resistance	Ω
R_x	Resistance of reference resistor	Ω
SE	Standard error	-
t	Sample thickness	mm
U	Voltage of measurement system	V
U_x	Voltage across reference resistor	V
w	Width of sample	mm

1 Introduction

Large composite structures have become increasingly important in the aerospace industry due to their high specific stiffness, low weight, excellent fatigue resistance, and corrosion resistance [Pal93, SR05]. Modern aircraft rely extensively on bonded composite components such as shells, spars, stringers, and ribs to achieve improved aerodynamic efficiency, reduced fuel consumption, and lower direct operating costs [KZM08, Lei23]. However, these lightweight structures are subjected to complex operational loads and harsh environmental conditions throughout their service life, making reliable structural integrity assessment a major engineering challenge. Conventional inspection methods are often labor-intensive, require significant downtime, and are difficult to apply to inaccessible bonded interfaces. Consequently, structural health monitoring (SHM) systems have received increasing attention in aerospace applications as a means of enabling continuous condition monitoring, early damage detection, and condition-based maintenance [RSN21]. Studies report that SHM systems may reduce aircraft direct operating costs by up to 5 % through optimized maintenance procedures and reduced inspection requirements [CCM22].

One industry that faces similar pressures to adopt SHM system is the wind energy sector. Wind energy has developed into one of the most important renewable energy technologies worldwide and is a key component in the transition toward sustainable and low-carbon energy systems. In 2025, global wind power generation reached nearly 3000 TWh, supplying more than 11 % of worldwide electricity demand, while annual installation growth reached its highest rate since 2020 [Wor26]. In addition, this accounted for 23 % of all newly installed electricity generation capacity in 2025 [FSA+26]. This expansion has been driven largely by rapid developments in turbine technology and increasing deployment of large-scale offshore and onshore wind farms.

As modern wind turbines continue to increase in size and power output, the structural demands placed on their components also increase significantly. Like airplane wings, rotor blades are subjected to complex cyclic loading, environmental degradation, and dynamic stresses throughout their service life. Studies have shown that rotor blades experience an average annual failure rate of approximately 0.1 failures per turbine [KVD+11]. Furthermore, reliability studies indicate that increasing turbine size is often accompanied by higher downtime and reduced reliability [LFH+09]. The economic consequences of such failures are substantial, as each day during which a turbine remains out of operation can result in revenue losses between $800 and $1600 depending on local wind conditions and power production potential [KPN21]. Consequently, minimizing downtime and enabling early damage detection are of considerable importance for the wind energy industry.

Current SHM systems for large composite structures are still limited in their ability to identify the exact cause and type of structural damage. The aerospace structures and wind turbine blades must withstand high operational loads over long service lifetimes while operating with minimal inspection access. At the same time, operators seek to reduce maintenance costs by extending inspection intervals and relying increasingly on remote monitoring technologies. Modern SHM systems combine integrated sensing technologies with advanced data analysis methods to monitor structural integrity during operation. These systems can support damage detection, localization, and maintenance planning while reducing inspection effort and operational interruptions [SN25], but they often cannot distinguish between different failure mechanisms.

Particular attention must therefore be given to adhesive bond lines, which represent critical interfaces within composite structures. One promising approach for monitoring such bonds is the use of electrically conductive adhesives in combination with embedded electrical contacts. By measuring changes in electrical resistance, it becomes possible to monitor crack initiation and crack propagation within the adhesive layer. Research conducted at the Deutsches Zentrum für Luft- und Raumfahrt e. V. (DLR) developed an adhesive with an electrical conductivity of approximately 0.1 S/m, slightly above the percolation threshold, and initial studies have characterized its electrical and mechanical behavior [Mar25, Zel23]. However, the influence of embedded electrical contact systems on the mechanical performance of the adhesive bond has not yet been fully investigated.

An attractive candidate for such embedded contact systems are metallic meshes, similar to those already used in aerospace applications for lightning strike protection [SAE16]. These conductive meshes are well suited for integration into composite laminate structures and could potentially provide both electrical conductivity for SHM and sufficient mechanical durability under operational loading conditions. Nevertheless, the effect of different mesh geometries and material properties on adhesive bond strength remains insufficiently understood. Accordingly, this thesis investigates the influence of parameters such as wire diameter, open area, and mesh material on the mechanical properties of bonded joints. In addition, the work examines whether different failure modes — including adhesive, cohesive, and mixed failures — produce distinguishable electrical resistance responses, thereby enabling not only damage detection but also failure mode identification and localization within adhesive layers.

2 Basic Principles

In this chapter, the fundamental principles required to understand the investigations in this work are introduced. It begins with an overview of adhesive types, with particular emphasis on epoxy resins and their characteristics. The mechanisms of adhesion and cohesion are then explained, alongside typical fracture patterns observed in bonded joints. Building on this, structural health monitoring (SHM) and relevant damage detection methods are presented. To support this understanding, key concepts such as stress concentrations and fatigue are briefly discussed. Finally, the application context is established through an overview of wind turbine blades, including the loads they experience and the common types of damage observed in service.

2.1 Adhesives

2.1.1 Types of Adhesives

Polymers can be categorized into elastomers, thermoplastics and thermosets also known as duroplasts. Cross-links are molecular bonds between different polymer chains. The different polymer groups have varying amounts of cross-links which decrease the movement of these chains changing their mechanical characteristics and making them desirable for different applications. Thermoplastics are linear or slightly branched polymers that do not cross-link, allowing them to melt and solidify repeatedly without breaking down. This characteristic leads to high flexibility. Parallel molecules of thermoplastics can form many intermolecular bonds, such regions are called crystalline. Regions where the molecules are randomly ordered are called amorphous. Due to the high number of intermolecular bonds the crystalline regions have higher elastic moduli however, they also have lower impact resistance because the molecules cannot slide past each other as easily. Elastomers are polymers which have a small number of cross-links allowing them to quickly return to their original shape at room temperature. Some elastomers can form a crystalline phase. Partially crystalline elastomers usually have a higher elastic modulus but exhibit lower deformation, while Thermosets have a high number of cross-links. The polymer chains are completely restricted from moving making these adhesives stiff. Thermosets do not melt, instead the molecular bonds begin to break down at high temperatures. Due to their high strengths and low deformations, thermosets include the category of structural adhesives. [Hab16]

2.1.2 Epoxy Resin

Epoxy resin adhesives are produced by mixing of a resin (part A) component with a hardener (part B), curing through polyaddition to form thermosets at room temperature or higher. Part A contains an epoxide group that reacts with the amine group of part B, as displayed in Figure

2-1. They are often used in the automotive, aerospace, and electronic industries as well as to produce composite materials. Epoxy resins exhibit high moisture resistance, good ageing characteristics, and can adhere well to most materials. Due to high cross-linking, the adhesives maintain high strength even under thermal stress. However, due to the high cross-links leading to low deformability bending strength is reduced. [Hab16]

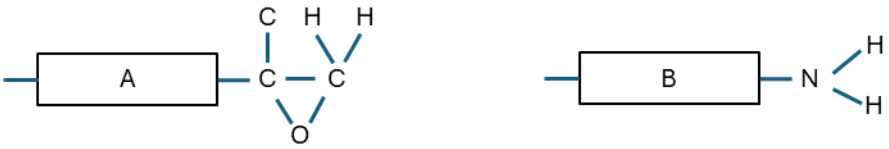

Figure 2-1 – Chemical structure of epoxide- and amine groups after [Hab16]

2.1.3 Binding forces: Cohesion and Adhesion

Adhesion and cohesion are two key phenomena that explain how adhesives work. For an adhesive to perform well, it must strike a balance between the adhesion and cohesion forces. Excessive adhesion without sufficient cohesion can cause the adhesive to break apart internally, leading to bond failure. Conversely, excessive cohesion without adequate adhesion means the adhesive will not adhere effectively to the surfaces. These properties lead to the different fracture patterns described in section 2.1.4.

Adhesion refers to the processes and mechanisms by which the adhesive sticks to the surfaces to which it is applied to. Multiple adhesion mechanics exist, the first being mechanical clamping of the adhesive to the bonding surface. In this explanation of adhesion, the rough surface of the bonded material hooks onto the adhesive resulting in the bond. This works to explain adhesion for materials such as wood and ceramics, where the adhesive can penetrate the porous material to hook onto or diffuse into it. For materials with smooth, non-porous surfaces, this is insufficient to create meaningful strength. This is where the phenomenon of chemical adhesion becomes crucial. [Hab16]

Adhesive forces arise from the intermolecular forces, also known as secondary bonds between the molecules of the adhesive and the surface. In polymers, specifically the group of forces known as van der Waals forces is responsible for adhesion. These forces are formed between the positively charged side of one molecule and the negatively charged side of another. These dipole-dipole bonds are weaker than the ionic and covalent bonds between atoms in molecules. The London dispersion forces, one of the van der Waals forces, have a dissociation energy of a few $kJmol^{-1}$, while hydrogen bonds range from 10 to 40 $kJ\ mol^{-1}$ though they do not form

between adhesive and metals. Covalent bonds have dissociation energies in the range from 300 to 500 kJ mol^{-1} [GH19]. The van der Waals forces do not require a chemical reaction between the molecules to form, meaning they can occur between two very flat, finely polished pieces of metal or the adhesive and substrate. [Doo18, GH19, Hab16]

Dipole-dipole forces can only form between molecules very close together and are weak. Therefore, it is usually necessary to have a large surface area for the adhesive to bond with the adherent, for a strong connection. The geometric surface area refers to the area of the flat bonding surface. To increase the surface area of the material it can be roughened through various methods such as mechanical (grinding, brushing or blasting treatment), chemical, laser or plasma processes [Thu20]. This creates a microscopic mountain-like surface whose total area is the true surface area. The adhesive should be viscous enough and have appropriate surface tension and surface energy to flow into these gaps and adhere to the surfaces. This phenomenon is called wetting; the area formed through wetting is referred to as the working surface area. By optimizing the bonding surfaces for the adhesive, adhesion can be increased without changing the adhesive itself. [Doo18, Hab16]

Due to the short range of molecular forces required for adhesion, it is necessary to clean the bonding surfaces of oil or dust before the glueing process [Hab16]. Even as little contamination as a finger print due to improper handling after cleaning can meaningfully impact strength of the bond joint [CBN+21]. The proper handling is an especially important factor for parts under dynamic loads. Frömmel investigated this using samples glued by different operators. The strength of the bond varied by 20 % and variance in test results was between 3 % to 28 % for different operators. This results in an order of magnitude difference in the observed parts lifespan between operators. [SF13]

2.1.4 Fracture Patterns of Adhesives

An adhesive bond can fail in various combinations of adhesion and cohesion failure, leading to various fracture patterns (shown in Figure 2-2) as described in DIN EN ISO 10365 [DIN95]. Multiple different failure modes can occur in the same part were different loading occurred.

First a differentiation is made according to the failing part, either the Adhesive or the Adherend. The adherend can either break further away from the bonding surface called a substrate failure or directly underneath the bond which would be a cohesive substrate failure. For composite materials a delamination is also possible where different layers of the material separate from each other.

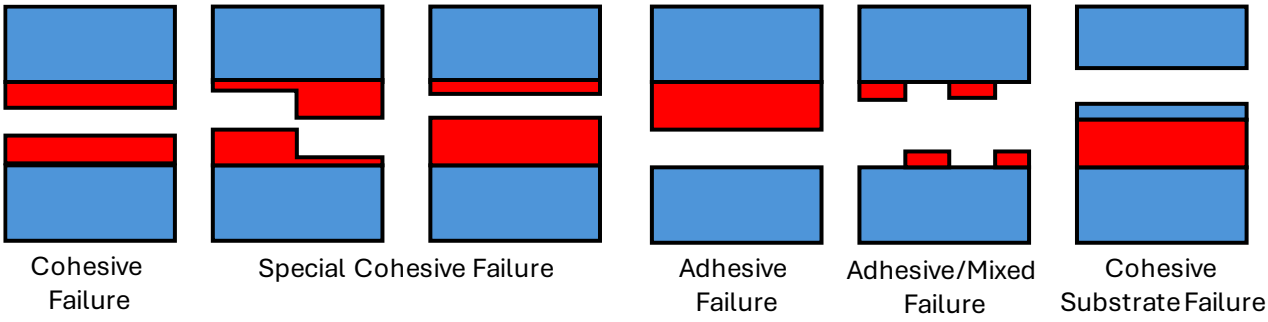

Figure 2-2 – Various failure patterns after [DIN95]

The adhesive can fail either thru cohesive failure or adhesion failure or a mix of both. There are three types of cohesive failure. A crack can form in the adhesive and travel through the middle of the adhesive layer parallel to the bonding surface (cohesive failure) and zig-zag through the bond layer without touching the adherend or near the bonding surface (special cohesive failure). Lastly crazing can occur where there is an uneven strain with areas of very high local deformation. In these zones the material whitens. This failure mode is most often observed in highly elastic materials.

The adhesion failures occur in the bonding surfaces between adhesive and adherend. These failures can either be on only one adherend or jump between the two adherends. Lastly a mix of both adhesive and cohesive failure can appear were the adhesive peels from the adherend and splits in the middle simultaneously.

2.2 Damage Detection Methods

The need for quality assurance during production and inspection during their life time of composites and adhesive joints have led to the development of various non-destructive testing methods. These will be briefly described below.

For adhesives the most common defect to occur is surface contamination either through improper cleaning, idle time between surface preparation and bonding or inappropriate handling. These can lead to an adhesion failure as these contaminants are weak points in the structure and often lead to crack formation. This crack will change the resonant frequencies of the part and lead to friction during cyclic loading which can be used to detect this damage. The following non-destructive testing methods have been developed to identify these signs according to [Ras12]:

- Ultrasonic testing
- Acoustic testing
- Radiographic testing

- Infrared thermal imaging technology
- Shearography
- And Vibration testing

In composites a major failure type is delamination, this shows changes in behaviour as described above when a delamination occurs, so the same methods can also be used. Carbon fibers are electrically conductive allowing for additional damage detection methods to be utilized. The following damage detection methods are being used for CFRP composites:

- Strain measurement
- Resistance detection technology
- X-ray detection technology
- Three-dimensional scanning laser vibration measurement technology
- Eddy current testing technology [DCC+21, DZJ+20]

Additionally, some damage detection methods have been developed specifically for aircraft composite wings:

- Electromechanical Impedance
- Laser shocks
- Nonlinear Ultrasonic Technique [CBN+21]

Most of the described testing methods need large equipment, shielding or onsite personal for the structural assessment. Thus, of the described methods only, a few are used for structural health monitoring such as the strain measurement.

Of the listed measurement techniques, the one most applicable method to this study is the resistance change method which was proposed for carbon fiber composite structures.

The measurement of changes in resistance for damage detection has been studied since the 1990’s. It doesn’t have an agreed upon name in the literature and can be found under the following names: electrical resistance change method, resistance detection technology, electrical resistance measurement or electrical monitoring. In this detection method the changes in the resistance due to the stretching cracking or delamination of the material is measured between various contact points. The analysis of the measured resistance over the load duration can then offer information on the severity and location of the damage. [SL99, TTS05] This method has been studied primarily in the development of CFRP for the aerospace industry.

The carbon fiber in the CFRP create a network of conductive fibers. Where these fibers are close together electrons can tunnel between with a higher chance leading to higher conductance. The strain of the material can then be measured as the distance between the fibers increases under strain decreasing the conductivity. Similarly, when a crack starts to form in the matrix the distance between the carbon fibers increases leading to a higher tunnelling resistance and lower conductance. The same effects occur in adhesives with conductive additives during loading. Figure 2-3 shows the influence loading has on the mean distance between fibers. [BAG+20, Kup01]

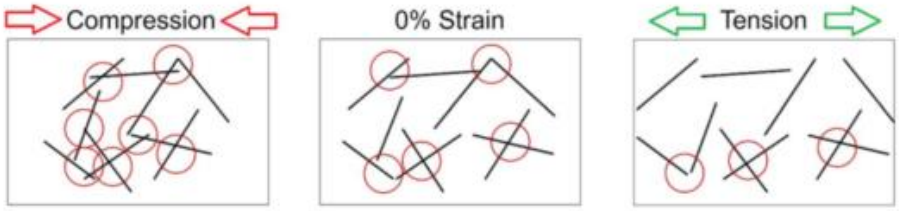

Figure 2-3 – Percolation behaviour during tension from [BAG+20]

For the additives to be conductive the fibers need to form a lattice-like structure where over long distances there are no spaces bigger than the tunnelling gap. This characteristic and the underlying mechanism is described by the percolation theory. At first as the conductive additive is added isolated clusters of connected particles grow, the conductance increases slowly. Eventually the clusters start to combine which can be observed by the conductivity increasing rapidly by orders of magnitudes. Once the percolation threshold is reached the clusters of isolated networks have almost all combined. The addition of more conductive material will only lead to a slow linear increase in conductivity, as the new particles will only provide shorter paths between points in the network instead of connecting previously unconnected clusters [MB13]. The effects of percolation theory are more often observed when an adhesive is hardening. Early in the hardening process the network of reacted molecules is sparsely dispersed, until suddenly the hardening process progresses rapidly when the percolation threshold for the molecule network is approached. [Kup01, SS94]

2.3 Dynamic Properties

Dynamically loaded adhesive joints are subject to a continuous reduction in strength due to fatigue and creep. True fatigue strength, where no more reduction in load bearing capacity occurs as cycles increase as can be seen in metals, does not develop for adhesives due to creep meaning the service life is entirely dependent on type of load, frequency and adhesive properties [Ras12]. “However, adhesives are generally regarded as possessing good dynamic

fatigue properties compared to other methods of fastening such as rivets, spot welds and mechanical fasteners" [Kin87], this is due to their even stress distribution in the joint [Kin87]. Pulsating and low frequencies promote creep and lead to premature fracture at lower cycle numbers however the overall service live is longer. The effective loading duration which takes into account the frequency and test duration is the same for all [Ras12]. Dynamic tests are described in the DIN 50100. In the pearl string method experiments are performed at various different loads for each sample and the results are plotted logarithmically in a S-N curve diagram, from which the dynamic properties can be obtained. [Hab09]

2.4 Stress concentrations and Fatigue

Stress concentrations are localized regions within a material where stresses significantly exceed the nominal applied stress. These arise due to geometric discontinuities, material heterogeneities or microstructural features. In ideal elastic materials, the effect of stress concentrations can be predicted using finite element method or analytically for simple geometries. The stress concentration factor is highly dependent on the radius of the part, with this factor reaching infinite for when it approaches zero. In such cases the theory of fracture mechanics is more applicable. In real materials, plastic deformation, microstructural constraints and damage mechanisms limit stress singularities. These stress concentrations are the predominant place for crack initiation. [Kin87, Sch09] These cracks or notches continue growing until the part fails or a section of the material work hardens thus stopping the growth. [Sch09]

Inclusions are particles embedded within a matrix (in the classic sense these are non-metallic particles in a metallic matrix) which are typically introduced in processing. These inclusions haver different stiffness, strength and bonding with the matrix leading to heterogeneous stress distributions under load. These particles act as stress risers due to the different properties specifically young's modulus and geometric discontinuity. Should debonding occur the inclusions effectively act like a void significantly increasing local stresses. [Sak09]

At stress concentrations, the local stress can exceed the yield strength even though the applied global load is still in the elastic region. This leads to localised plastic deformation, and to further increases in local stresses and crack nucleation. [Sur04]

2.5 Wind turbine blades

Wind turbines are devices that facilitate the conversion of kinetic energy from airflow into mechanical energy. The aerodynamic lift of rotor blades is utilised to generate electricity by turning a generator. Wind turbines can be divided into two categories based on the axis of rotation of the rotor: vertical and horizontal. These components are sometimes equipped with

shrouds or diffusers to concentrate the power on the rotor circle area, though this is rarely done in commercial applications.

It is hypothesised that wind turbines with a vertical axis of rotation were already in operation in Egypt 3,000 years ago. The configuration of these devices enables the usage of power near the ground without the need for gears, thereby significantly streamlining their construction for utilisation in early mills. These wind turbines are independent of wind direction. Conversely, these wind turbines possess a low-speed ratio and lack rotor blade adjustability. This type of wind turbine has not become widely used today due to its disadvantages. [Hau16]

The most common type of wind turbine in modern day is that with a horizontal axis of rotation. The advantages of this type of wind turbine include the ability to adjust the rotor blades to regulate power output and protect the system during extreme wind speeds, as well as the inherent efficient of this design. [Hau16]

The rotor blades must withstand many loads that can have different origins. Forces from the wind turbine itself come from its own weight, rotation (centrifugal force) and gyroscopic effects during rotation of the nacelle. In addition, there are forces from aerodynamics that can vary greatly due to turbulence, gusts, boundary layer to the ground, tower wake vortex and unsteady air forces such as flutter and vibrations. [Hau16]

Two different designs are used in modern rotor blades construction to carry these loads. In the box spar design, the longitudinal spar runs along the entire length of the blade and absorbs the majority of the loads. The shell plays only a minor role in the load-bearing function. In the single spar design, the shell contributes significantly to the stiffness. The single spar mainly absorbs the transverse forces and ensures stability. This construction method is usually lighter though more difficult to manufacture. [Hau16]

In either design the Shell is constructed from fiber glass composite with carbon fiber reinforcements in the critical sections i.e. the root and sometimes the spar. The shell is constructed in two halves the upper and lower shell. These pieces are then glued together. An example a wind turbine blade cross-section is shown in Figure 2-4 with the adhesive joints indicated. [Hau16]

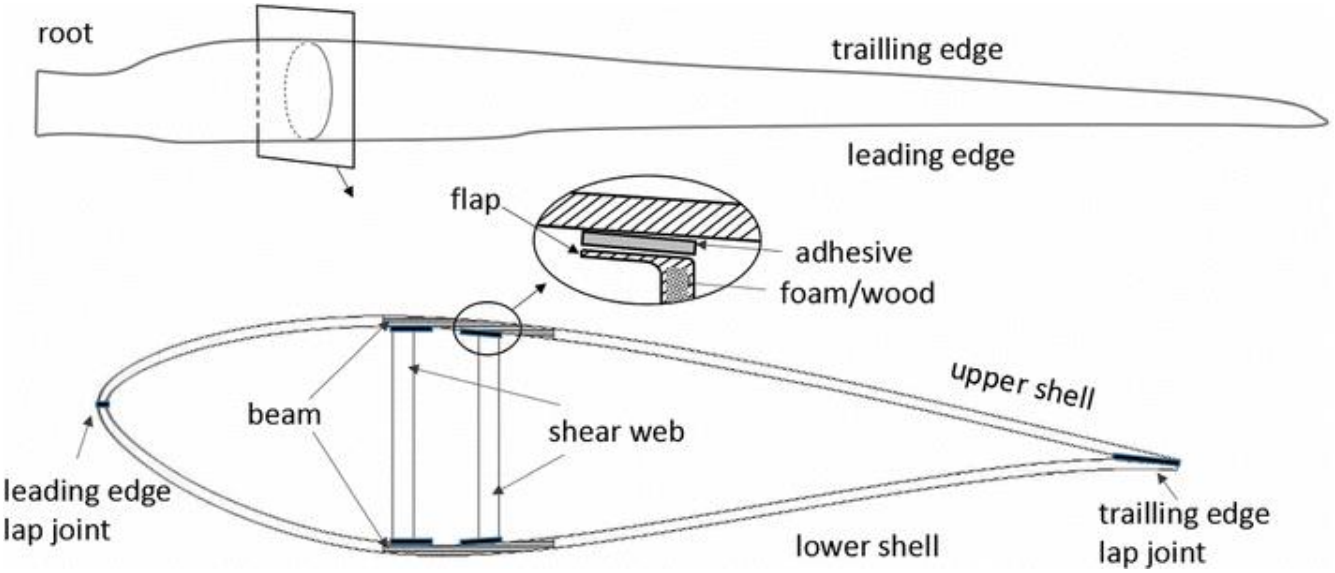

Figure 2-4 – Wind turbine blade design cross section from [LST+18]

During a wind turbines 15–30-year life it is exposed to high dynamic loads which can cause cracks to grow, lightning strikes and collisions with particles in the air leading to corrosion and abrasion of the leading edge. The mechanical damage and the locations in various parts of the wind turbine blade in which they can occur structure is shown in Figure 2-5. As such the monitoring and inspection of the turbine blades is an essential part of the operation of a Wind turbine. [SJD+04]

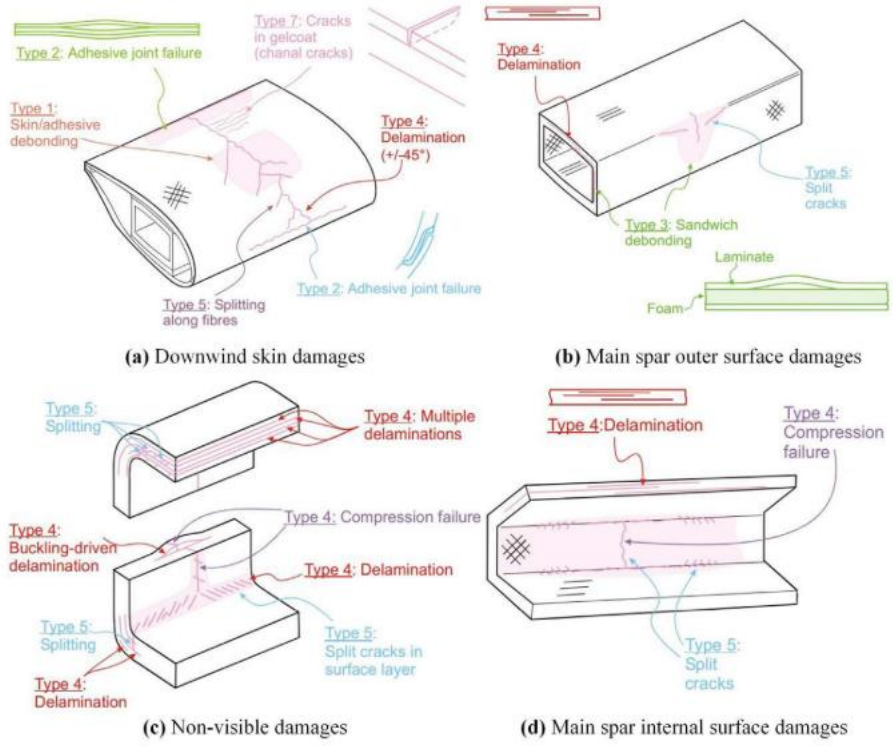

Figure 2-5 – Damage in a wind turbine blade from [SJD+04]

Many inspection methods for wind turbines require personnel to climb the wind turbine which is expensive, dangerous and limited to a small time frame each year when the wind is weak. Thus, there is a need for monitoring of the structure from afar through structural health monitoring. In most wind turbines this is already implemented in the monitoring of the shaft and generator. For the turbine blades experiments have been carried out to monitor blade structure using various damage detecting techniques to find damage during operation. The following damage detection methods are currently being researched: strain measurement, acoustic emission, ultrasound, vibration, thermography and Machine Vision. [DZJ+20]

“The inspection of wind turbine blades is a rather complicated task, as they exhibit an arbitrary curved surface, constitute complex multi-layered structures, are made with anisotropic materials and have variable thicknesses. (…) The most commonly applied NDT (Non-destructive testing methods) are: visual testing, ultrasonic testing, thermography, radiographic testing, and acoustic emission.” [KPN21] More damage detection methods are currently being researched especially the topic of machine vision. [DZJ+20]

3 State of the Art

The following section provides a brief overview of the current state of the art of In-situ damage detection of adhesives and laminates. There has been much research performed on carbon nano tubes (CNT) modified laminates as well as adhesives for the purpose of structural health monitoring (SHM) testing however these often use conductive adherends or non-integrated electrical contacts.

3.1 Structural Health Monitoring

The topic of SHM of adhesives using electrical resistance measurements is new and unexplored. The few research papers found on this topic which are relevant to this paper are summarised. A significantly larger body of research exists for the SHM of carbon fiber reinforced polymers (CFRP) panels using electrical resistance measurements, thus some of this research is included here.

A research group at the Tokyo Institute of Technology researched the delamination detection in CFRP. Akira Todoroki et al. proposed the measuring of electrical resistance in the laminates for damage detection. A CFRP plate was produced with a copper foil placed in a pattern above the outer layer during lamination to act as measurement contact electrodes. Using indentation tests the CFRP was damaged until delamination, which could be detected using this method. [TTS01] This was further investigated in a follow-up paper using finite-element-method analysis. A delamination was simulated in a CFRP with electrically conductive matrix and different contacts at different positions to this delamination. Using this a neural network was trained to determine the position of the delamination based on the electrical resistances measured. With decreasing fiber volume fraction the spacing between contacts could be increased with similar estimation error of the delamination location. [TTS05] For the usage in rotating components such as helicopter or wind turbine blades a method using oscillating frequency changes was investigated, which has the benefit of potentially being a wireless SHM system. The laminate is used as a resistor for the oscillator. Due to the presence of delamination in the CFRP the oscillating response of the samples is shifted to higher frequencies. However this method has a lower sensitivity than the resistance change method. [MT06] Later different measuring techniques where investigated. The measurement through inductance, impedance and capacitance showed promising results being able to detect the damage. In this method a driver and pickup coil are placed above and below the samples. This method was shown to be effective in determining through thickness electrical properties of the CFRP. [MIM+24] All of these methods have a strong dependence on temperature meaning temperature compensation must be used.

The above-described processes focus on the sensing capabilities of laminates, similar sensing capabilities can also be achieved in adhesives through modification using CNTs.

Oliva-Avilés et al. showed that applying electrical fields during the curing process could improve the sensitivity of CNT modified adhesives by aligning the CNT during curing. Aluminium electrodes were placed on the surface on which the adhesive was cured and an electrical current is applied. 0.1, 0.3, 0.5 and 0.75 weight percent (wt%) of CNT were tested using downscaled Dog Bone samples. The percolation threshold was the same for aligned and non-aligned CNTs. However, the conductivity was 3 to 5 orders of magnitude higher with the alignment of the CNTs at 0.1 to 0.5 wt%. The produced films with aligned CNTs had a higher piezoresistive sensitivity. The films could reproducibly measuring the applied strain during loading cycles as well as the permanent deformation. [OAS11]

Lucio Pinello et al. investigated the usage of CNT modified CFRP for in-situ monitoring of impact dynamics in 2025. The CFRP panels with six different contact patches were tested according to the ASTM D7137 standard in a drop tower setup. During this the electrical resistance was measured between the three sets of contacts. For the control measurement a thermal camera was used to measure heating of the sample due to the impact and a fiber bragg grating sensor to measure stress and strain direction. From the electrical resistance measurements matrix cracking, delamination and permanent damage after unloading could be identified. The closer set of contacts had a higher sensitivity to the damage. It is notable the resistance decreased during these tests as the samples were under compression decreasing the tunnelling distance between CNT-fibers. From the slope of the resistance change it can be predicted if buckling occurred in the samples. The authors recommend to use a machine learning algorithm to analyse the signal as the analysis is nowadays based on experience-based modelling. Furthermore they propose the usage of bucky paper inside the panels to deal with the statistical distribution of resistance values from the dispersion process of CNTs and improve results. [PFV+25]

3.2 Electrical Contacts/Embedded meshes

Previous research on adhesive SHM through resistance measurements as described in the papers above was done using contacts ranging from silver paste, conductive substrates and solder. This cannot be used in the deployment of SHM systems for wind turbines due to the manual work associated with these contacts, their fragility and the properties of the glass fiber reinforced polymer (GFRP). Therefore, a new method using metal meshes as contacts will be explored in this paper. In this section shows the state of the art on the usage of metal meshes

inside various polymers, adhesives and composite structures. The wire dimensions used in these papers are gathered in Table 3.1 at the end of this chapter.

Marzena Pawlik et al. investigated the effects on adhesion strength between two CFRP laminates when different surface treatments were used. The investigated surface treatments are acetone cleaning, sanding, grit blasting, peel ply and a metal mesh. The stainless-steel mesh with an aperture of 178 µm and a wire diameter of 140 µm was placed above the CFRP prepreg and infused during the curing process of the laminate. Samples cleaned with acetone had a lap shear strength (LSS) of 12.0 ± 2.0 MPa. “Grit blasting, sanding and peel ply enhanced the lap shear strength up to 13.7 ± 1.4 MPa, 14.5 ± 1.5 MPa, 14.8 ± 1.8 MPa, respectively” [PYG+22]. Using the metal mesh a LSS of 24.2 ± 6.4 MPa was measured which is an increase of 101.7 % compared to samples only cleaned with acetone. Though the metal mesh had a statistically significant variability in test results. The common failure mode of the metal mesh samples was the interface between metal mesh and CFRP, thus it was concluded that the metal mesh acts as a adhesion promoter. [PYG+22]

R.K. Naik et al. produced metal sheet thermoplastic sandwiches reinforced with a metal mesh spotwelded to the metal sheet. Usage of the metal mesh was theorised to improve adhesion. These sandwiches were then tested in double lap shear tests, peel tests, V-bending tests and uniaxial tensile tests and compared with simulation results. Only the area density of 1.12 kg/m^2 was mentioned for the mesh parameters. No mention of a failure of the metal mesh or the adhesion between metal mesh and polymer is made. The bonding between thermoplastic and metal sheet was most often the first point of failure, leading to buckling in the V-bending tests. [NPR22]

Metal meshes can be used as heating elements to melt a thermoplastic in a bond line in a process called resistance welding. Two parts are pressed together with a small thermoplastic foil and wire mesh between them. As the wire heats up the thermoplastic melts and bonds the two parts together. Martine Dubé et al. investigated the effect of different wire diameters and open gap widths using four stainless steel meshes on single lap shear strength (LSS). Tests were performed using GF and CF adherend laminated with thermoplastics of either PEI or PEEK. The authors calculated a ratio between open area and wire diameter. This ratio was found to be the most important factor in the resulting LSS. The wire mesh with the highest ratio showed an interlaminar failure of both the adherend and the mesh as well as the highest LSS. It was found using a scanning electron microscope that the polymers did not adhere well to the

mesh and it was recommended to investigate the improvement of adhesion through surface treatment of the metal mesh which is discussed in another paper further down. [DHG+12]

In 2024 Dongyang Cao et al. used as similar method as described in the paper above to resistance weld PLA 3D printed parts using three different metal meshes. Ni-Co and two Ni-Cu meshes were used in this paper. Optimal process parameter to ensure good impregnation of the metal mesh with the polymer were found using various heating times, compression rates/pressures, and voltage settings. The produced samples were tested in three point bending tests and compared to solid samples without metal meshes to gauge the bonding effectiveness. Even though the main investigation of this paper is to find optimal process parameters for the resistance welding, optimal parameters were found using multivariable linear regression analysis for each of the three metal meshes allowing a view into the adhesion properties of the various meshes. The Ni-Cu mesh with 34 % open area and 0.07 mm wire diameter performed best with a 94 % welding strength efficiency (welding joint had 94 % strength of the base polymer material). The other Ni-Cu mesh with 30 % open area and 0.11 mm wire diameter had a welding strength efficiency of 82 % and the Co-Ni mesh with 36 % open area and 0.25 mm wire diameter had a welding strength efficiency of 87 %. In addition, the welding strength efficiencies of this paper were compared to other bonding tests from other research papers. According to the authors the resistance welding process “demonstrates commendable efficiency in achieving welding strength”. [CBL+24]

In the previously discussed papers, the metal meshes were cleaned before use. However, a huge part of bonding strength is the adhesion between the adherent and the adhesive or polymer. This can be optimized through surface treatments as discussed in section 2.1.3. Vincent Robert et al. investigated the effects of various coating on the adhesion between stainless steel (SS) heating elements and PPS polymer. The stainless-steel heating element was coated with a silane coating in a five-step process. This coating is often used to improve adhesion between organic and inorganic materials. Water contact angle tests showed a significant surface activation with angles for untreated SS being 78° and the silane coated SS being 11°. The coating was tested in SLS and double cantilever beam (DCB) tests. The uncoated DCB samples could not be tested due to failure in their production and no statement on the critical energy release rate could be made with regards to coating optimization as there were too high standard deviations. Tests on coated DCB samples revealed mixed failure behaviour, including fibre cracks and interfacial failure between the matrix and the fibres, which was clearly visible on their surfaces. In the SLS tests the best process parameters resulted in a 32 % higher LSS than uncoated stainless steel meshes. The coated SLS failure was between

the matrix and the fibers showing that good adhesion between matrix and mesh was achieved. [RLD20]

As can be seen from these different papers the usage of metal meshes can significantly improve the overall bond strength and in certain examples it can act as an adhesion promoter, though it does introduce a significant variability into the bond strength. In Table 3.1 the wire cloths used in the described papers are listed. Various different meshes have been used with different apertures, wire diameters, and materials. These have not been all investigated in comparable experiments, thus the effect that these three parameters alone have on the bond cannot be concluded.

Table 3.1 – Metal meshes used in various research papers

Paper (Mesh)	Material	Wire Diameter (mm)	Open Gap Width (mm)	Open Area (-)
CBL+24	Ni-Co	0.25	0.381	0.36
CBL+24	Ni-Cu	0.05	0.07	0.34
CBL+24	Ni-Cu	0.11	0.14	0.3
DHG+12 (A)	SS	0.114	0.152	0.327
DHG+12 (B)	SS	0.066	0.104	0.374
DHG+12 (C)	SS	0.041	0.089	0.469
DHG+12 (D)	SS	0.036	0.043	0.296
NPR22	Steel			
PYG+22	SS 316	0.14		
RLD20	SS 304	0.04	0.09	0.479*

* Calculated from wire diameter and open gap width

4 Problem statement and research objective

In the wind energy and aerospace sector the main load bearing structure composed of stringer spars and ribs are connected through with either rivets or adhesives. These parts are required to withstand high loads for their entire service lives with minimal inspections, additionally, due to cost saving measures there is an incentive to extend maintenance intervals by utilizing increased remote monitoring. Currently structural health monitoring (SHM) systems for the entire blade are only capable of pinpointing the location of or presence of damage. However, these systems are not yet able to identify the cause of the issue in the structure.

As a critical structural component between stringer and shells, it is important to develop a SHM system for the adhesive bond. An attractive option is the use of resistance measurements between embedded electrical contacts in the adhesive to track the development of the cracks in the bond. Early development of these systems focused on the development of an adhesive with an electrical conductance of 0.1S/m, a value just above the percolation threshold has already occurred at the Deutsches Zentrum für Luft- und Raumfahrt e. V. (DLR). Additionally, this adhesive has been characterised in various tests. The effect of an embedded electrical contact on the mechanical strength of the adhesive layer has, thus far, not been researched.

One example of such an electrical contact system is found in metal meshes developed in the aerospace sector in the form of lightning strike protection systems, which were found to be well suited to the task of electrically conducting in laminate structures. However, these conducting systems have not been tested for their mechanical properties. Thus, it is the aim of this paper to investigate the effect various mesh geometries have on the mechanical properties of the bond strength. In particular the important parameters identified are wire diameter and open area. A few wires material will also be studied as the material needs to both be conductive enough for the SHM system and withstand the dynamic loads.

Furthermore, the various failure modes (adhesion, cohesion and mixed failure) could display different resistance changes which would make it possible to determine the failure mode through these systems. That is why another objective of this paper is to determine which types of damage can be detected using this type of SHM system. Due to the size of wind turbines, it is important to be able to localize the damage to a given area, although this has been tested in laminates it has not yet been tested in adhesive layers yet. Accordingly, the ability to localize various failure modes will also be assessed.

4.1 Hypothesis

At the start of this work, several hypotheses were formulated regarding the influence of mesh reinforcement on the overall adhesive layer strength and the detectability of different failure modes using resistance measurements.

With respect to material properties, two competing effects might be expected. Materials with a similar young's modulus to the adhesive can reduce stress concentrations around the wires and thereby improve fatigue life. In contrast, meshes with a high young's modulus are expected to stiffen the bond, allowing the mesh to carry a larger share of the load and thus increase the overall strength of the adhesive layer. This could act similarly to the γ' and γ phases in nickel superalloys, where the γ' phase has a high ductility and doesn't fracture while the γ phase has a high strength. [SSH87] The interaction between the two phases strengthens the material.

The mechanical properties are influenced by the mesh geometry of wire diameter and open area. Larger wire diameters could reduce local stress concentrations, limiting crack initiation and increasing fatigue life. For the open area, two opposing effects are anticipated. A higher open area reduces the number of wires; if the wires act primarily as crack stoppers, this will reduce strength. If stress concentrations at the wires dominate, a higher open area will reduce these effects and increase strength.

For the demonstrator, hypotheses are formulated regarding the detectability of different failure modes. Adhesive failure is expected to be the most sensitive to detection, as it occurs at the interface between laminate and adhesive and directly interrupts the conductive paths. However, detection depends on the measurement path thus detection may not be possible if the failure is not located between the selected contacts or on the opposite side of the adhesive layer relative to the contact. Cohesive failure is expected to be less sensitive, as electricity finds paths to bypass small cracks. In both cases, the change in resistance may be small if the damaged cross-section is limited.

Mixed failure is expected to show a stronger effect, should it separate regions of the adhesive and isolate electrical contacts, leading to a significant increase in resistance. This effect is expected to be more pronounced between contacts located in different regions of the bond. However, incomplete through-thickness separation may limit detectability for contacts positioned on opposite sides of the adhesive layer.

5 Materials and Methods

In this section, the materials, machinery, and tools employed in the study are introduced and described. The methods used to produce the test specimen and the demonstrator are outlined, followed by the experimental procedures. Finally, the rationale underlying the selection of the various experiments is discussed.

5.1 Adhesives and Additives

There are four adhesives relevant to this thesis. The properties of these adhesives are shown in the Table 5.1.

Table 5.1 – Properties of the adhesives used in this study

Adhesive (abbreviation for use in Samples)	RIMR 035c 1% MWCNT, 3% Aerosil, 10% GF (RefB)	RIMR 035c 1% MWCNT, 3% Aerosil, 10% CF	EPIKOTE™ Resin MGS RIMR 035c (RefC)	EPIKOTE™ Resin MGS BPR-137GF (RefA)
Pot time (min)	-	-	190-240	120
Curing Temperature (°C)	-	-	80	75
Curing Time (h)			5	4
Youngs Modulus (MPa)	4356*	5498	3100	5500
Tensile Strength (MPa)	59.2*	73.5	70	75
Ultimate strain (%)	3.47*	1.84	7-10	2.9
T_g	-	-	80	81

*Tested without MWCNT's

The two modified Adhesive systems investigated in this thesis are the result of two previous theses [Mar25, Zel23] at the Institute of System Light weight design at the DLR Braunschweig. A low viscosity infusion epoxy resin from Hexion is used as a base composed of the resin "EPIKOTE™ Resin MGS RIMR 035c" and the hardener "EPIKURE™ Curing Agent MGS RIMH 037". The mixing ratio by weight for this adhesive is 100:28. This adhesive is commonly used for bonding glass carbon or aramid fibers which experience high static and dynamic loads.

In both adhesives were modified with 1 % by weight (wt%) multi walled carbon nano tubes (MWCNT) procured from IoLiTec. The MWCNT provide the required electrical conductivity and 1 wt% has been found to be just above the percolation threshold from previous studies. The

MWCNT have a high specific surface area between 250-300 m^2/g and therefore need to be dispersed in the adhesive using a three-roll-mill.

To increase the viscosity and achieve the required thixotropic properties of the adhesive 3 wt% of Fumed Silica produced by Evonik under the name Aerosil are added.

The mechanical properties are achieved by adding 10 wt% of either carbon short fibers or glass short fibers. This increases the young's modulus to the required amount although it has the downside of reducing the fracture strain.

The carbon short fiber is recycled carbon fiber sold under the name "carboNXT milled PURE" made by Mitsubishi Chemical Advanced Materials GmbH. The carbon short fibers have a density 1.8 g/cm^3 and a bulk density of 150 g/l. The tensile modulus is above 3200 MPa.

The glass fibers used is FG 400/030 from STW Kautzmann GmbH. These have a higher specific weight than the carbon fibers at 2.53 – 2.55 g/cm^3 and a lower tensile modulus of 1800 - 3100 MPa. The glass fibers provide lower mechanical properties than the carbon fibers. The glass fibers will be used in this thesis as the investigation of the contact options in the form of wire mesh should not be influenced significantly by the small difference in mechanical properties. In addition, using both adhesives would not aid in the comparison of the different wire meshes.

Two adhesives were used as references for the modified adhesives. The first reference adhesive is a commercially available two-component glass fiber reinforced epoxy resin wind turbine certified adhesive. It is composed of the resin "EPIKOTE™ Resin MGS™ BPR 135G3" and hardener "EPIKURE™ Curing Agent MGS™ BPH 137G/137GF" made by Hexion. The mixing ratio by weight for this adhesive is 100:45. The mechanical properties of this adhesive were used as targets during the development in the modified adhesive system. Additionally, the unmodified "EPIKOTE™ Resin MGS RIMR 035c" and "EPIKURE™ Curing Agent MGS RIMH 037" system is used to make sure that no negative effects on the mechanical properties have been introduced due to the addition of the additives.

5.2 Metal Meshes

To achieve the contact between measurement devices and the adhesive layer which is to be monitored various different materials come into question. The materials considered in the early phases of this study are non-woven fabrics (fleece), wire cloths (metal meshes), perforated sheets and expanded metal sheets. These materials are all semi flexible with open area for adhesive to flow through and thus could be used for the contacts. To limit the scope of this study only the wire cloths were investigated. It is hypothesized that the observed relationship,

regarding mesh geometries, may be broadly representative and thus extendable to the other material systems.

A few benefits of the metal mesh are the availability of the materials and the range of mesh parameters which can be procured. A benefit of the metal mesh is the flexibility of the material to follow the contour when laid onto a curved shape.

There are multiple different ways to weave wires into a metal mesh. The simplest is the plain weave where the wires alternate between going over or under the perpendicular wires. A diagram of a plain weave fabric with mesh parameters is shown in Figure 5-1. All of the meshes used in this study are plain weave as this is the most common used weave for metal meshes, and is the only commonly available weave type for fine metal cloths.

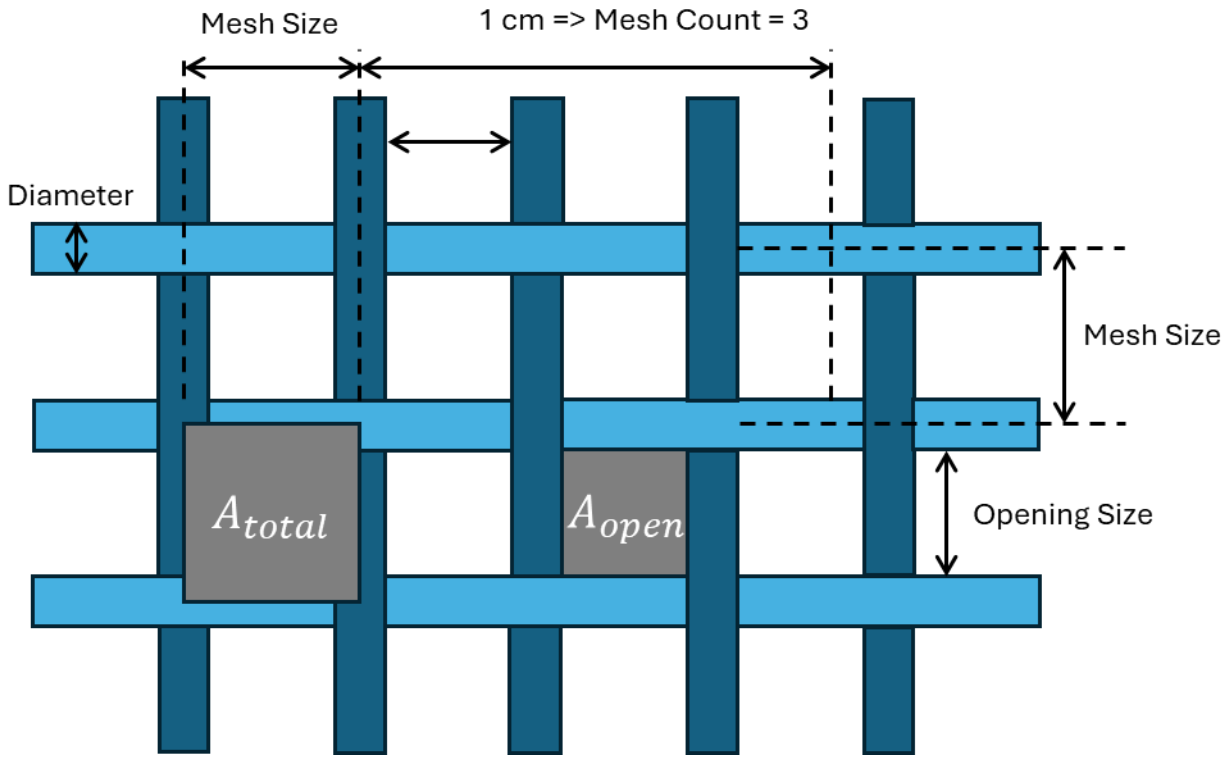

Figure 5-1 – Schematic of plain weave fabric with parameters

The parameters which can be chosen in addition to the weave type are the wire diameter and the opening size. The opening size, also known as the mesh width, is the distance between the wires. The opening size can be different in the x and y directions, though this is rare for plain weave wire cloths. From these two properties the other characteristics such as the mesh count, mesh size and open area can be calculated.

The mesh size is the number of wires per a given distance, often in wires per inch or wires per cm and is how wire cloths are most commonly described. The open area of a mesh can be calculated using the following formula, where d is the wire diameter and mw is the mesh width:

$$Open\ Area = \frac{A_{open}}{A_{total}} = \frac{(mw)^2}{(mw+d)^2} \quad (1)$$

As the wire material has different material properties than the adhesive, it could act as a stress riser in the adhesive layer. As the notch sensitivity is very dependent on the radius [CG13] different wire diameters will be investigated as well as different materials with different young's modulus. In addition, having less disruptions in the adhesive layer could improve its performance thus the effect of open area will also be investigated. Nine metal meshes were chosen to test these parameters with. The properties of the wire mesh can be found in Table 5.2, were the meshes with the same wire diameter and open area are highlighted red.

Table 5.2 – Properties of wire meshes used

Abbreviation	Material	Wire Diameter (mm)	Opening Size (mm)	Open Area (%)	Mesh Size (Wire / Inch)
S1	Steel 304	0.14	0.46	59	42x42
S2	Steel 304	0.14	0.18	31	80x80
S3	Steel 304	0.14	0.15	25	90x90
S4	Steel 304	0.09	0.12	31	120x120
S5	Steel 304	0.19	0.23	31	60x60
S6	Steel 304	0.25	0.38	36	40x40
NiCr	Nickel-Chromium	0.25	0.38	36	40x40
Cu	Copper	0.25	0.38	36	40x40
Al	Aluminium	0.25	0.38	36	40x40

The wire meshes made from steel were used to investigate the wire diameter and open area as these could not be found in copper in adequate sizes. Copper would have been preferred as it has a higher conductivity which is thought to have a better measuring sensitivity to the crack formation. The five meshes used to investigate the mesh properties are S1-S5. Three metal meshes have the same wire diameter and three have the same open area. Allowing for independent study of these two geometries.

The other four meshes have the same mesh parameters and are made from different materials. Copper has the highest conductivity and is used widely in the electrical industry for wire

production. Although it is known to not develop as many dislocation barriers which means it has a lower fatigue ratio. [MS20] Copper would be the ideal material for this application due to the high conductivity, however should it not be usable under dynamic loads the other three potential materials might make adequate replacements.

Scanning electron microscope (SEM) pictures of these four wire cloths were taken at the TU Braunschweig to analyse the surface structure, these can be seen in Figure 5-2.

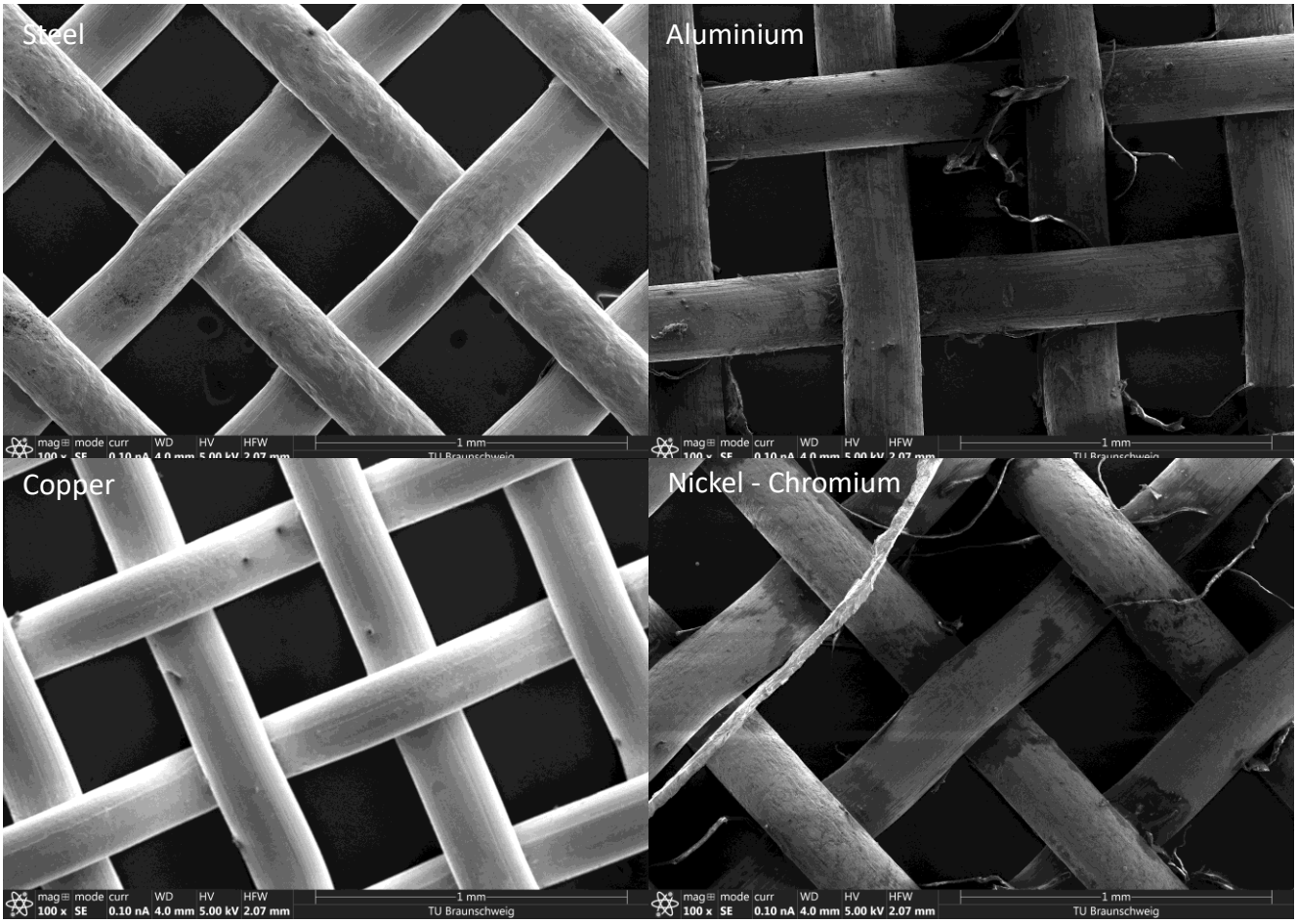

Figure 5-2 – REM scans of different wire mesh materials

Before they were analysed the samples were cleaned thoroughly with isopropyl alcohol. The small strands of material seen especially on the NiCr and Al cloth are from the cleaning paper. Both the steel and copper samples have few deposits (black dots) on their surfaces. The aluminium and nickel-chromium metal mesh show significant contamination at the points where the wires intersect. The contamination is darker compared to the material; perhaps this is oil or residue from the weaving process. This contamination could not be removed though mechanical cleaning. Attempts at cleaning in an ultrasonic bath should be attempted in further studies should the adhesion between adhesive and mesh be a weak point, though the applicability of this in large scale production is questionable.

The distributor of these materials does not deliver material data sheets with these wire-meshes; The 304 stainless steel is the only material where the alloy is mentioned. Energy-dispersive X-ray spectroscopy (EDX) was used to determine the composition of each material. The results of the EDX analysis can be found in the appendix 9.2. This was then referenced to data tables to determine which alloys match these results from the EDX. The material properties and for the alloys are listed in Table 5.3. The elastic modulus is a key property of these materials as it can affect the load distribution within the adhesive layer either reducing or enhancing its strength.

The listed E-moduli might not represent the actual properties of the wire mesh as the wires have been processed and stretched to form the wire cloth. This can work harden some materials.

Table 5.3 - Properties of the mesh materials used in this study

	Alloy [Source]	Electrical Conductivity (MS/m)	E-modulus (GPa)	Density (kg/dm^3)
Steel	Stainless Steel 304 [Thya]	13.89	193	8.0
Nickel-Chromium	Inconel 601 [MET]	0.84	207	8.1
Copper	Pure Copper [Thyc]	58	127	8.94
Aluminium	AlMg3 [Thyb]	20 to 23	70.5	2.66

Another consideration with these materials is reactions with the adhesive. An aluminium material was used in a previous study with MWCNT at the DLR and was noted to show signs of galvanic corrosion. This was also investigated by Ireland et. al. between GFRP modified with MWCNT and Aluminium. In high humidity environments no significant increase in corrosion was observed but in aggressive environments the corrosion resistance was significantly lower. [IAL12] For steel bonded with CFRP modified with MWCNT Arronche et al. found no increase in corrosion compared to samples without MWCNT modification. Though if this difference occurred because CFRP was used instead of GFRP was not determined. [AGR+13]

A downside of wire meshes is that the electrical resistance is not homogenous. The shortest distance will be longer for diagonal distances due to the Manhattan geometry of the wire mesh, which need to be used instead of the usual Euclidian distance calculations. In addition, the resistance can be higher in the diagonal direction, as the perpendicular wires form point contacts when crossing each other. Thus, a resistance increases of at least 41 % is expected

compared to a solid material. Measurements on the wire mesh confirm this higher resistance in the diagonal direction. The resistance was measured between two points 20 cm apart on the wire cloth S6. In the weave direction the resistance is 0.81 Ω while at 45° to this the resistance is 1.44 Ω. This is an increase of around 77 %. For small contact patches in samples this difference will not be significant due to the high conductivity of the contact material. However, for very large applications this could pose a problem.

5.3 Adhesive Production

The production of the modified Adhesive can be split into five steps:

1. Dispersion of MWCNT into a resin masterbatch
2. Mixing hardener and remaining additives
3. Mixing the modified adhesive
4. Application of adhesive on adherend material for sample production
5. Curing of the adhesive

These steps will be further explained in the following sub-sections; though, the sample production is discussed in Section 5.4.

5.3.1 Dispersion of MWCNT using a three-roll mill (Resin Master Batch Production)

When particles with high surface area and an active surface are mixed, attractive forces form and these particles form agglomerates. These do not mix well through normal means and need to be dispersed under high shear forces so the particles spread evenly throughout the mixture.

A 3 kg masterbatch of resin was produced at the start of the thesis from which all the adhesive for the samples and demonstrators was made. The masterbatch was made from the resin “EPIKOT Resin MGS RIMR035C” and 2 wt% MWCNT. For the dispersion a three-roll mill (EXAKT 80 E PLUS Three Roll Mill, EXAKT Advanced Technologies GmbH, Norderstedt, Germany) was used. A picture of the setup can be seen in Figure 5-3.

Figure 5-3 – MWCNT dispersion setup using the three-roll mill

To start all tools and the machine used in the mixing are cleaned using acetone. The MWCNT was measured into the container cautiously to avoid agitating the additive. Due to its low bulk density it tends to cover everything in a small layer if agitated too much. Therefore, this initial mixing was done under a fume hood to avoid breathing in the MWCNT. Then the resin was poured into the container until the required amount was reached. Using a mixing utensil the resin was gently stirred by hand until all the MWCNT were covered in resin and no dry spots could be seen anymore. After this the MWCNT can no longer be suspended in the air and it is safe to take it out of the fume hood.

To break up the agglomerations of MWCNT in the resin the three-roll mill was used. The three-roll mill was set to a speed of 300 rpm for the final roller during the continues operation. For the start and stops between cycles lower speeds were used to be able to handle the material effectively and not let the machine run dry. During the entire mixing procedure, the mill is cooled to 20 °C using a “CF31 Kryo-Komakt-Thermostat” from Julabo.

The instructions from the previous work were followed to disperse the MWCNT in the resin using four different cycles performed with different gap sizes. However, the gap width of 150/50 µm resulted in a non-existent material throughput rate. The lower gap size of 45/15 µm

intended for the second cycle provided a high material throughput rate and thus the 150/50 µm gap size cycle was skipped.

For each pass-through, the material was poured and later scooped using a spatula into the input of the three-roll mill and collected in a tray in front of the machine. The collection tray from the previous pass-through and the machine were scraped clean with the extra material being fed into the machine. Following this the trays were switched and the pass-through was marked down in a table. Each cycle of a gap size is comprised of five pass-throughs of all the material. During the last cycle using the gap size mode the forces exerted by the rollers was recorded. In Table 5.4 the process parameters for the dispersion process are listed.

A final cycle in the force mode was done with only one pass-through. The force was slowly increased until the force measured was twice that of the recorded force during the previous cycle. During this pass-through extra caution was used to avoid running the three-roll mill without any material, because the shear forces could scratch or damage the rollers should they touch each other. Following this, the Masterbatch was packed air-tight in cleaned containers and stored in a freezer until further processing steps required it.

Table 5.4 – Process parameters and force-data for dispersion of MWCNT in resin for the masterbatch

Mode	Gap width roller 1/2 (µm)	Pass-throughs	Force roller 1/2 (N/mm)
Gap Distance	150/50	-	-
Gap Distance	45/15	5	3.1/1.5
Gap Distance	15/5	5	2.8/1.2
Force	0/0	1	6/3

5.3.2 Hardener Component

To effectively mix the resin and the hardener components in the Speed Mixer DAC 700.2 VAC-P, Hauschild (the mixing procedure and machine is described in Appendix 9.1) they have to have similar viscosities. Since the masterbatch of resin contains the MWCNTs and has a high viscosity, the remaining additives are added to the hardener. As the used additive mixture was the same throughout this thesis a large batch of material enough for 1 kg of adhesive was prepared for each series of experiments. This ensures that the material properties are not influenced by the mixing and measuring of the hardener component. The hardener batch contained 188.125 g of hardener, 30 g of Aerosil and 100 g of glass short fiber.

Before the mixing, the Aerosil and the glass short fibers where dried in the oven at 120 °C for one hour. The containers were covered in aluminium foil with a few holes to reduce the agitation of the fibers.

For the mixing of the Aerosil and the short fibers breaking up the agglomerates is not a vital component of the mixing process thus the dispersion using the three-roll mill is not required. For the short fibers it can even be harmful as the fibers can break shortening them and thus reducing the reinforcing effect they have on the adhesive. Therefore, the hardener components are mixed using the speed mixer and time as shown in Table 5.5.

To start, all the containers are cleaned with isopropyl alcohol. All of the measuring of the components is done under the fume hood. Half the required amount of Aerosil is measured into the speed mixer container, with care taken to minimize disturbance as the Aerosil has a very low packing density and thus is easily agitated. Only half of the Aerosil was used initial due to its low bulk density to not overfill the container. The hardener was then added, before mixing the container was closed with the lid and then sealed with tap to prevent the container from bursting. In the lid a small hole was punched to avoid pressure build up. The components were mixed using the speed mixer. After mixing the container walls are scraped down as some of the light Aerosil gets pushed up the sides of the container and does not mix. The remaining Aerosil is added, and this was mixed again. During the mixing of the Aerosil and the hardener, no vacuum was used to avoid pulling the additive into the air. After scraping the walls of the container again the glass fibers are added and the mixture is mixed with a vacuum of 3 mbar. The resulting batch of hardener is sealed and stored in a freezer.

Table 5.5 – Process parameters for the speed mixer

Parameter	Section 1	Section 2	Section 3	Section 4
RPM (1/min)	1200	1600	1800	2100
Time (seconds)	90	20	20	10

Throughout the production of the samples, changes in the properties of the hardener master batches were observed. As the batch was left in the freezer the viscosity and stickiness to the spoons seemed to change. This change was theorised to be possible due to either the evaporation of volatile compounds or absorption of water, since the hardener has a very strong smell indicating evaporation, while the additives (mainly Aerosil and glass short fiber) are known to absorb water. To verify if this observed change was due to actual material changes or simply

observation differences it was decided to investigate this using thermogravimetric analysis (TGA) and differential scanning calorimetry (DSC). For this analysis samples were taken from the batches at various times as if they were used up, while recording the day they were taken. Then they were tested in a TGADSC3+ from Mettler Toledo according to the following testing profile. First a 5-minute static temperature section at 30 °C is used so the temperature of the sample and the DSC measurement can settle down. Next the sample is heated at 1 °C/min up to 120 °C, with a final 15 min holding period at this temperature.

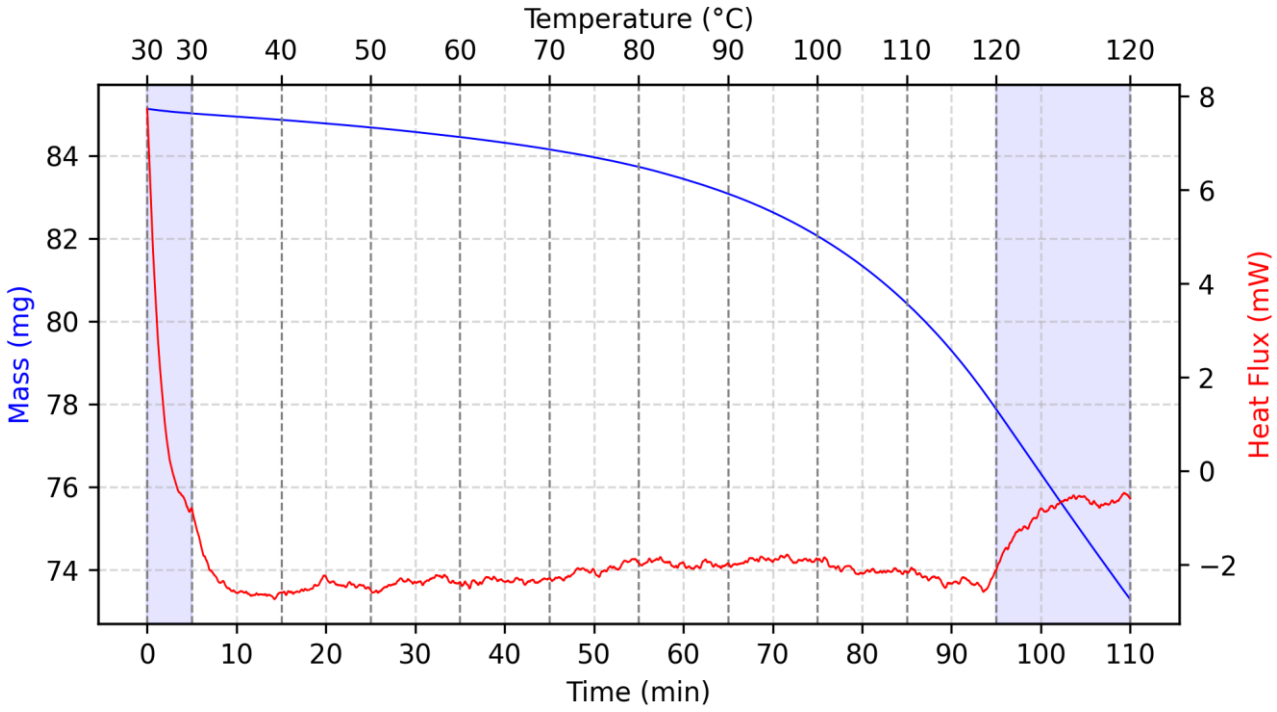

Figure 5-4 – Mass and heat flux of hardener batch during DSC & TGA analysis

The results for one experiment are shown as example in diagram Figure 5-4. It can be seen that as the temperature increases more material evaporates and that the heat capacity remains unchanged after an initial settlement period. This was the same for all samples. The change in mass for the various samples over three different temperature ranges are shown over time in the Figure 5-5. The temperature ranges of 30-50 °C, 50-80 °C, and 80 to 120 °C (including the 15 min holding periods, plotted on left vertical axis) were chosen to evaluate the results.

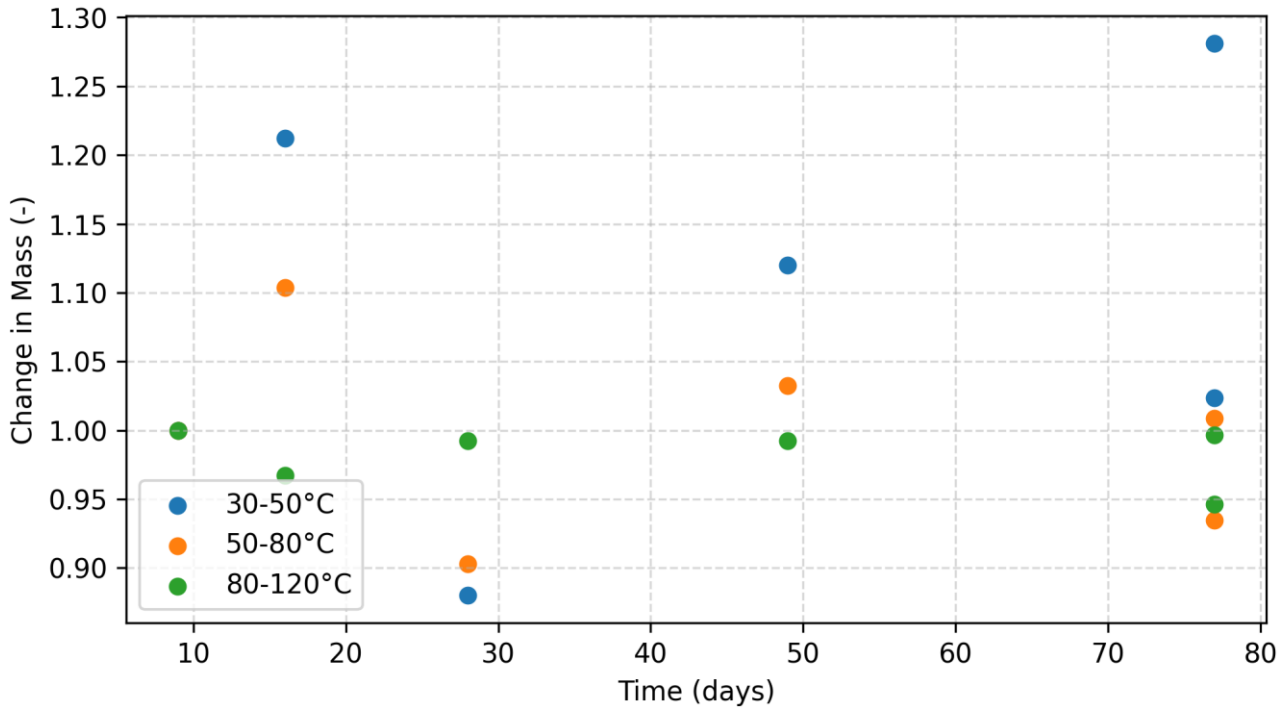

Figure 5-5 – TGA of hardener - change in mass over time

As can be seen in all three temperature ranges there is not significant change in evaporation indicating that no absorption or evaporation occurred during the storage of the hardener. To further verify that no significant change occurred another two samples were tested which were left exposed to the room air for three days. This should give these sample enough time to absorb moisture or evaporate volatile material. The results from the previous tests are averaged for this comparison. The results of these tests are shown in Table 5.6.

Table 5.6 – Change in mass of hardener after exposure to air

	%Δ Mass from 30-50 °C	**%Δ Mass from 50-80 °C**	**%Δ Mass from 80-120 °C**
No air exposure	-0.56 ± 0.07	-1.19 ± 0.09	-12.73 ± 0.25
3 days of exposure	-0.78 ± 0.07	-2.27 ± 0.15	-15.39 ± 0.70

As can be seen the change in mass for the samples exposed to air is significantly higher at all sampled temperature ranges compared to the samples tested directly after removing them from the freezer. Thus, it can be concluded that exposure to air can result in absorption of moisture into the hardener though the storage time in the freezer was not long enough to significantly affect the samples. Therefore, the observed changes in the hardener have to either be imagined

or result from a different source. This could be the additives settling or agglomerating during storage. An easy solution to this is to stir the hardener before removal from the container to homogenize the batch. The stirring should be enough to avoid differences in adhesive composition while the final mixing step will breakup agglomerates or disperse the additives sufficiently again. From these experiments it can be concluded that the used storage method for the hardener is acceptable.

5.3.3 Adhesive Mixing

For the final mixing of the adhesive the speed mixer is used with the process parameters described in section 9.1. The amount of adhesive that needs to be mixed is calculated from the volume need to fill the adhesive layer of the sample with a safety margin of around 50 % to account for losses in the mixing and transferring of the adhesive.

The resin masterbatch is mixed with the required extra resin. Then the hardener was added and mixed again. Both mixing steps were done using a vacuum of 3 mbar. Here it is important to keep the mixing time to the minimum necessary as the percolated state of the MWCNT is meta stable and the particles can re- agglomerate with prolonged mixing times when shear forces are too low in the mixing step. [Kup01] Though this should not be an issue in this study as the total mixing time is less than 5 minutes.

5.3.4 Adhesive Curing

The curing of the adhesive was performed in either an oven or a hot press for the sample production or in the autoclave for the adherend production with a temperature profile as described in the section 5.1. The curing profile for the RIMR035c adhesive is shown in Figure 5-6. For both adhesives the machine is heated at 1 K/min to 80 °C. The curing is performed at this temperature for the required time as mentioned in section 5.1, for RIMR025c it is 5 hours. The cool down rate is limited to a maximum of 1 K/min and later by the oven’s thermal insulation. Below 40 °C oven temperature the parts are deemed cold enough to remove them from the oven.

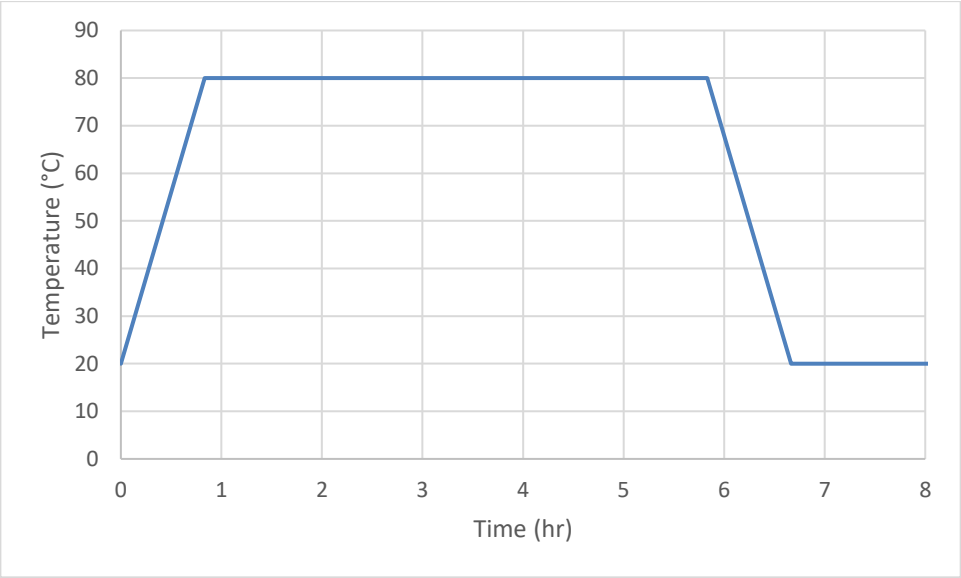

Figure 5-6 – Temperature profile for curing the RIMR035 adhesive

5.4 Adherend Production

The composite adherends for the SLS and G2C samples are produced from a unidirectional glass fiber called Saertex U-E-1200 g/m^2-1300 mm. The GFRP plate was produced using the vacuum assisted resin infusion method (VARI-) with the RIMR035 resin system. In the Vacuum assisted resin infusion (VARI-) method the vacuum pressure and capillary forces aid in the wetting of the fibers. For this a tooling die was used which is shown in Figure 5-7. The resin flows into the tool and is spread around the edges of the cloth while the vacuum is pulled from the middle. The plates were cured in the autoclave using the temperature profile described in section 5.3.4. No external pressure was applied in the autoclave. The produced plates had dimensions of about 58 x 58 cm after trimming the edges. Two layers of the 0.8 mm thick cloth is used resulting in plates with a thickness around 1.55 to 1.60 mm.

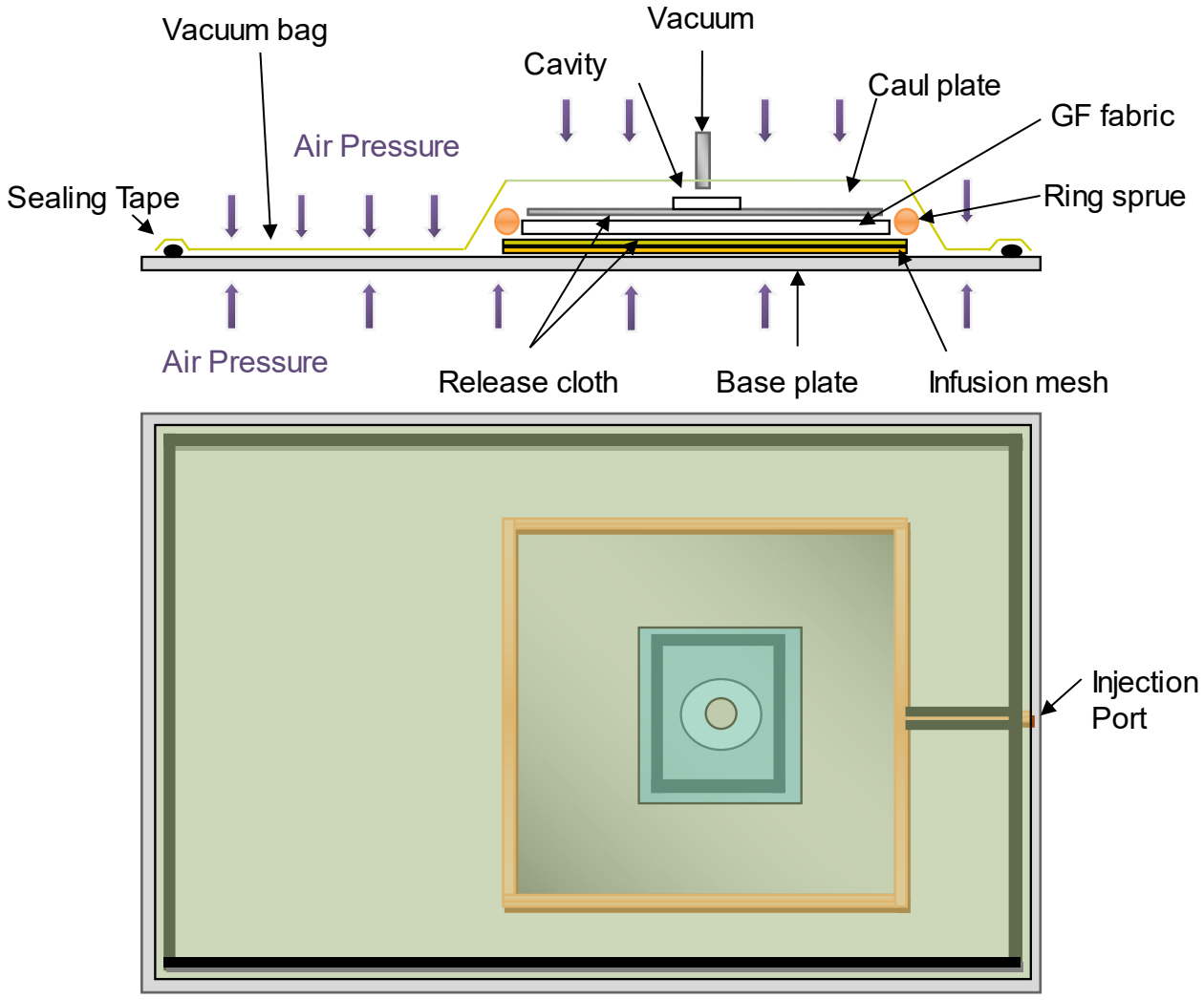

Figure 5-7 – Tooling mould for GFRP laminate production

The first five of these glass fiber laminates had no discernible issues after demoulding. After this a new batch of fiber glass material was cut for the next laminates. In these the resin did not impregnate the fiber material well leaving the entire plate looking white due to the dry spots. A few attempts to remedy this issue were made. At first it was thought that the vacuum had not been adequate, though the next attempt at producing the laminates resulted in the same problem. For the next attempt the glass fiber was heated in the oven at 120 °C to evaporate any moisture. Weighing the fibers before and after the heating showed that an insignificant quantity of water had evaporated. Additionally, a heating blanket was placed on top of the mould to decrease the viscosity of the resin while the infusion took place. This did not help impregnate the fibers. The usage of infusion meshes to improve the flow of the resin and higher temperature of the heating blanket also did not improve the result. The Saertex glass fiber material which had been used up to this point was past its expiry date, so the next laminate was produced using a new glass fiber cloth, a heating blanket, an infusion mesh as well as a significantly longer infusion time. This resulted in a small improvement. Two thirds of the laminate showed no sign of any defects. The final attempt at producing a laminate without large defects was performed without the mould on a large steel plate. In addition to the previous changes, above the caul plate a layer of VAP® foil was placed. This membrane allows air through but stops resin allowing for very long infusion times and better air evacuation. These plates had no defects, however could not be used due to time constraints

5.5 Sample Production and Testing Procedure

5.5.1 Cube Samples

The conductivity of the adhesive with varying sample thicknesses is to be determined. Following this the measurement sensitivity of the adhesive to crack formation at different sample thicknesses is to be determined. To measure this, rectangular cubes of varying thickness with a surface of 15 x 15 mm were produced. Into halve of these samples nonconductive foils are placed to simulate a crack in the conductivity measurement.

To start a smooth non-stick surface is prepared by wrapping two glass-panel with a non-stick foil. Onto these the adhesive can later be placed and cured. The two pieces are then heated in the oven to 130 °C so that the foil contracts and forms the smooth flat surface. Next the adhesive was mixed and the oven cooled back down to room temperature so that the adhesive does not experience a temperature shock during the curing step. The mixed adhesive was placed on the glass panel on the side of which were two parallels of the desired sample

thickness. The other glass panel is placed on top of these parallels and weight down with 4 kg. The setup is shown in Figure 5-8.

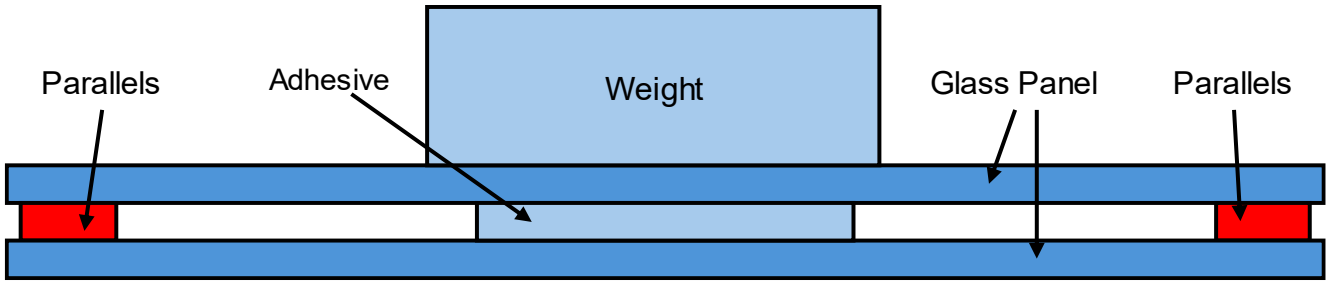

Figure 5-8 – Setup for cube sample production

To simulate a crack inside the samples a slight variation of this procedure has to be used. For this the goal is to place a non-conductive foil inside the samples. This should cover about half of the surface area and be at a depth of half the sample thickness. The production of the samples is shown step-by-step in Figure 5-9. A 20 mm strip of the non-stick and non-conductive foil is prepared by tapping it to the underside of the glass. Then about half the adhesive is placed on the glass. To position the foil, at a depth of half the desired sample thickness, two sets of parallels were used at half the sample thickness. Over the first set of parallels the foil was wrapped tightly making sure to go over the middle of the adhesive blob and glued to the backside of the glass, shown in part b. The other half of the adhesive is placed on top of the foil part c. The other set of parallels is placed on the first set and covered with the glass panel. The final result with the foil inside the adhesive is shown in part d. The adhesive is cured according to the temperature profile described in section 5.3.4. The samples are then cut using a KKS 1300 C Maiko diamond cutting saw into squares (part e) of 15 x 15 mm.

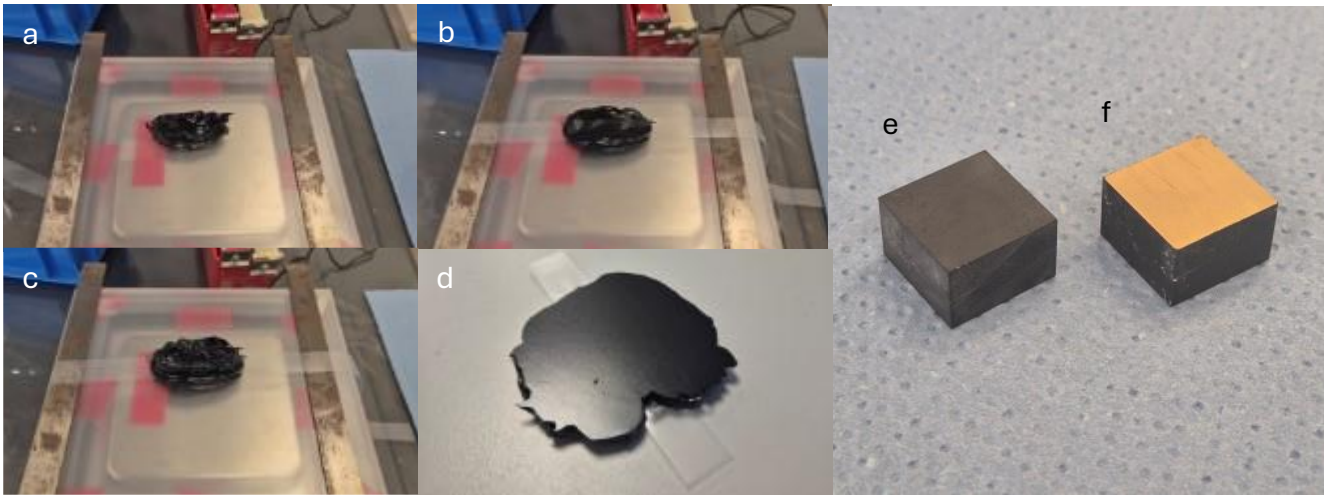

Figure 5-9 – Production steps for cube samples with simulated damage

The top and bottom surfaces of the samples can potentially have a very thin layer of pure resin which would inhibit the electrical current. Thus, the samples where lightly sanded using 600 grit wet sandpaper. The samples where then cleaned of any sanding residue and oil using a water rinse followed by isopropanol. The sides of the samples were wrapped in tap to avoid applying the contact coating on them. Using the Sputtering machine E5100 Autocoater, shown in Figure 5-10 from ingbuero liebscher a 100 nm layer of gold was applied which is shown in Figure 5-9f, which will simulate the contact material.

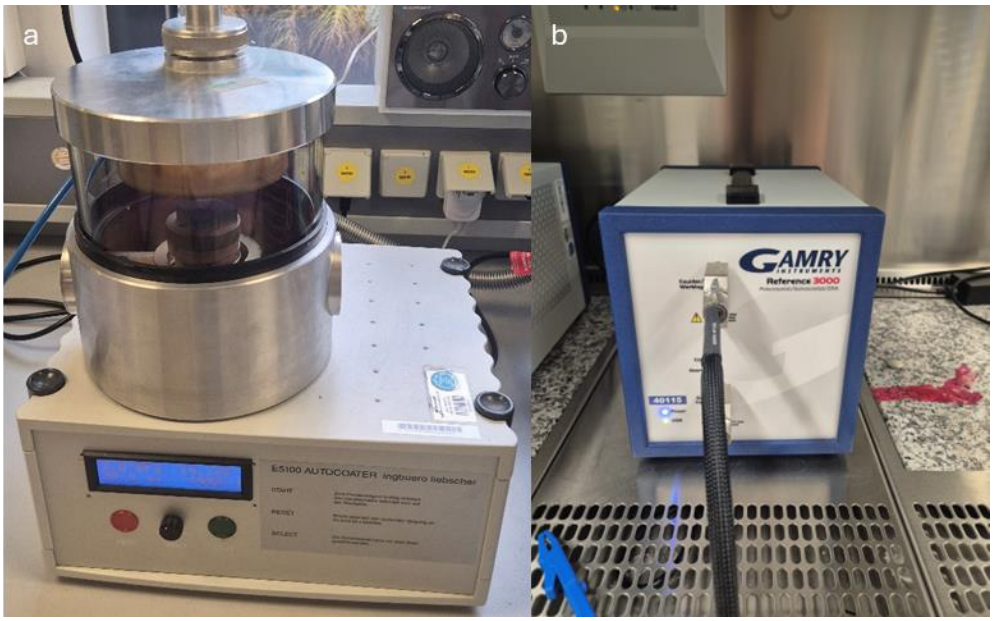

Figure 5-10 – a. Sputtering system - autocoater from Ingbuero Liebscher, b. Potentiostat from Gamry Instruments

The samples dimensions are measured using a micrometer. The thickness was measured at 5 points (one central and one on each corner). The length and width of the samples was each measured twice. Following this the average of these measurements is taken to determine the height, width and length of the samples.

A Reference 3000^{TM} potentiostat/galvanostat/ZRA from Gamry Instruments was used for the measurements. A four-point measurement method is used to measure the resistance. The sample is held during the measurement in a fixture (show in Figure 5-11). Across the sample a current of 1 mA is placed and the voltage is measured. 20 measurement point where collected 0.5 seconds apart and then averaged. The resistance is measured using a multimeter as a backup and function check of the potentiostat. For this the sample is held with a modified clamp where the jaws have a copper sheet attached with a wire leading to the multimeter.

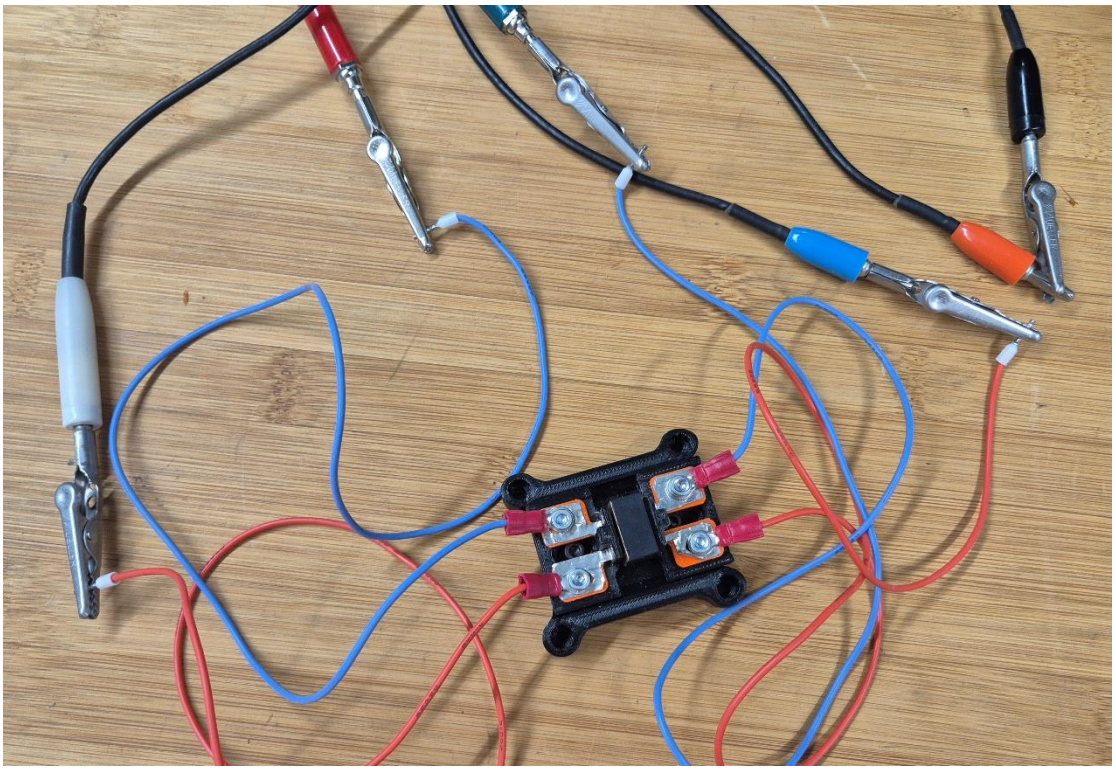

Figure 5-11 – Potentiostat fixture for cube samples

5.5.2 G2C samples

The G2C samples where produced based on the DIN EN 6034 and AITM 1.0006 standard. Deviations from this standard had to be made due to material availability of the adherend and the wire mesh used in the samples. The typical method of producing these samples is to cut them out of the tested G1C samples so that the crack is in the correct position. However, in previous experiments at the DLR it was found that G1C tests with mesh result in high variations in results, while G2C tests result in more precise results. Thus, for these experiments G1C samples were not tested and instead G2C samples had to be directly produced. For each parameter a plate was produced from which the samples were cut.

Rectangular GFRP plates were cut with a size of 250 x 120 mm. This is long enough to ideally produce 8 samples, with one sample being reserve should a sample be defect. The plates where lightly sanded to remove the top layer of epoxy, cleaned and then clamped together. In opposite corners two holes were drilled about 5 mm away from the edge. These are used to index the plates together using two pins. The two plates are marked to remember the orientation with a pen. This way the plates can be stored in pairs for the bonding later.

To prepare for the layup a few items where cut to size beforehand. The wire mesh was cut to 230 x 120 mm. The release film was cut to 230 x 45 mm. Four 0.5 mm thick and 12.7 mm wide

spacers where cut to 110 mm length. The burrs on the spacers were also removed. All of these items were wiped down with isopropanol before the bonding.

For the layup of the samples a tool was designed and 3D printed out of PETG to aid in the application of the adhesive while keeping the spacers and CFRP plates in from moving. The layup and final sample can be seen in Figure 5-12. To start a batch of 70 g of adhesive was mixed according to the procedure described in section 5.3.3. For all the G2C samples the same two master batches of Resin with MWCNT and Hardener with Aerosil and glass fiber was used.

A GFRP plate was placed on the tool and an adhesive layer of 1.5 mm thickness was applied. The final adhesive layer is between 0.9 and 1.0 mm thick due to the metal mesh is placed inside it. This results in a final sample thickness of 4 mm which is outside of the specification of the AITM 1.0006 standard.

The first plate is set to the side and the other plate placed into the tool. The second plate was covered in a thin layer of adhesive, just enough to keep the wire mesh and the release film in place during the layup. About 10 mm of adhesive was removed where the spacers are placed and pins inserted into the holes. The wire mesh is placed on the plate in the tool and aligned with one edge. Then the release film is placed on top and also aligned to the edge of the CFRP plate. The other plate is stacked on top and using a hammer near the pin holes gently pushed down until the spacers touch the plate. A metal plate with two holes drilled at the pin location is placed on top as the pins are longer than this stack. This entire setup is then placed inside a hot press where the adhesive is cured using temperature profile described in section 5.3.4 a force of 3 bar is applied to press out the excess adhesive.

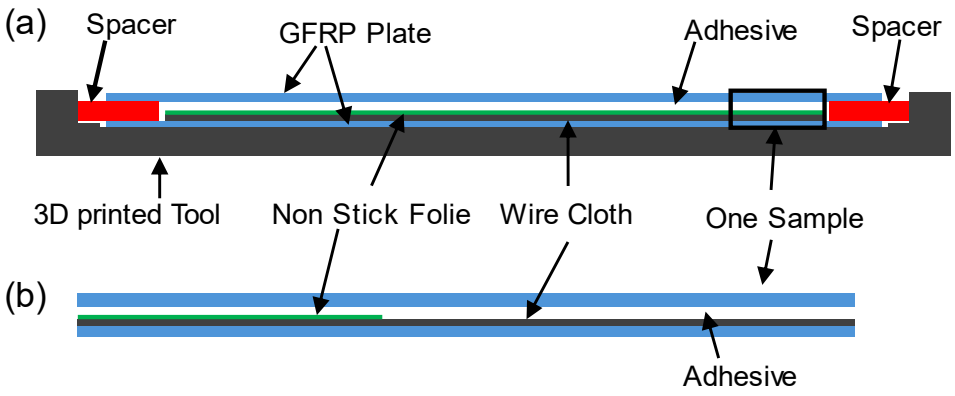

Figure 5-12 – a) front-view of G2C Layup, b) side-view of G2C sample

The unmodified RIMR035 adhesive is not viscous enough to produce the samples through the above-described method. These samples were produced by using a casting. On one GFRP

plate the non-stick foil is taped. The GFRP plates and spacers are assembled and the edges are tapped leaving one side open for the pouring. This assembly is then clamped between two aluminium plates, so that the open side is on top. With some tape a slit is created to make it possible to pour into the 1 mm wide gap. This assembly is then placed inside the oven and the adhesive cured.

After curing the plates are cut into a 25 mm wide samples. After that the samples need to be cut to length as the release film and the plates are longer than necessary to account for movement during the curing. The release film moved especially much for the samples with the S2 wire cloth and had to be redone. The release film needs to be only 40 mm long. However, due to the wire mesh it is not possible to see the release film with the eye. Therefore, the end of the release film is marked using a pen under the microscope. Then the samples can be cut shorter. The samples are then around 115 mm long which is longer than the minimum required of 110 mm.

The width and length of the samples are measured using a vernier caliper at 3 and 1 points respectively. The thickness is measured at 3 points using vernier callipers. Using the microscope a picture is taken of the sample and the distance between the sample edge and the end of the non-stick foil is measured.

Samples for each of the wire cloths applied into the modified adhesive were produced. Reference samples without wire cloth were produced using the modified and unmodified RIMR035 adhesive and the BPR adhesive.

The samples were tested using a Zwick Roell universal testing machine, using a three-point bending fixture with a span of 100 mm. A force transducer capable of 5 kN is used to measure the force applied. The Experimental setup is shown in Figure 5-13.

The samples are marked with a pen 5 mm above the end with the foil. The samples are placed onto the fixture and the marking is aligned with the support. A constant displacement speed of 1 mm/min is used.

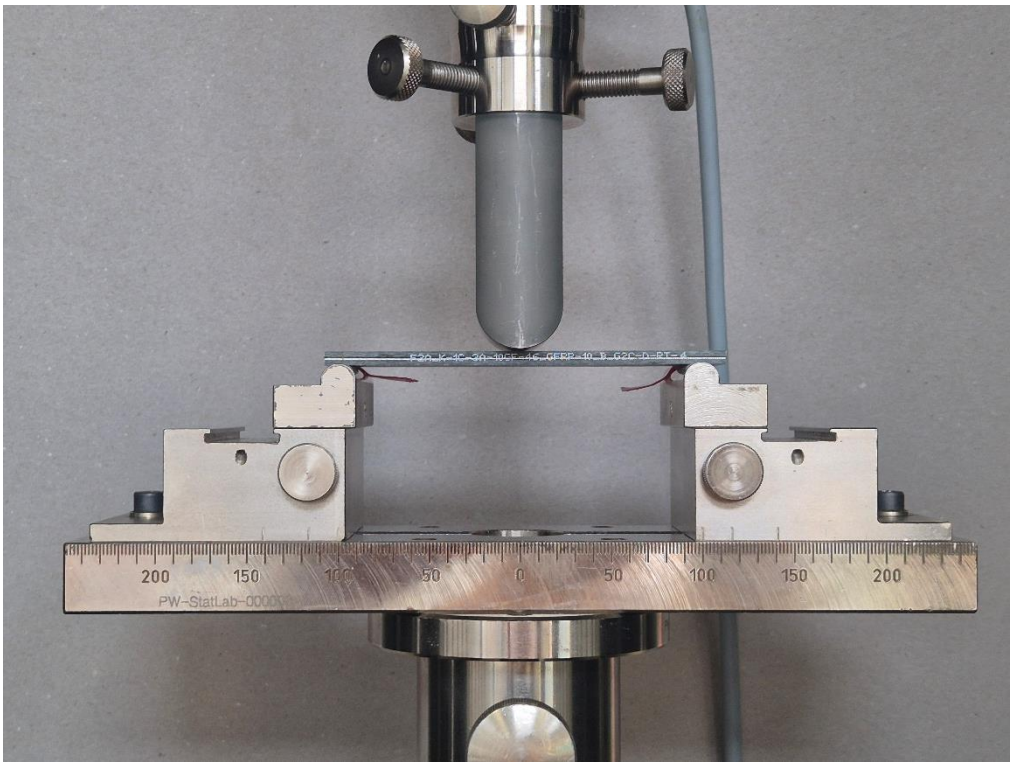

Figure 5-13 – G2C experimental setup

5.5.3 SLS samples

The SLS samples are produced and tested based on the DIN EN 1465 standard. The purpose of these SLS experiments is to find out which material is best suited for long duration dynamic loads. The result of these experiments is ideally a SN-Curve (Wohler diagram) which details the strength of the different adhesives and wire cloths at different load cycles.

For each set of samples, the following material was prepared. The GFRP plates are cut into 4 pieces. 2 pieces have the dimensions 28 x 10 cm, while two pieces have the dimensions of 28 x 3.75 cm. The latter are used as shims so that alignment in the testing machine is simple. Six spacers of length 37.5 mm and three spacer of length 12.5 mm are cut on a metal shear. Both spacers have a width of 12.7 mm and a thickness of 1 mm. The burrs are removed using a plate grinder. One side of each GFRP sheet is sanded using 320 grit sand paper. Holes are drilled for pins in the corners where these pieces will overlap. The sheets of adherent are alignment using a 50 mm long plate, so that an overlap length of 12.5 mm is achieved. The holes for the joint overlap are then drilled with the assembly firmly clamped. The free length of the adherends is covered with tape so that excess material doesn't impact the test results. The samples, spacers and wire mesh are cleaned with isopropanol until no residue is seen on the paper towel. 45 g of adhesive is mixed as explained in section 5.3.3. 10 g are set aside for the joint. The rest is applied onto the two adherends where the shims will go. The adhesive is

levelled using a scraper. Where the spacers will sit the adhesive is scraped away. Two spacers are placed on the sides and one in the middle. Following this the shims are placed on top and using a hammer the pins are pushed through the holes. The 10 g of adhesive from earlier is placed in a continues bead across the length of the joint area, without scrapping flat. This excessive application of adhesive and limited handling of the adhesive ensures that any air bubbles are pushed out of the joint. The pins and spacers are placed similarly as described above on this section. Finally, the two halves are joint and the pin hammered in place. During this procedure excess Adhesive is removed after each step to keep the work place tidy. This assembly is then placed in the hot press, where first the sample is pressed and excess adhesive removed one final time. Then the curing procedure from section 5.3.4 is followed with a pressure of 3 bar. Eight 25 mm wide samples are cut from the produced boards. The excess adhesive is finally carefully removed using a chisel and the tape is removed. The produced samples dimensions are measured using a micrometer and documented.

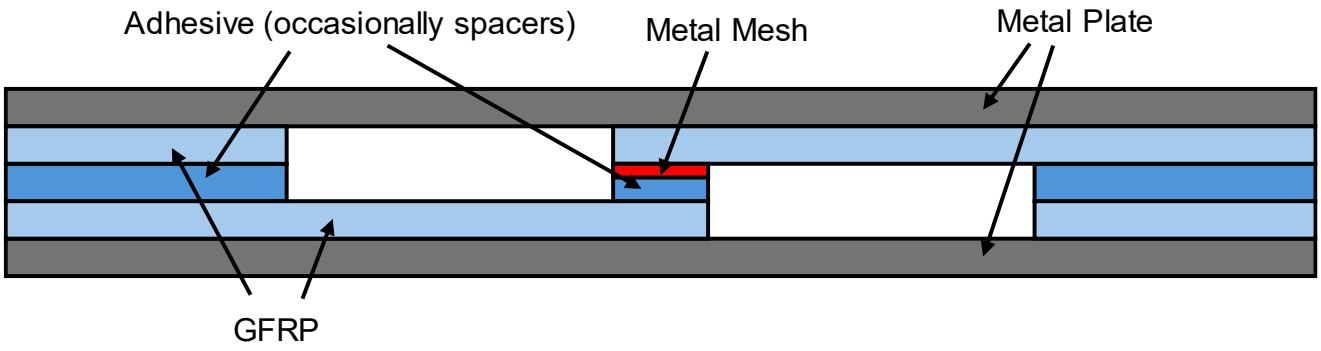

Figure 5-14 – Cross-section of SLS sample production

Samples were produced with the BPR reference adhesive, the modified RIMR035 adhesive without wire cloth and with the steel wire cloth. Due to poor results from the first samples tested and a lack of adherent material no other cloth material was tested.

The samples were tested using a LTM10 electrodynamic testing machine from Zwick Roell. The test setup is shown in Figure 5-15. A load cell measures the force during the experiment, while the Pyrometer CTL-CF2 from Micro Epsilon (on the right) is used to record the temperature of the sample. A camera (on the left) is used to image the sample throughout the experiment to monitor any crack formation and propagation or delamination.

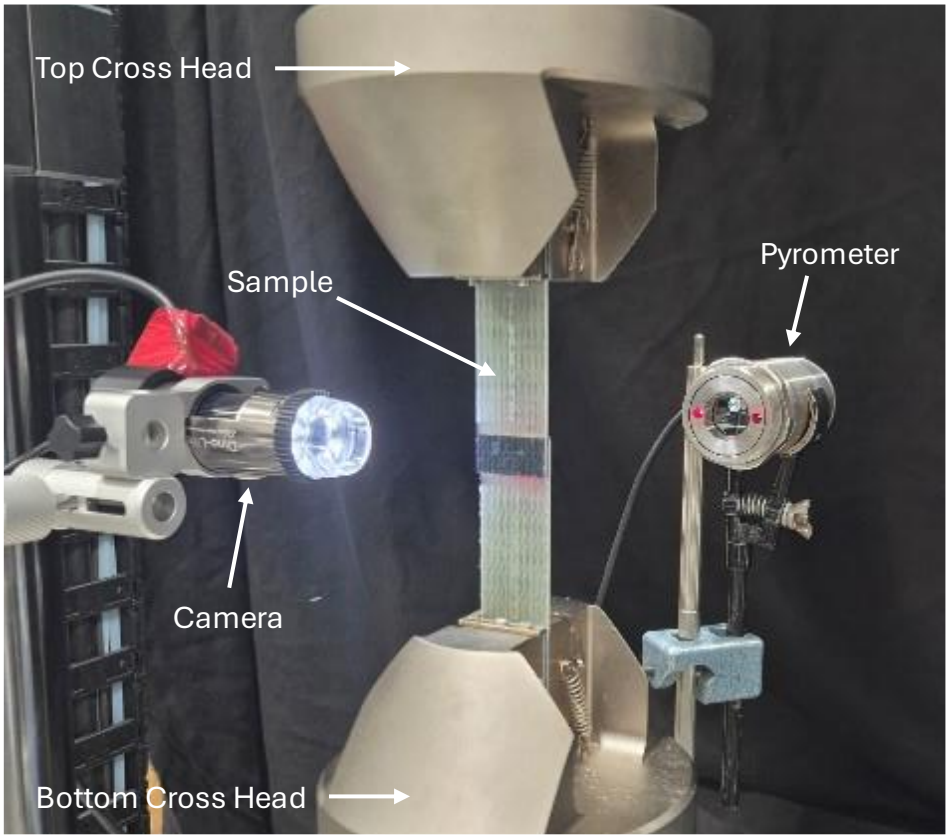

Figure 5-15 – SLS experiment setup

For each of the adhesives, four samples were tested statically until failure with a displacement rate of 1 mm/min. During these tests the samples are filmed.

The dynamic tests were conducted using the pearl string method, as insufficient data and experience was available to apply the horizon method; in such cases the pearl string method is recommended by [Mül15]. The calculated maximum shear stress from the static tests is used to calculate the forces used during the dynamic tests. The maximum force applied was incrementally decreased from sample to sample until enough data points have been acquired.

A stress ratio of 0.1 and a frequency of 3 Hz is used during these tests. Measurements are taken with varying sampling intervals to reduce the amount of data collected for high cycle tests. The force and displacement are measured using a sampling rate of 100 samples per second. A cycle is recorded at progressively increasing sampling intervals. The first 10 cycles are recorded at intervals of 10 cycles. The subsequent 10 cycles are recorded at between intervals of 100 cycles and so on. The imaging interval is calculated using an estimated fatigue limit using data from previous experiments and the load applied during the experiment. This fatigue limit estimate is then used to adjust the sampling intervals so that the samples ideally fail when 20-50 pictures have been taken.

5.6 Conductivity Demonstrator

The conductivity demonstrator is going to be used to tests various damage configuration and attempt to localize the damage. For this a GFRP with electrically conductive elements in different patterns is needed. An attractive option to realise this accurately and fast is the use of PCBs designed with the contacts for the adhesive and attachment points for the measurement devices. Invent GmbH, a project partner, has designed and written code for the measurement device which will be used for this. There are three different types of failure which are going to be investigated, adhesion, cohesion, and mixed failure, for each of these a demonstrator part was produced.

A PCB with square contacts measuring 40 x 40 mm was used. Four of these contacts were placed in a row with a distance of 40 mm between the contacts. Multiple rows were placed on each PCB with a separation of 10 mm, to reduce the quantity of the glue ups necessary. For the top three rows the vias (a connection from one side to the other of the PCB) are in the middle of the contacts. While the bottom row has the vias near the edge of the contacts. With this the effect of measurement location can be determined. The PCBs were designed in KiCad and ordered from Aisler B.V.

To maintain a consistent adhesive thickness a 3D printed part made of PETG was utilized with a thickness of 4mm. A diagram of the 3D printed part can be seen in Figure 5-16. In addition, this part also has horizontal beams of 10 mm width between the four rows of measurement areas. Due to the non-conductive nature of PETG this should isolate the measurements rows from each other reducing the impact the other rows have on the measurement. To aid in the alignment of the PCBs over each other, the part has tabs on each corner which form a rectangle into which the PCB fits. The tabs for the top PCB are printed separately and inserted into V-groves, through this the overhangs are eliminated leading to reduced material usage and improve surface finish of the 3D printed parts. This was deemed necessary to reduce the electrical conductance through the gap between 3D printed part and PCB. To allow excess adhesive to flow out of the part the height of the part is reduced at the end of the rows.

The adhesive for the demonstrator was mixed according to section 5.3.3. To fill the rectangular slots the adhesive was moved into a cartridge from the mixing container and a 3D printed nozzle (diagram in appendix 9.3) was used to dispense the adhesive evenly across the 40 mm channel. The produced bead of adhesive is a little thicker than 2 mm and two beads are enough to fill the 4mm high adhesive layer with enough excess material to fill the corners of the channels.

Figure 5-16 – Demonstrator part during glue up with foil and 3D printed part visible

For both the adhesion and cohesion failure modes the same damage location and sizes were used to be able to compare the results, the difference is the location within the adhesive layer. The foils in the adhesion demonstrator are directly in contact with the PCB while in the cohesion demonstrator they are in the middle of the adhesive layer. The location of the failures is shown in Figure 5-17. The blue squares represent the contacts while the red rectangles are the foils placed in the demonstrator. The second column of contacts is not disturbed with any damage so that a reference resistance can be measured for each row. Foils covering 33, 67, and 100 % of the contact area are placed in column one to identify the effect of size on the resistance. On the right various damages are placed next to the contact area to identify if damage which is not directly in contacting the electrical contacts can be detected. Lastly in the fourth row the same area of the contact is covered though at different distances to the via pass through, this simulates the distance to the measuring device.

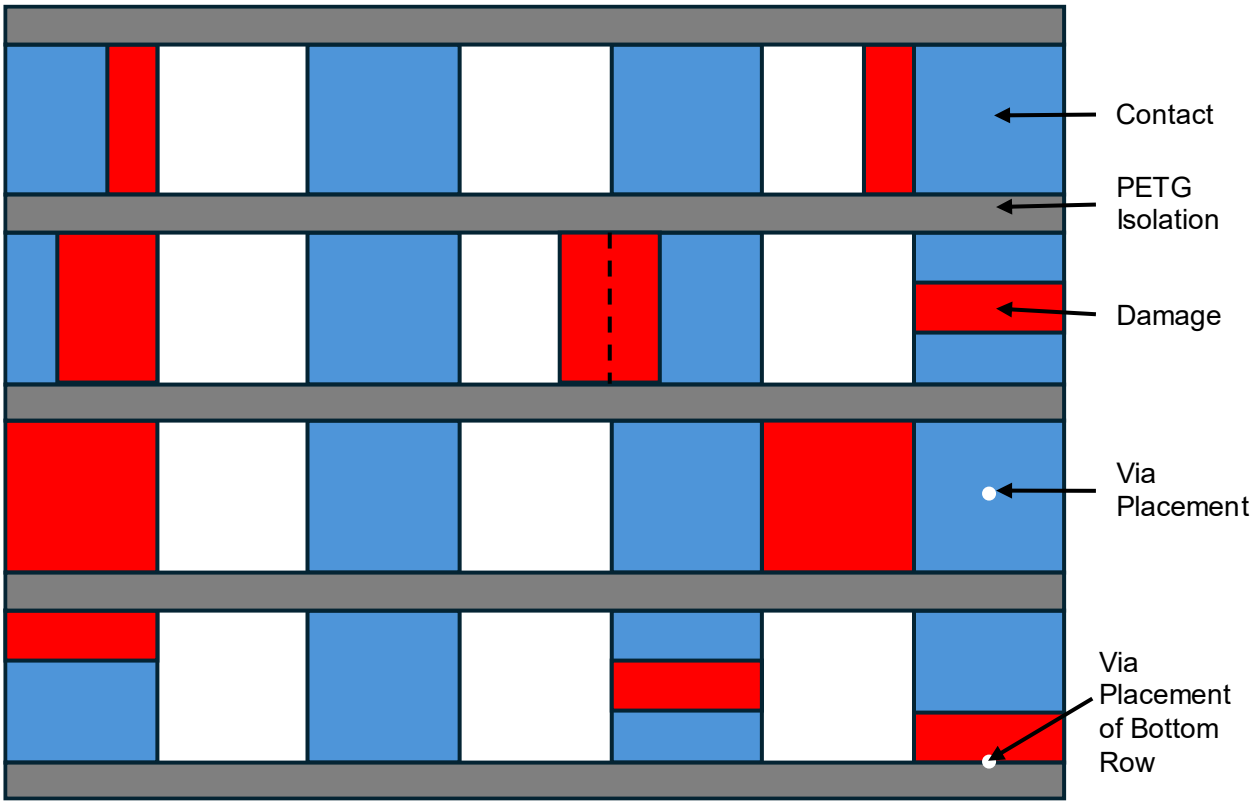

Figure 5-17 – Location of simulated adhesion and cohesion damage

The failure location for the mixed failure mode is shown in Figure 5-18. The orange lines indicate were a crack perpendicular to the parts runs, so from one side of the adhesive layer to the other. While the red rectangles represent a crack parallel to the PCB at the interface. The expected difficulty in locating these failures means less different sizes of damage were investigated instead different location and orientations were looked at.

The glue up process is as follows. The contact points were covered in tape to avoid adhesive moving through the vias and producing a thin insulating layer on top. The PCB was cleaned to remove any oil or dirt using isopropanol. The PETG part was placed on top. Two layers of adhesive is applied while noting the following. To simulate the cohesion failure a foil is placed on the first layer of adhesive. For the adhesion failure a foil is placed after applying the second layer of adhesive. For positioning of the simulated damage, the PETG part has groves which indicate were the inserts are supposed to be placed. Non-conductive foil is used to simulate the adhesion and cohesion failure modes. The remaining PCB is placed on top. Following this the part is cured using a hot press applying 3 bars of pressure following the process described in section 5.3.4. To test and develop this procedure small parts were produced with leftover material from previous studies. From this it is known that the foils move little due to the excess material which is pushed out of the sides.

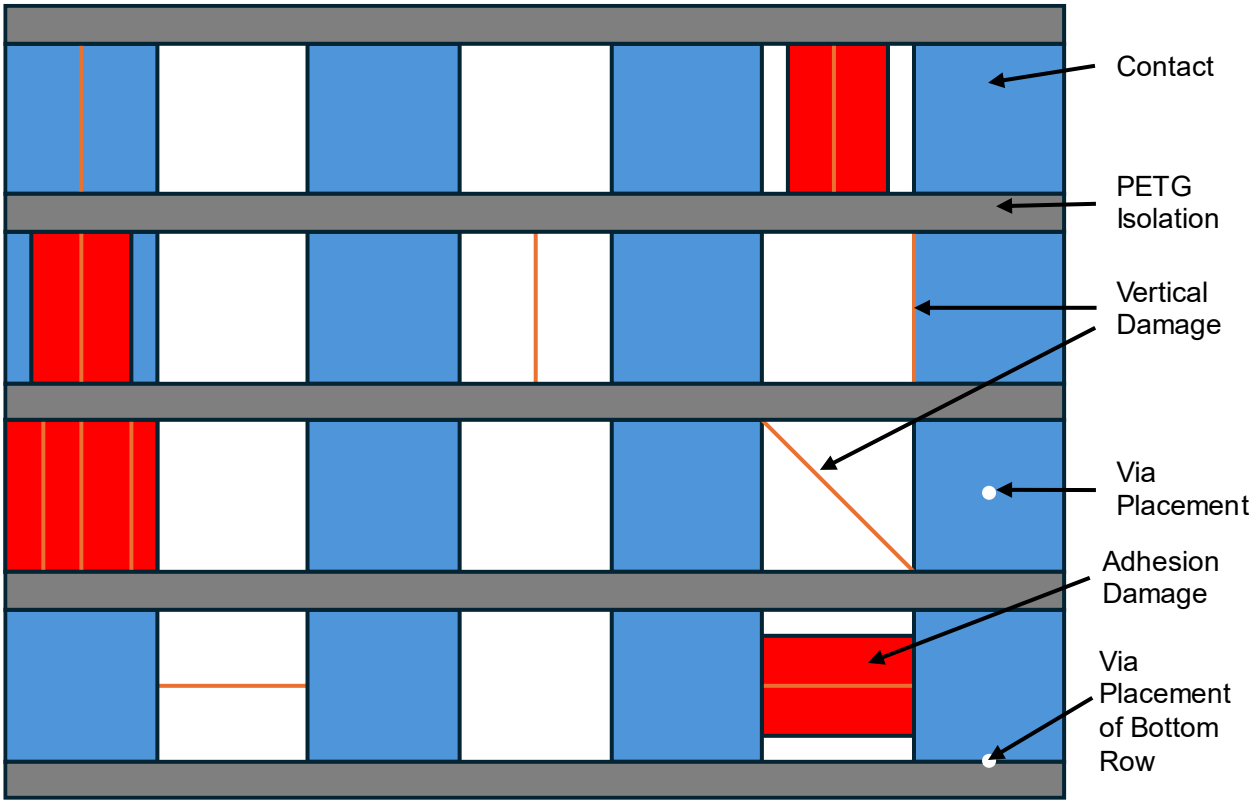

Figure 5-18 – Location and shape of simulated mixed failure damage

For the mixed failure mode demonstrator, the inserts are 3D printed from PETG to produce the 3D shape accurately. The same general procedure as above is used to produce this part however the inserts are placed while the first layer is placed. This prevents cavities from forming in the isolated areas between where the crack jumps between the adherends.

A multimeter and a SHM system were used to measure the resistances in the demonstrator parts. The multimeter was used to verify if the SHM system could reliably measure the resistance.

The SHM system (measurement path shown in Figure 5-19) was developed at INVENT Innovative Verbundwerkstoffe Realisation und Vermarktung neuer Technologien GmbH. The system is based on a voltage divider to determine an unknown electrical resistance based on the voltage measured. The integration of 2 analogue multiplexers (MUX1 & 2) with 16 channels enables the measurement of multiple conductions paths. The demonstrator is placed between these two MUX and each contact point is connected to both. The change of electrical resistances based on the path may be used to localize a defect inside the adhesive bound under the condition that the undamaged reference state is known. From the multimeter measurements the resistances in the parts are known a priori and the reference resistances

can be chosen and connected to MUX 3. To ensure adequate sensitivity and a low measurement error R_x, the reference resistance, should be of the same magnitude from the measurement paths resistance i.e. $0.1\ R_1 < R_x < 10\ R_1$. As there is a wide variation between the resistances in the part multiple reference resistors are used to account for this high variety which are connected through MUX3. The resistors used in for the measurement of the demonstrators are 33, 100, 333, 1k, 3,3k and 10k Ω. A high overlap between the resistors is used to test the error and sensitivity of the system.

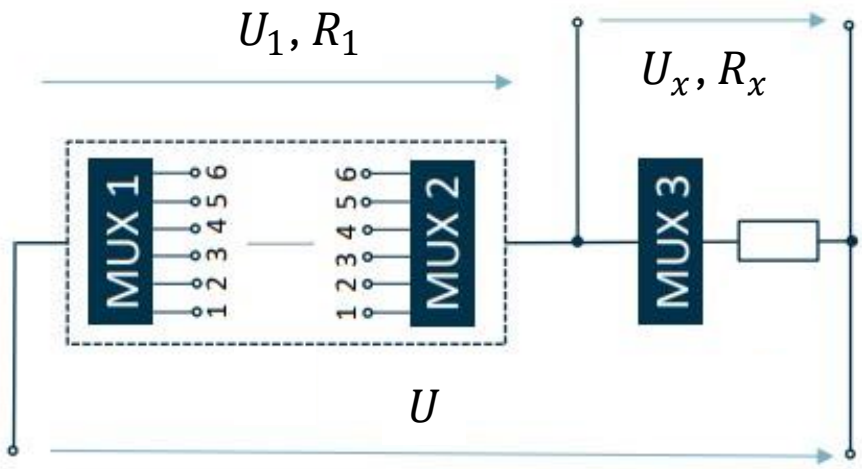

Figure 5-19 – Schematic of SHM measurement system

This SHM measures the voltage U_x over the reference resistor for each combination of points between MUX 1, 2 and 3 at a sampling rate of 10 ms, while continuously saving these measurements to the computer. To calculate the resistance in the part the voltage across the reference resistors is measured. The resistance can be calculated with the known supplied voltage U from the power supply of 5 V using the following formula:

$$R_1 = \frac{R_x(U - U_x)}{U_x} \quad (2)$$

6 Results

In the following chapter, the results of the mechanical investigations conducted on adhesive bonds with embedded wire meshes and the electrical investigations are presented and analysed. The influence of sample thickness, mesh geometry and material on fracture toughness, and fatigue behaviour is examined, alongside the detectability and localization of different damage modes using resistance measurements. Additionally, the performance and limitations of the multiplexer measurement system are evaluated.

6.1 Conductivity Measurements (Cube samples)

The first parameter which was investigated is the thickness of the adhesive layer. For the pure adhesive the thickness should not have an influence on conductivity as it is a material property, thus for samples of different thicknesses with only adhesive a linear increase of the resistance is expected with increasing sample thickness. However, should a small crack appear in the sample the current flow is hindered. How this impacts the resistance is unknown. For samples with higher thickness the same crack dimensions will account for a smaller volume fraction, thus it is believed that it will contribute less to the overall resistance of the sample leading to lower sensitivity and detectability of the cracks. Two sets of samples were produced and tested as explained in section 5.5.1, to investigate the influence of the sample thickness on the detection sensitivity.

In Figure 6-1 the calculated conductivity for the samples without a crack and samples with a crack covering 50 % of the cross-section are shown in relation to the thickness.

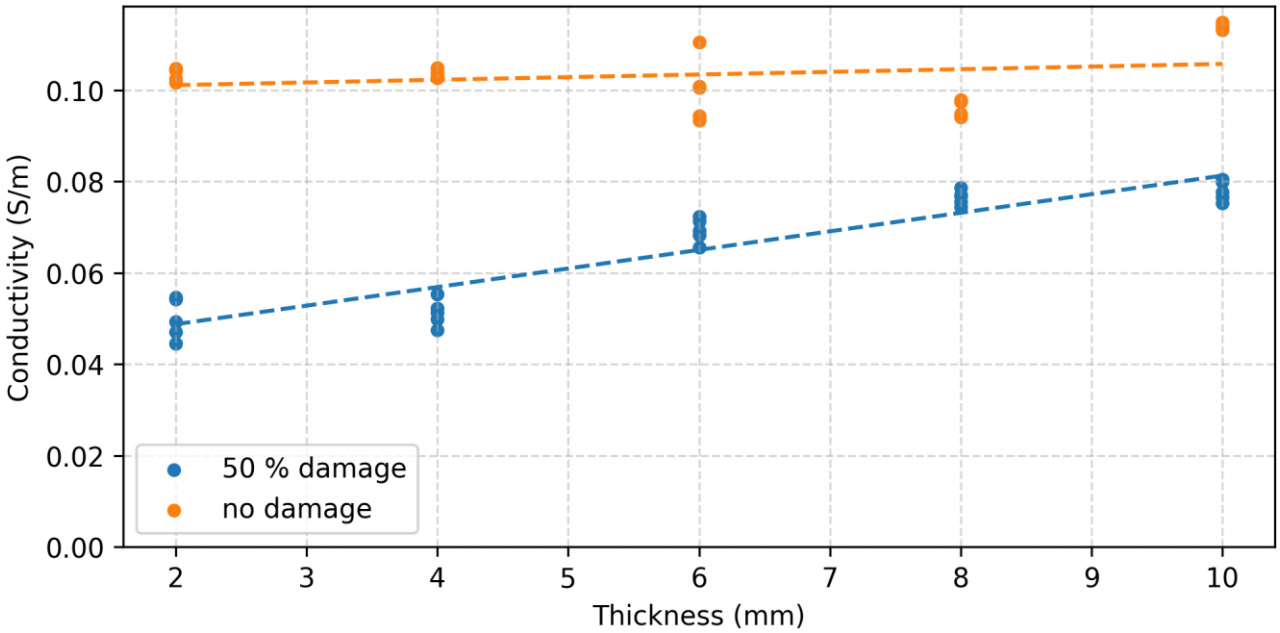

Figure 6-1 – Conductivity of samples with and without crack over sample thickness

The undamaged adhesive samples had a nearly constant conductivity of 0,1 S/m with increasing thickness with slight variance. This can be attributed towards small voids inside the samples, which were spotted in some of the samples, especially the thicker samples. The chance of voids to occur is even greater for the samples with the non-conductive foil as there are now 4 interfaces where air can be trapped during the production. The crack covering 50 % of the cross-sectional area increased the resistance, resulting in a decrease in conductivity compared to samples without a crack.

The sensitivity of the samples is calculated as $\Delta R/R_0$ where ΔR is the difference in resistance between the undamaged crack and the damage crack and R_0 is the resistance of the undamaged crack, this is shown in Figure 6-2. There is an inverse relationship between bond thickness and sensitivity to damage.

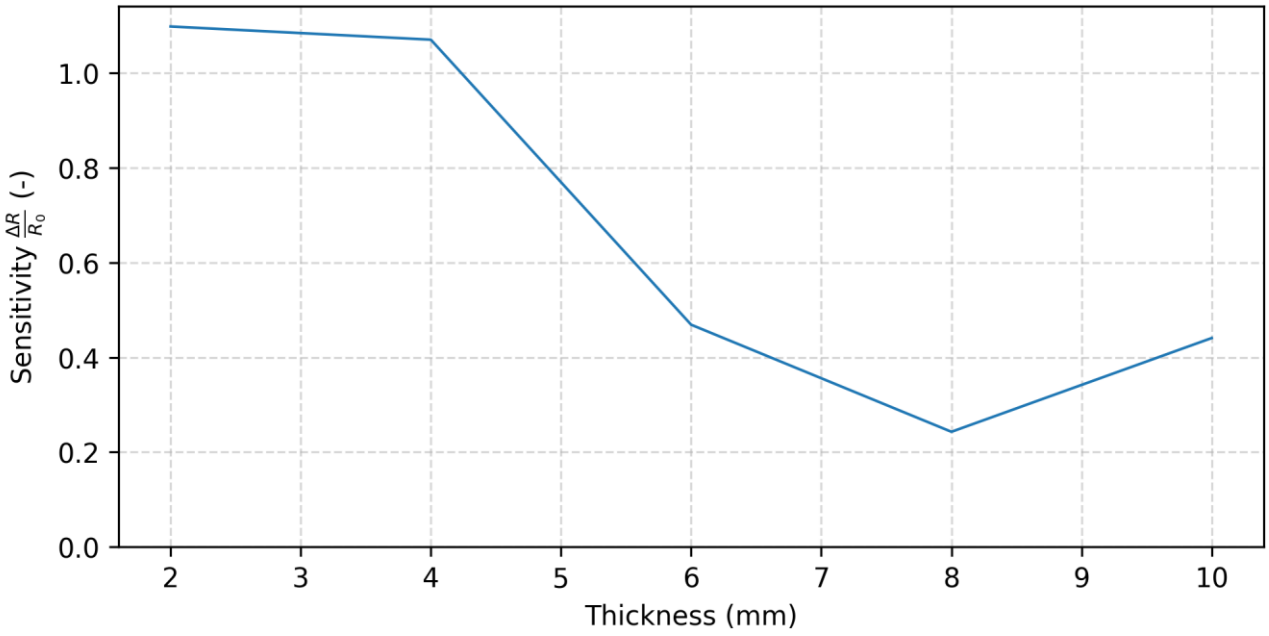

Figure 6-2 – Sensitivity of adhesive to damage covering 50 % of cross section over sample thickness

The detection sensitivity decreases with sample thickness. The sensitivity remains high for 4 mm thick adhesive layers. Thus, this thickness is used for the demonstrator parts to have a best-case scenario in which the detectability and localization can be tested.

6.2 Fracture Toughness (G2C Experiments)

G2C samples were tested to determine how the metal mesh properties impact the fracture toughness. This experiment measures how much energy is needed to start the crack propagation under shear loads.

In the samples a thin foil is placed to start the crack. The placement of this foil is important as it can determine the type of bond failure which is initiated. The length of this foil is measured using a microscope. During this, the adhesive layer is also examined. A representative set of samples is shown in Figure 6-3.

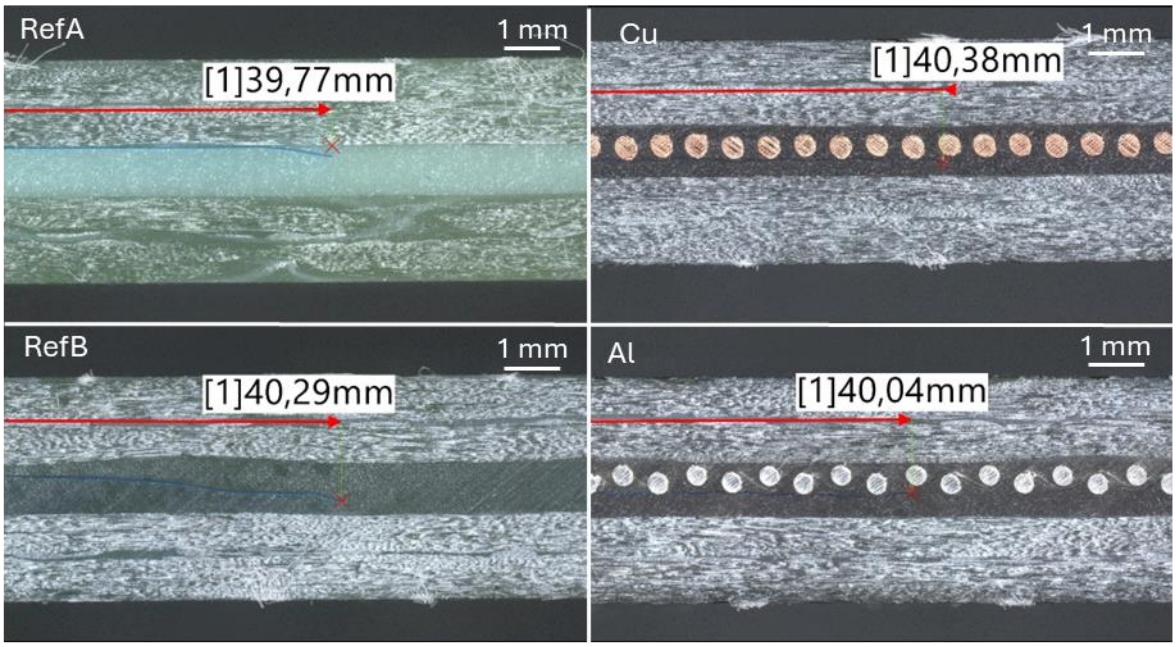

Figure 6-3 – Cross-section a small selection of G2C samples showing foil position

For the samples with a wire mesh the foil is not firmly attached instead only placed on top of the mesh, meaning the crack will not start directly attached to the wire mesh. Still, it is completely inside the adhesive layer, not touching the adherend of the sample meaning cohesive bond failure will be initiated. The foil could not be placed in the middle of the adhesive layer in the RefA and RefB samples, thus it is often laying on the adherend. Adhesive can flow below the foil due to movement of the adhesive as the samples are pressed, meaning some samples had the foil in the middle of the adhesive layer. In RefC with the unmodified RIMR035, the flow of the adhesive pushed the foil into the middle of the adhesive layer for all samples.

For consistency the samples were tested with the wire mesh on the bottom of the adhesive layer and for the samples without the wire mesh with the foil at the bottom. The samples were tested until adherend failure determined by a significant drop of the force. The rate of displacement was constant at 1 mm per minute, while the force is recorded. As an example, in Figure 6-4 the force is plotted over the displacement of the samples for the S4 steel. The first drop in force and the maximum force is shown by red and green dots respectively.

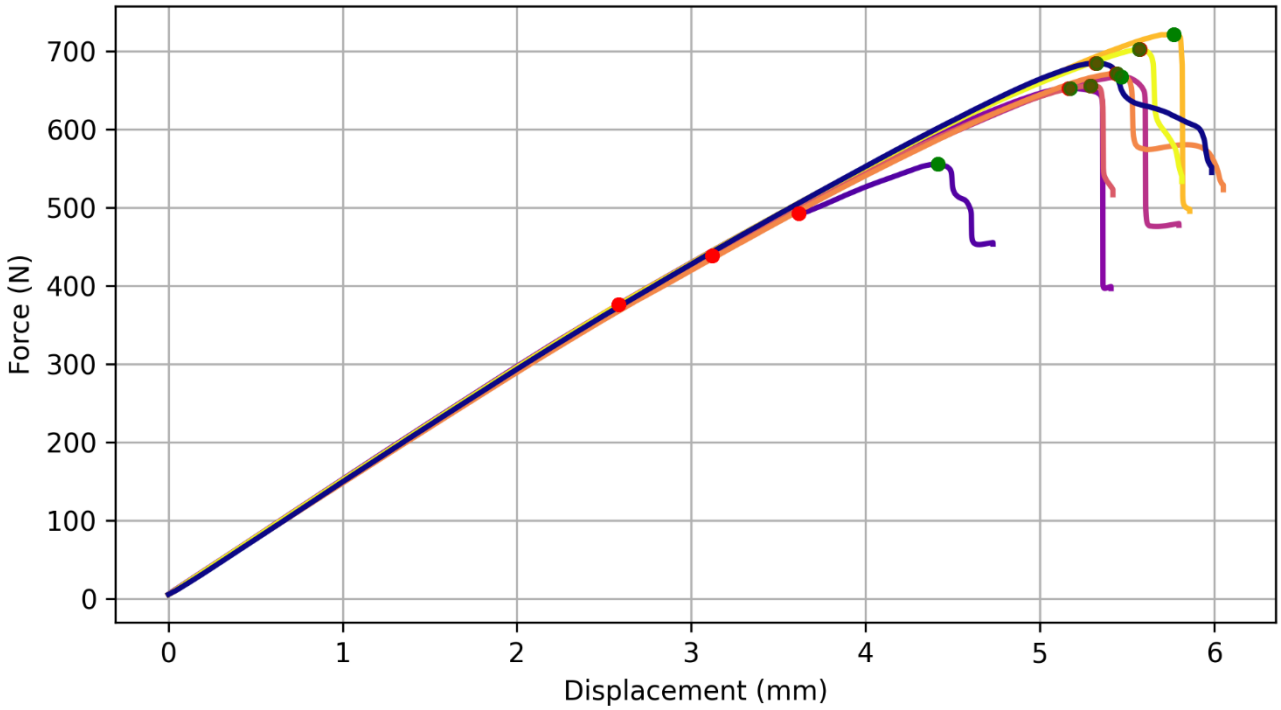

Figure 6-4 – Force over displacement for 8 G2C samples with Cu Mesh, first drop in force marked by red dots, maximum force marked by green dots

In this figure, the first small drop in force, also known as the onset point, is noticed after which the force continues to increase with the same slope, indicating that the structural integrity of the sample has not been impacted. This drop doesn't occur consistently within each sample series or at all. The fracture toughness is calculated according to the following formula:

$$G_{IIC} = \frac{9Pa^2d}{2w\left(\frac{1}{4}L^3 + 3a^3\right)} * 1000 \quad (3)$$

Where:

G_{IIC} is the fracture toughness (J/m^2)

d is the displacement at crack delamination onset (mm)

p is the critical load to start the crack (N)

a is the initial crack length (mm)

w is the width of the sample (mm)

L is the span length (mm).

Figure 6-5a shows the fracture toughness depending on different metal meshes, grid sizes and wire diameters. As can be seen there are a few series were this is consistent while others have

very significant variation. These results cannot be used to evaluate the effect of the wire mesh as the standard deviation is too high due to the previously discussed issues with identifying the onset point. Going forward for the following analysis the maximum force will be used to compare the samples. This will be a deviation from the AITM 1.0006 standard used for the testing, however it leads to cleaner more comparable results as can be seen in Figure 6-5b.

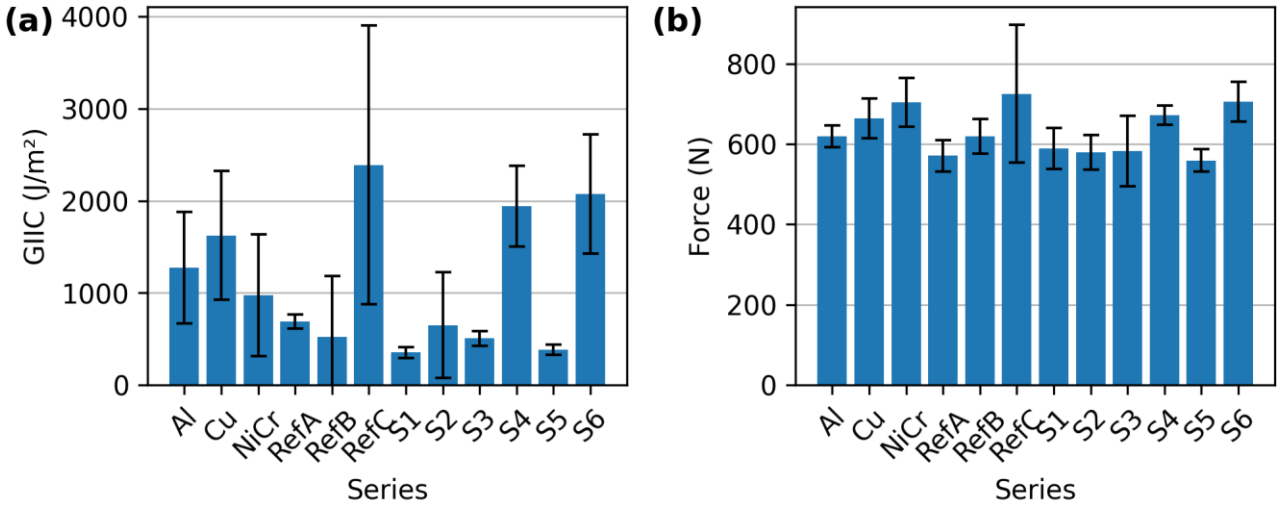

Figure 6-5 – a) G2C Fracture toughness and b) maximum force for all G2C samples

The maximum force for the various wire meshes and the references are shown in Figure 6-6. The trend lines are calculated using weighted least squares[1] to account for the highly variable standard deviations in these experiments. The p values which are derived from these calculations show the significance of these results and are related to this trendline. The r values are also shown though these values are not weighted and thus also not related to the trendline. Instead, they show how the average values correlate with the maximum force.

[1] Weighted by the standard error (SE) with the weight being $1/SE^2$

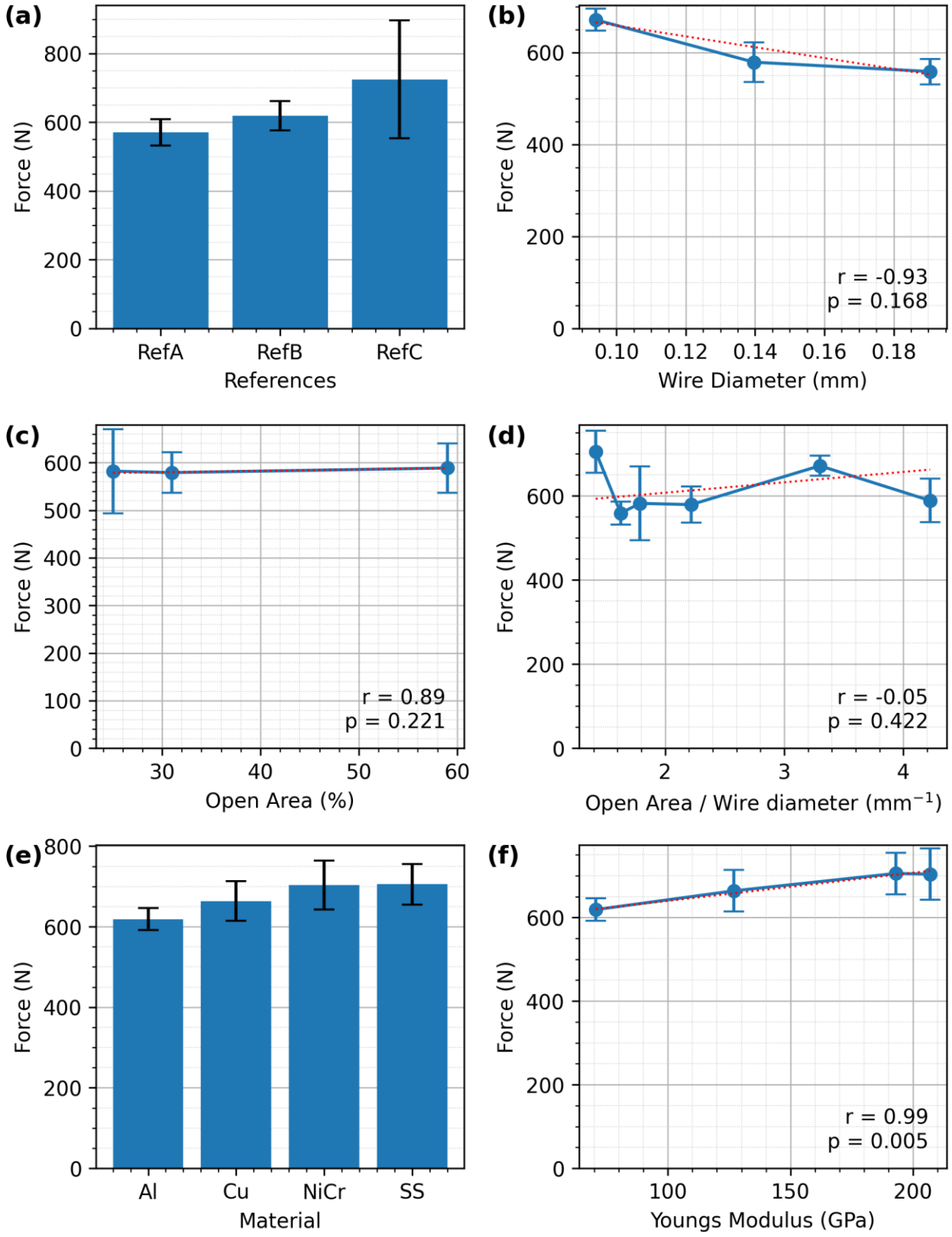

Figure 6-6 – G2C results: Force plotted vs. (a) references series, (b) wire diameter, (c) open area, (d) mesh ratio, (e) material, and (f) young's modulus

In Figure 6-6(a) the G2C experiment references are plotted. The RefA adhesive (commercial wind energy adhesive, which has additives to achieve good mechanical and thixotropic properties) has the lowest maximum force of 570 N. RefC the unmodified RIMR035 adhesive has the highest force, while the modified adhesive is in the middle. From this it can be concluded that the additives reduce the overall toughness of the bond. Though the modified adhesive still has a higher toughness than the commercial adhesive. The standard deviations for the unmodified adhesive were the highest, possibly due to the varying position of the crack initiation resulting from the different production method used for these samples.

The effect of the wire diameter on the shear strength is shown in diagram (b). The force trends downwards with increasing wire diameter. However, this is not significant with a p value of 0.168, where a p-value below 0.05 would be considered significant. In (c) the effect of open area is shown, this does not affect the strength of the bond, with the shear strength being constant.

How the ratio of open area to wire diameter affects maximum force is shown in part (d). The high standard deviations and variability in results means that no conclusion can be drawn from these. This analysis method was proposed in [DHG+12] with the claim being that a higher ratio increases the bond strength. This can neither be proven or disproven. Here the analysis showed different trends based on if weighted or unweighted analysis was performed. The weighted trend line shows an increase in maximum force with increasing ratio, while unweighted correlation is negative.

Lastly the effect of material is shown in diagram (e) and (f). There is a significant correlation between the young's modulus of the wire material to the bond strength. However, the increase in strength is minor, with a 13.7 % higher break strength for a 193 % increase in the young's modulus from the Aluminium to the stainless steel. The cause of this increase can either be explained by an increase in bond strength or a stiffening of the samples due to the higher young's modulus of the sample. To evaluate this the elasticity of the samples is also calculated based on the slope of the force vs. displacement graphs and the following formula:

$$E = \frac{L^3 m}{4 * w * t^3} \tag{4}$$

Where: L is the span length (100 mm), w is the sample width, t is the thickness and m is the slope before the onset. The relation between the sample stiffness and the wire stiffness as well as the sample stiffness and the resulting force are shown in Figure 6-7.

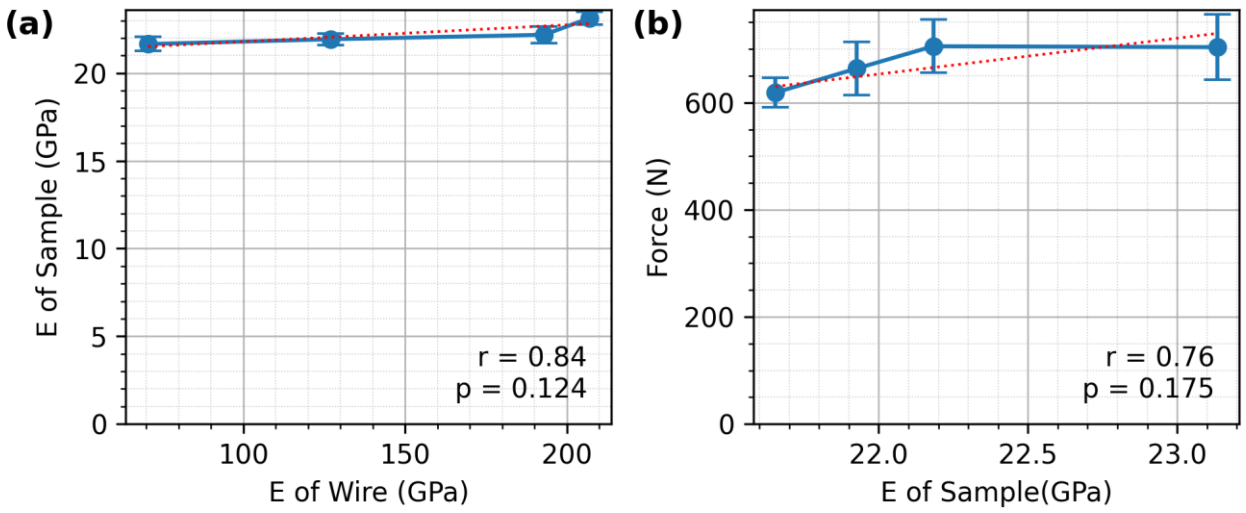

Figure 6-7 – (a) Comparison of E-moduli of wire and sample, and (b) Force vs E-moduli of samples

For both of these diagrams the correlation is not significant however a slight trend can be seen in both. As stiffer wires are used in the sample, the stiffness of the sample increases slightly. Though the expected increase is small due to the small volume fraction which the wire takes up, in addition the mesh is placed in the middle of the sample where the influence on the bending moment is small due to the small distance to the center of gravity. As the sample stiffness increases the force increases slightly. Both of these trends are weak while the observed increase in bond strength is statistically significant. Thus, it can be concluded that the young's modulus has a significant effect on the bond strength.

Microscope analysis of the sample sides was done to analyse the failure mode and crack propagation. These pictures can be seen in Figure 6-8, in the images the blue foil is placed to the left, ending near the midpoint of the image. The samples are oriented the same way they were tested, with the loading nose being to the right and moving onto the sample from the top. The round dots in these images are the labels placed onto the samples, while the green vertical line is the marking of the foil end. The perpendicularly cut wires are visible in S1 to NiCr, while the metallic parts in S1 and S3 are wires which were cut length-wise. The cracks appear as dark lines within the adhesive. There are two different ways the cracks propagated in the samples. Either the crack moved immediately to the upper adherend with a brittle failure or the adhesive failed ductile moving slowly to the upper adherend. For almost all the G2C tests the crack developed at the tip of the nonstick foil before proceed to curve upwards to the adherend. The exceptions are RefA and RefB were the crack moves up towards the top adherend before the end of the foil.

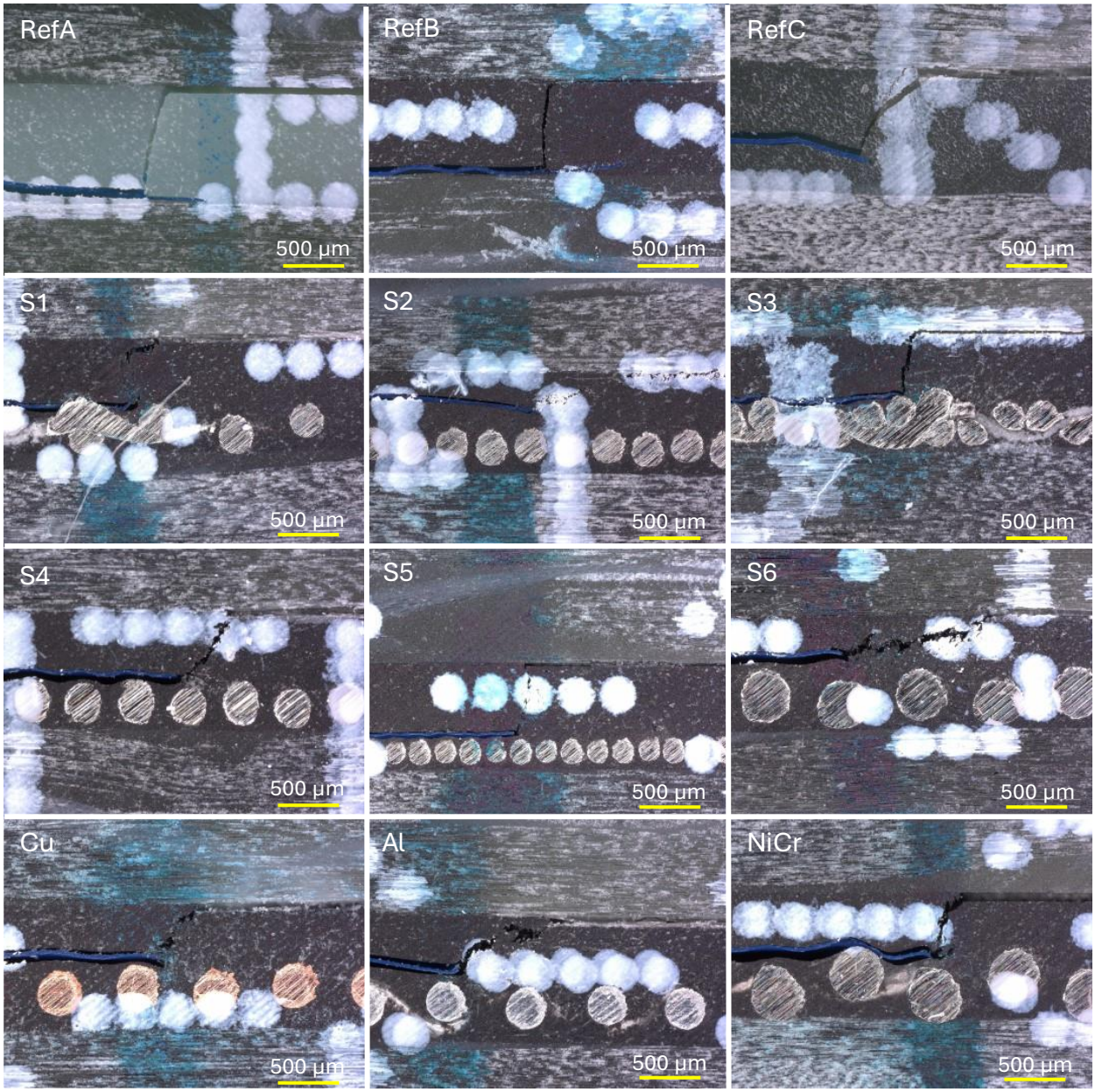

Figure 6-8 – Cross-sectional microscope analysis of G2C test at 40x magnification

Two samples of each series were taken and split apart so that the crack could be examined. The images can be seen in the Appendix 9.3 while the identified fracture patterns are shown in Table 6.1. This gives a view onto the fracture pattern and allows better failure mode determining for the G2C tests in the starting region of the crack. To determine the type of fracture the samples were held at a shallow angle so that height differences and fibers can be easily identified. In the G2C region all of the samples showed exposed fibers of the laminate material on both halves of the sample indicating a cohesive substrate failure. In the rest of the sample the splitting will induce a mode 1 failure. This allows for a rough identification of the failure mode which might be expected in the G1C tests.

In the fracture pattern under mode 1 load is applied a different failure mode emerges for many of the samples. Both of the RIMR035 reference samples had a mixed but predominantly cohesive failure where the crack moved between the two adherends. The samples with a steel mesh had predominantly adhesive failures with small cohesive parts. The exception to this is the S1 mesh which had a mixed failure pattern. The S2 samples had a substrate failure, however these were the only samples produced after issues with the GFRP material started to appear. The copper and aluminium mesh samples have an adhesive fracture pattern. In the aluminium series the second half of the fracture was an adhesive – aluminium mesh adhesion failure instead of the common adhesive – GFRP adherend adhesion failure. This indicates that aluminium has the weakest bond strength of these tested materials, and might not be suited for this application. The NiCr samples showed only substrate failure.

Table 6.1 – Fracture patterns in G2C samples for G2C and mode 1 load

Sample	Failure mode section 1 Loading mode 2	Failure mode section 2 Loading mode 1
RefA	Sub	Mix
RefB	Sub	Mix (mostly Cohesive)
RefC	Sub	Mix
S1	Sub	Mix (mostly adhesive)
S2	Sub	Sub
S3	Sub	Adh
S4	Sub	Adh
S5	Sub	Adh
S6	Sub	Adh
Cu	Sub	Adh
Al	Sub	Mix (also at mesh)
NiCr	Sub	Sub

* Adh = adhesive failure, Coh = cohesive failure, Sub = substrate failure, Mix = mix of cohesive and adhesive failure

Overall, the G2C experiments showed that the onset-point which is usually used for these experiments cannot be reliably identified, thus the analysis was carried out using the maximum force. Adhesive additives reduce bond toughness, although the modified adhesive still outperformed the commercial reference. Mesh geometry parameters such as wire diameter, open area, and open-area-to-diameter ratio showed low correlation though trends could still be determined. Open area had no effect on fracture toughness, while increased wire diameter

decreased the fracture toughness. In contrast, the wire material had a significant effect, with higher young's modulus materials generally increasing bond strength. Microscopy and fracture analysis further revealed that substrate failure was most common. In mode 2 loads failure behaviour depended strongly on the reinforcement material, with aluminium showing comparatively weak adhesion while NiCr samples consistently exhibited substrate failure, indicating superior bonding performance.

6.3 Single-Lap-Shear (SLS) Experiment

The static SLS results shown in Table 6.2 indicate an improvement in shear strength with both the modified adhesive and the addition of wire mesh over the wind energy certified adhesive. RefA has a strength of 13.2 ± 0,9 MPa while the modified adhesive (RefB) had a higher shear strength of 14.0 ± 1,0 MPa. The highest performance was obtained for the sample with the S6 wire mesh, showing that the wire mesh might have a reinforcing effect.

The RefA and RefB samples were also previously tested at the DLR in SLS experiments during the development of the modified adhesive and reached a shear strength of 12.81 ± 0.42 and 12.50 ± 0.47 MPa respectively. [Mar25] Notably, in the earlier study the modified adhesive performed slightly worse than the wind energy adhesive, whereas in the present results it outperforms RefA. This suggests that the processing conditions have changed slightly.

The large standard deviations (0.9 to 1.1 MPa) indicate a certain variability in the results. Therefore, further analysis would be required to confirm the significance of these results as the averages of the RefB and S6 lie within one standard deviations of each other.

Table 6.2 – Static SLS test results

Sample	Shear strength (MPa)	Standard deviation (MPa)
RefA	13.2	0.9
RefB	14.0	1.0
S6	14.7	1.1

Using the results from the static tests the dynamic tests were conducted using a pearl string method with tests at 80, 70, 60, 50 and 40 % of the maximum shear strength as found in the static tests. In Figure 6-9 the S-N curve calculated according to DIN 50100 is shown, with the 10, 50 and 90 % failure probability indicated.

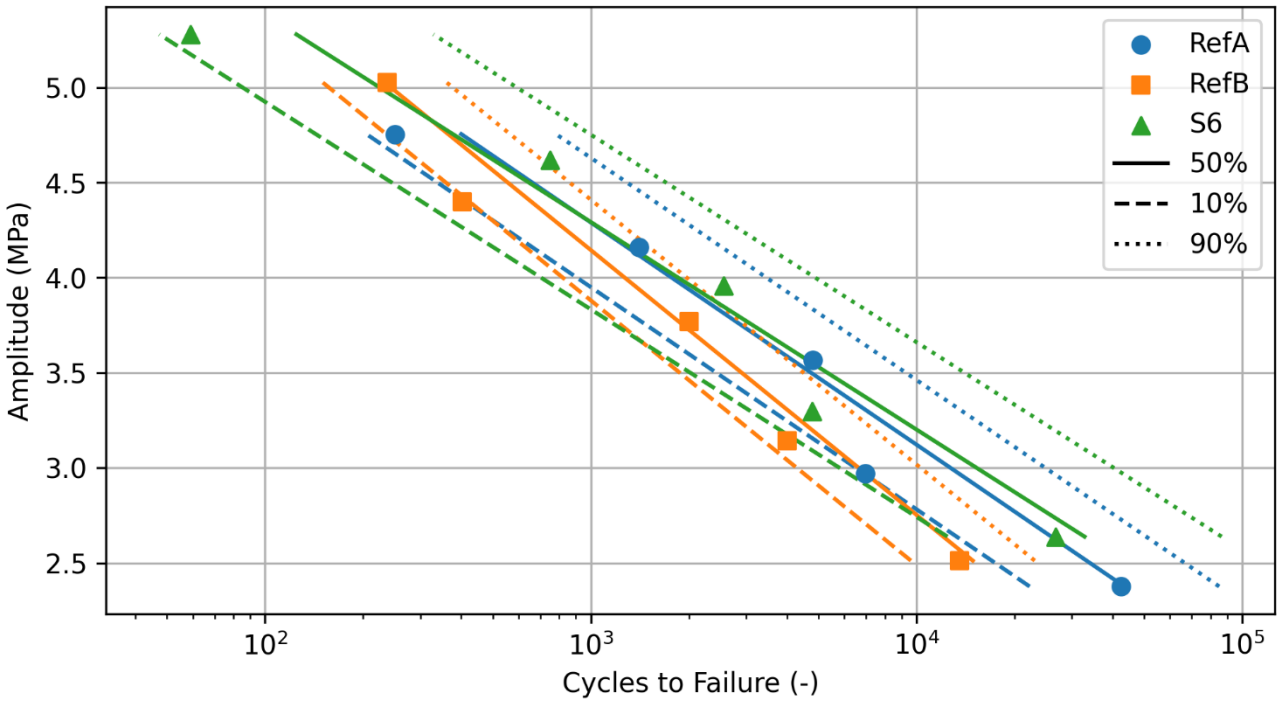

Figure 6-9 – S-N curve for dynamic SLS tests

First it is important to note that the difference between the results is not significant. The S6 samples have the highest 90 % failure load however this occurs due to the higher standard deviation in the results. The RefB samples with the modified RIMR035 adhesive have a slightly higher slope compared to the other two series leading to higher lifetimes. It must also be noted that the load decreases significantly with increased cycles to failure, in the case of these tests the maximum cycles that a sample endured is 42498 at 40 % of the static shear strength, which is low for adhesives in general.

For each of the force cycles the displacement envelope was recorded, which includes various displacements. The maximum displacement reached in each cycle can be seen in Figure 6-10 with the x-axis of cycles to failure being normalized to be able to plot all of the experiments on the same diagram. The bumps in the displacement graphs are due to the stopping of the machine to be able to take images of the sample for the crack propagation analysis. After the short stop the machine requires a short settling-in period before the previous state is reached again.

To be better able to compare the strain of the sample a normalization of these results is undertaken. The normalization is done by dividing the displacement by the displacement near the 5 % cycle to failure. This way the initial settling of the sample does not significantly affect

normalization. All results are shown in Figure 6-11 with the three series being colored differently. Separate diagrams for each sample can be found in appendix 9.5.

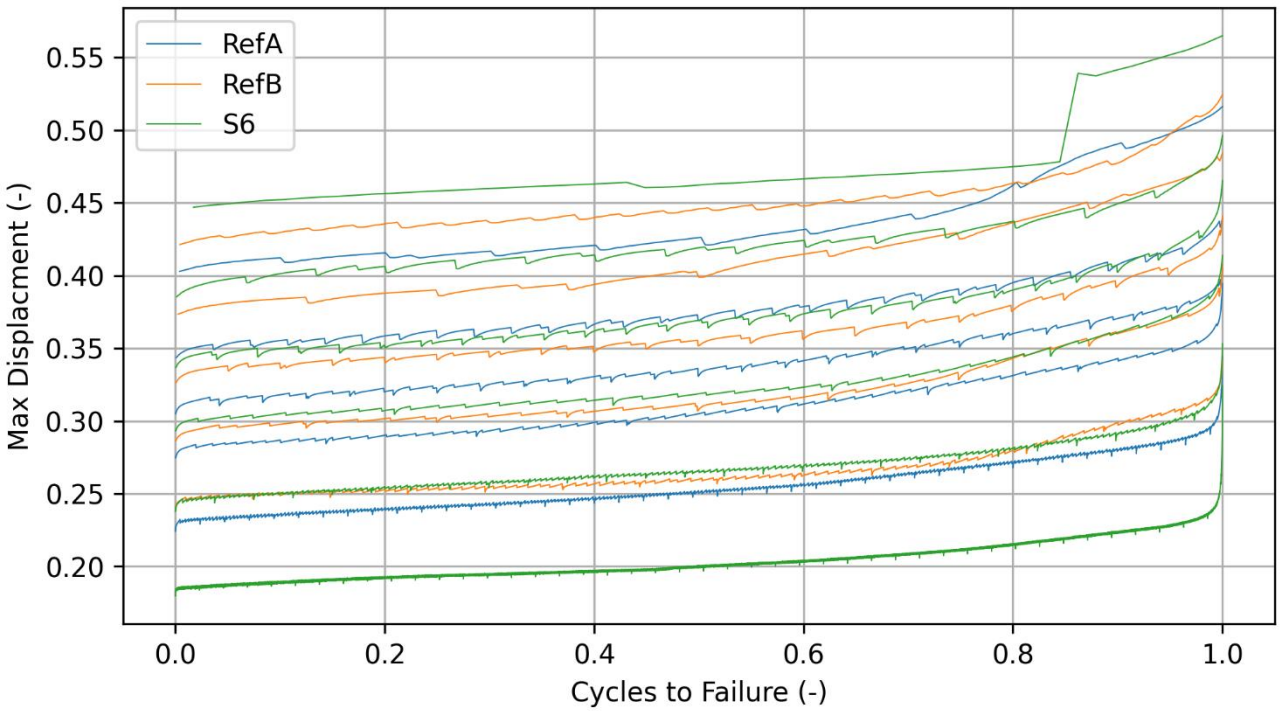

Figure 6-10 – Displacement curves for dynamic SLS tests

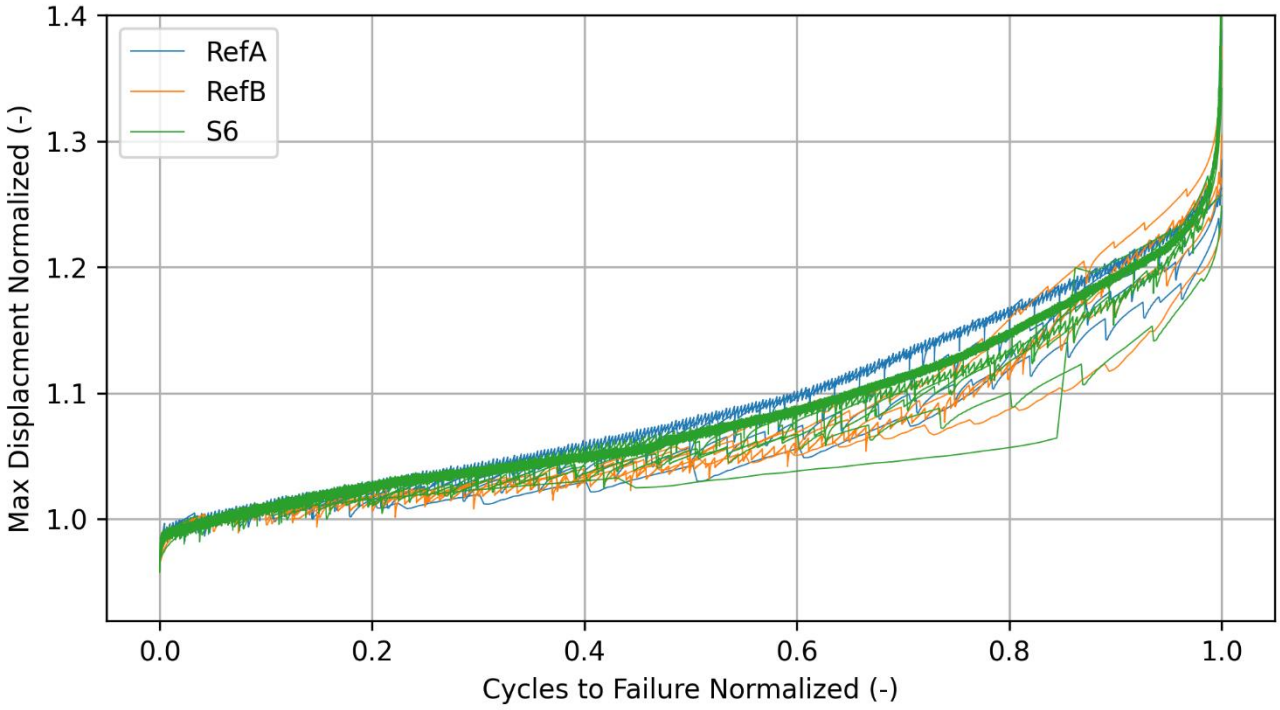

Figure 6-11 – Normalized displacement curves for dynamic SLS tests

The different experiment diagrams diverge slightly however they all follow the same general trend with an initial small increase in displacement followed by a linear region and then near the failure an increased displacement speed. The third region starts slightly earlier for higher loads.

The fracture pattern of the various samples was also examined to determine the failure mode. Sample images for each series can be seen in Figure 6-12. Both reference series had a substrate failure, while the S6 series had mainly substrate failure with occasionally small regions of adhesive failure between adhesive and mesh. This failure pattern was the same for both the dynamic and static tests.

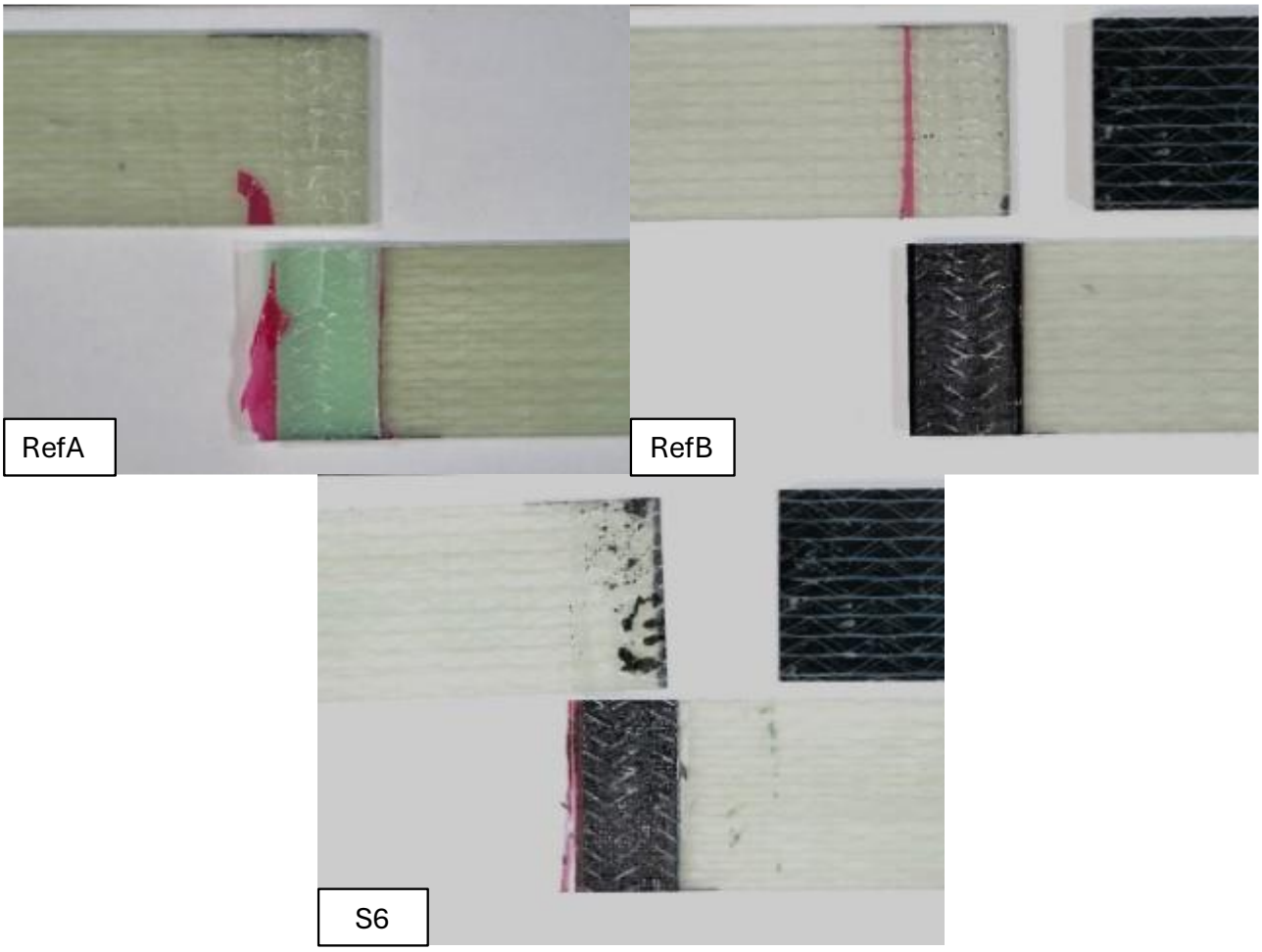

Figure 6-12 – SLS fracture patterns

Due to the small difference in the S-N curve, the displacement curves and the substrate fracture pattern it can be concluded that the laminate was the weakest link in these tests and that the adhesive only played a minor role in the observed results. Thus, the influence of the mesh cannot be determined definitively. Though the small difference in fracture pattern might indicate

that the bond between adhesive and stainless-steel mesh might be the second weakest link and thus a weak point which would need to be further investigated.

6.4 Demonstrator

The demonstrator is a proof of concept for the entire structural health monitoring setup. It is used to test the measuring equipment and show which types of adhesive damage can be detected and localised. In this section the results from the measurements on the demonstrator parts will be discussed. The goal was to identify the simulated damage using the resistance measurements using the multiplexer system provided by INVENT GmbH. Though firstly the localization and measurements were done using a multimeter to verify the viability of this method for adhesive, cohesive and mixed failure.

6.4.1 Multimeter measurements on the Demonstrator

To effectively discuss the results of the measurements the position and measurement path needs to be clearly defined. In Figure 6-13 several measurement combinations can be seen which are numbered accordingly. The contacts on each side (left, right) form opposing pairs with the adhesive layer between them. These pairs are adjacent to each other in a row. The resistance can be measured between the opposing contacts, the top two contact, either top and bottom contact or both bottom contacts. A convention for the location of the contacts on the demonstrator is introduced as in the format of x.y where x denotes the row and y the column.

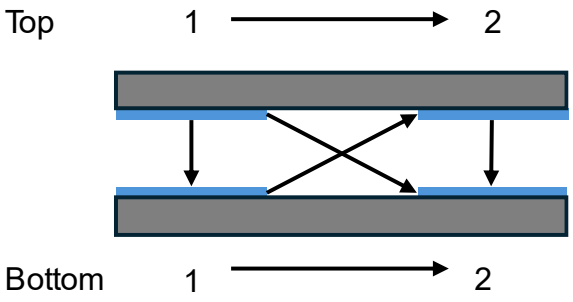

Figure 6-13 – Measurement path numbering between different contacts (not to size)

In Figure 6-14, the resistance of the adhesive is overlayed on top of a diagram of the demonstrator with the contacts shown in blue and the damage indicated in red. The measurements between the contacts are for the two adjacent contact pairs. The four data points from top to bottom correspond to the measurement paths: 2, 3, 4 and 5. As the resistance is almost two orders of magnitude higher for the measurements between adjacent contact pairs

and measurement path 1 these are shown on a different legend so that smaller differences can be seen.

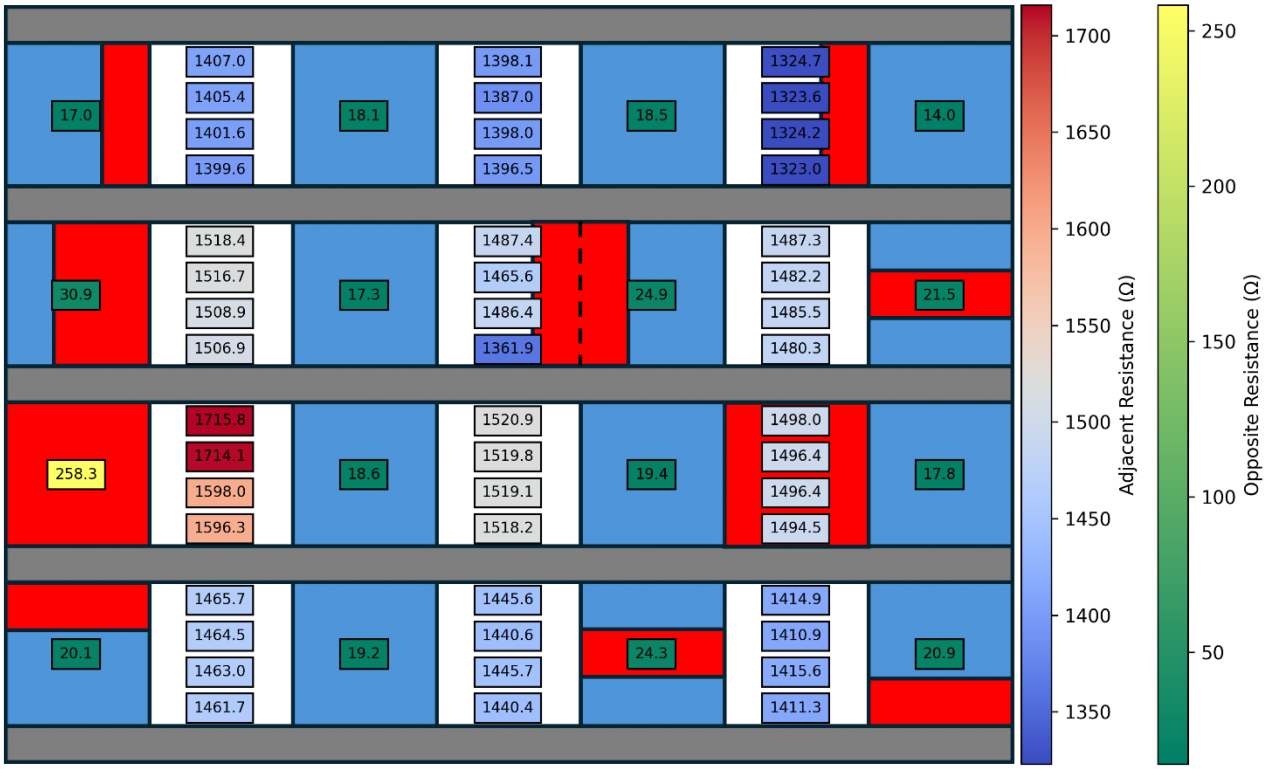

Figure 6-14 – Adhesive failure resistance measurements overlayed onto schematic of the demonstrator

The measurements for path 1 in column 2 (excluding row 4 due to different via placement) result in a reference resistance of 18.0 ± 0.5 Ω. While the adhesive between 1.2 and 1.3 as well as 3.2 and 3.3 is undamaged and can be used as a reference resistance of 1457 ± 62 Ω for the measurement between contact pairs. There is no significant difference between the resistances measured using the measuring paths 2-5. However, the resistance measured in row 1 and row 3 show a small difference of ~120 Ω.

Further analysis of the results is shown in Table 6.3, where each damage case is shown with comments on whether the damage could be detected and localized.

Table 6.3 – Analysis of various damage cases within the adhesive Demonstrator

Damage Case	Comments
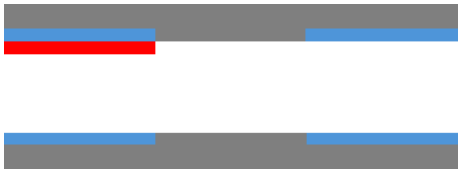	Path 1: 14 - fold increase in resistance. Good detectability The measurements which use the covered contact have higher resistance, i.e. path 2 & 4 have slightly higher resistance than path 3 & 5.
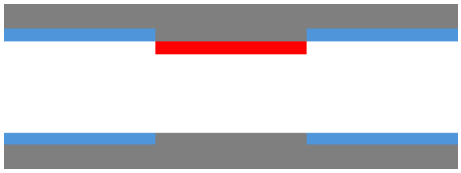	Not detectable
	67 % of contact covered 72 % higher resistance in path 1
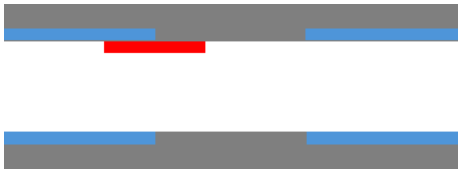	38 % increase in resistance of path 1 No increase in the other Measurement paths
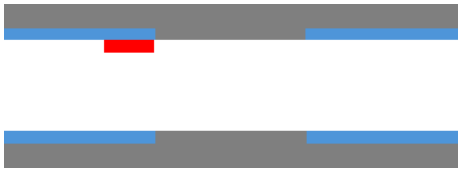	33 % of contact covered Not always detectable
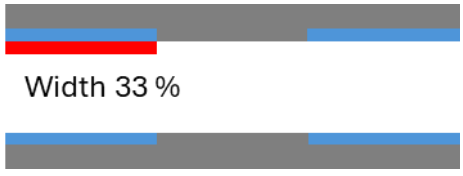	33 % of contact covered Damage is the same size as the previous damage case, but rotated 90°. An increase in resistance of 19 % is observed. In row four these have different distances between via and damage. There is no correlation between this distance and resistance, though all three damage locations have a higher resistance than the reference in measurement path 1.
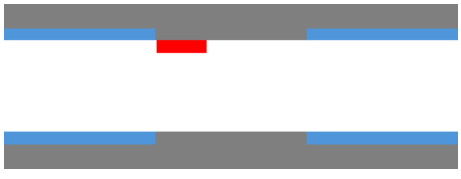	Not detectable

From the adhesion demonstrator it can be concluded that large damage is detectable and locatable when it is between opposing contacts i.e. measurement path 1, however it is difficult when the damage is small or between adjacent contacts. In addition, the no statement could be made on the effect of distance between via and damage and the resistance.

In Figure 6-15 the results for the demonstrator with cohesive damage is shown using the same method as for the adhesive demonstrator.

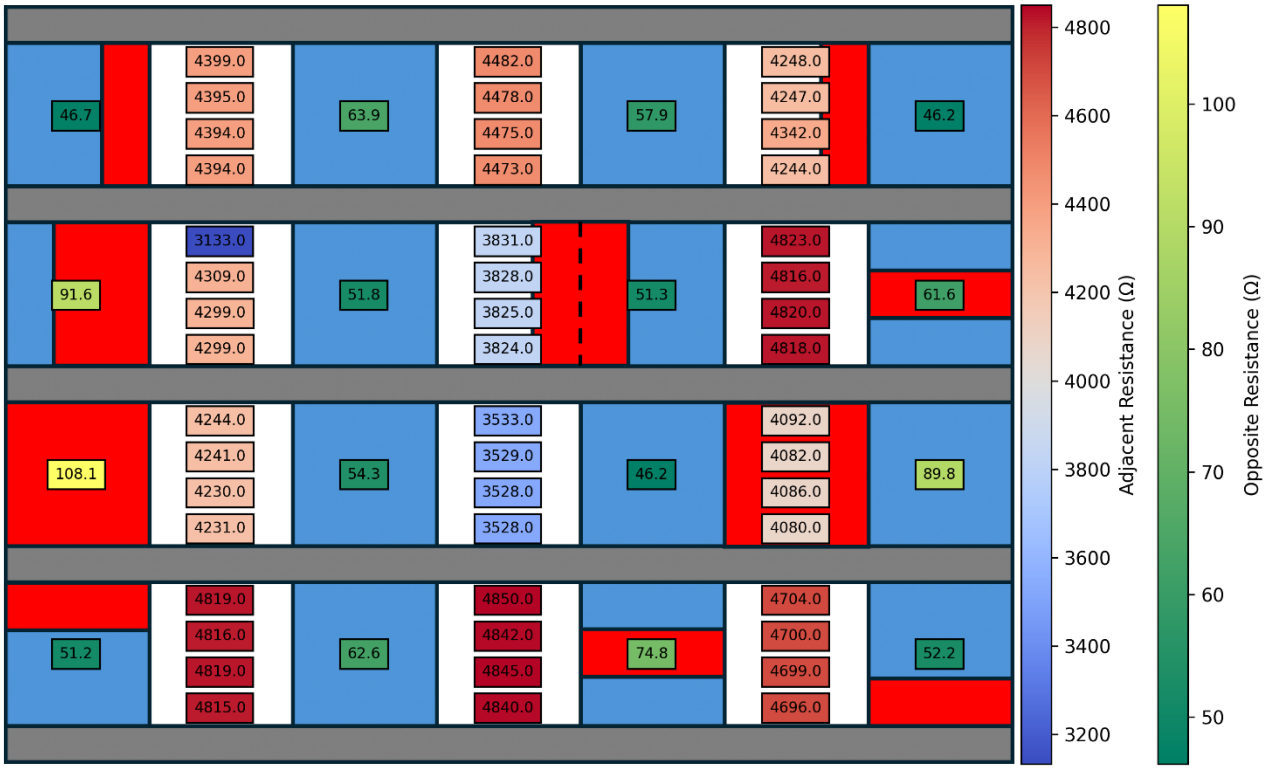

Figure 6-15 – Cohesive failure resistance measurements overlayed onto schematic of the demonstrator

The reference points are located at the same positions as in the adhesive demonstrator. The reference resistance for path 1 is 58.1 ± 5.2 Ω, while the reference resistance between contact pairs is 4003 ± 474 Ω. It is notable that the resistance of this demonstrator part is significantly higher at almost double the resistance measured in the adhesive demonstrator. It also shows a higher deviation. This could be due to the longer storage time before production of the part.

Table 6.4 - Analysis of various damage cases within the cohesive demonstrator

Damage Case	Comments
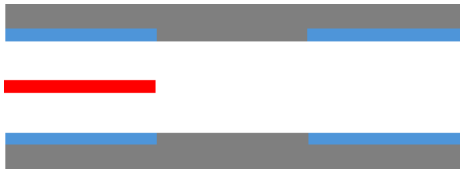	Path 1: resistance is twice the reference resistance Path 2-5: Not detectable
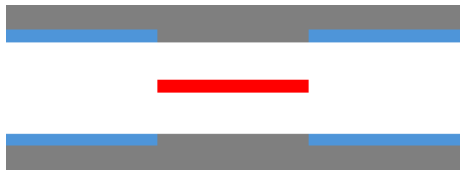	Path 1: On the right side the resistance does not increase however on the left it does, this might indicate that the foil moved during the glue-up. Path 2-5: Not detectable
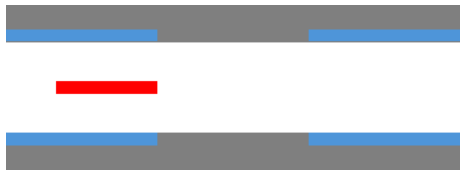	67 % of contact covered Path 1: Resistance is around 58 % higher than reference Path 2-5: Not detectable
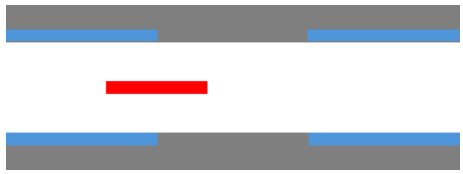	Not detectable
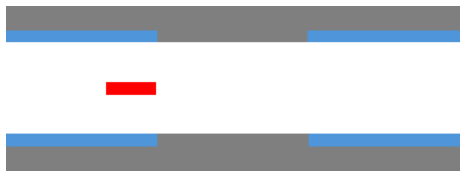	Path 1: Small reduction in resistance, which is counter to the expected results.
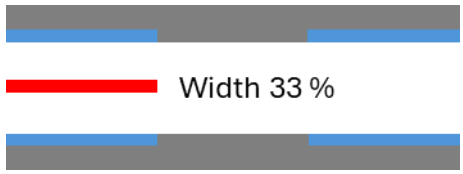	Damage is the same size as the previous damage case, but rotated 90°. No increase in resistance for path 1. For path 2-5 resistance is increased by around 20 %. In row four these have different distances between via and damage. There is no correlation between this distance and resistance.
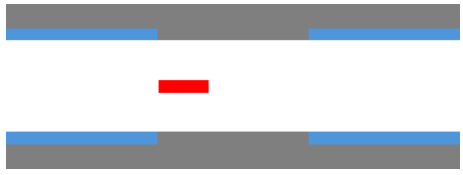	Path 1: Small reduction in resistance, which is counter to the expected results.

Again, the large damage between opposing contacts can be found, however damage between adjacent contacts is difficult to determine.

In diagram Figure 6-16 the results for the demonstrator with mixed damage is shown using the same method as for the adhesive demonstrator. The goal was to identify the influence a crack

jumping between the adherends in a mixed failure would have on the resistance, the theory being that the crack could separate the adhesive into different regions thus increasing the resistance.

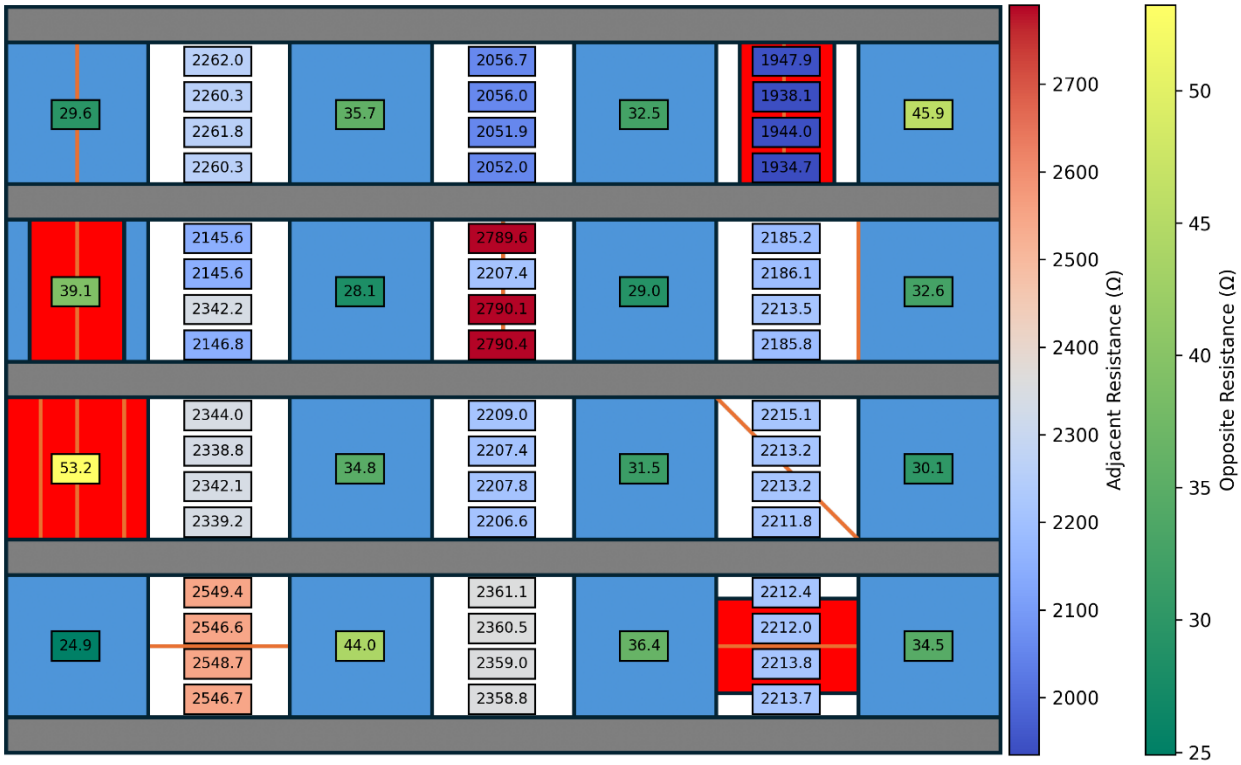

Figure 6-16 – Mixed failure resistance measurements overlayed onto schematic of the demonstrator

The reference resistances for this part were 32.9 ± 3.4 Ω for path 1 and 2131 ± 76.8 Ω for path 2-5 using the same contact points as in the adhesive and cohesive demonstrator parts, described above.

Table 6.5 - Analysis of various damage cases within the mixed demonstrator

Damage Case	Comments
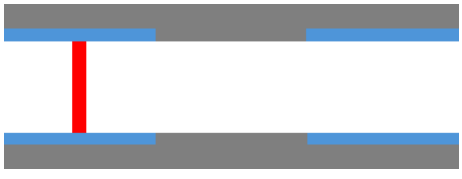	Not detectable Cross section of damage is negligible to the contact area

Damage Case	Comments
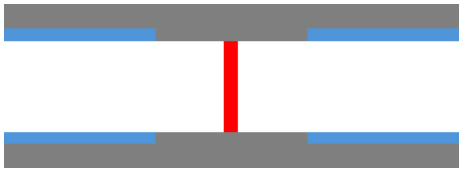	31 % increase in resistance for paths 2, 4, 5 No increase for path 3 This could be due to measurement error
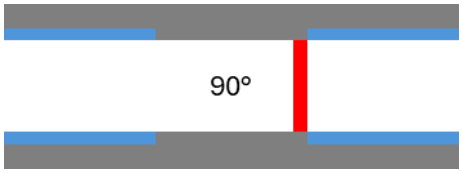	Not detectable The damage insert could have moved during clue up to the left which would make it similar to the first damage case
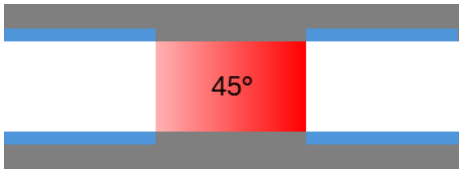	Not detectable Length of the crack is longer than the damage case above or below, which could reduce the resistance if it behaves similar to an electrical parallel connection.
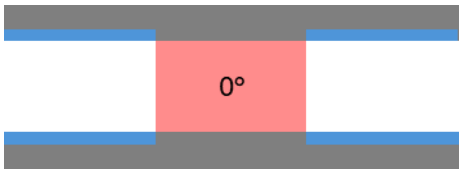	Paths 2-5 have a 19.5 % higher resistance, even though it does not separate the adhesive or take up a significant portion of the adhesive. Path 1 also has a slightly higher resistance on one side Damage is placed in parallel to the electric path
	Path 1: 19 % increase in resistance Path 2-5: not detectable
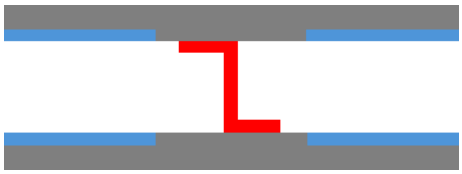	Path 1: 40 % increase in resistance on the right side no increase on the left Path 2-5: not detectable
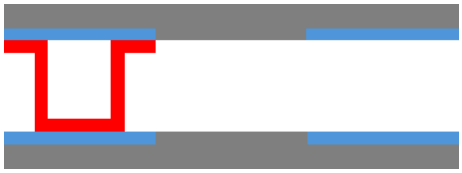	Path 1: 62 % increase in resistance Path 2-5: not detectable
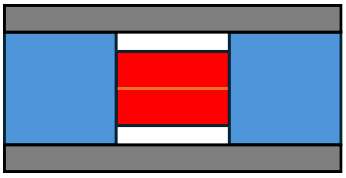	Not detectable Top-Down look onto the demonstrator instead of cross-section

As can be seen the identification and localization of small mixed failure mode damage is significantly more difficult. Compared to the adhesive and cohesive failure modes measurement paths 2-5 often do not identify the damage. The orientation of the crack is variable and effect the resistance as well. Cracks which run perpendicular to the electric paths can be detected however cracks which are parallel cannot be detected.

6.4.2 Multiplexer system for signal recording as a first step of building a SHM system

The evaluation of the multiplexer system and the measurements performed using it are discussed in this section. Each row of the demonstrator was connected to the device separately and the resistances were recorded between all 384 possible combinations of contact and reference resistors for 2 minutes. The results for three measurement paths are shown in Figure 6-17.

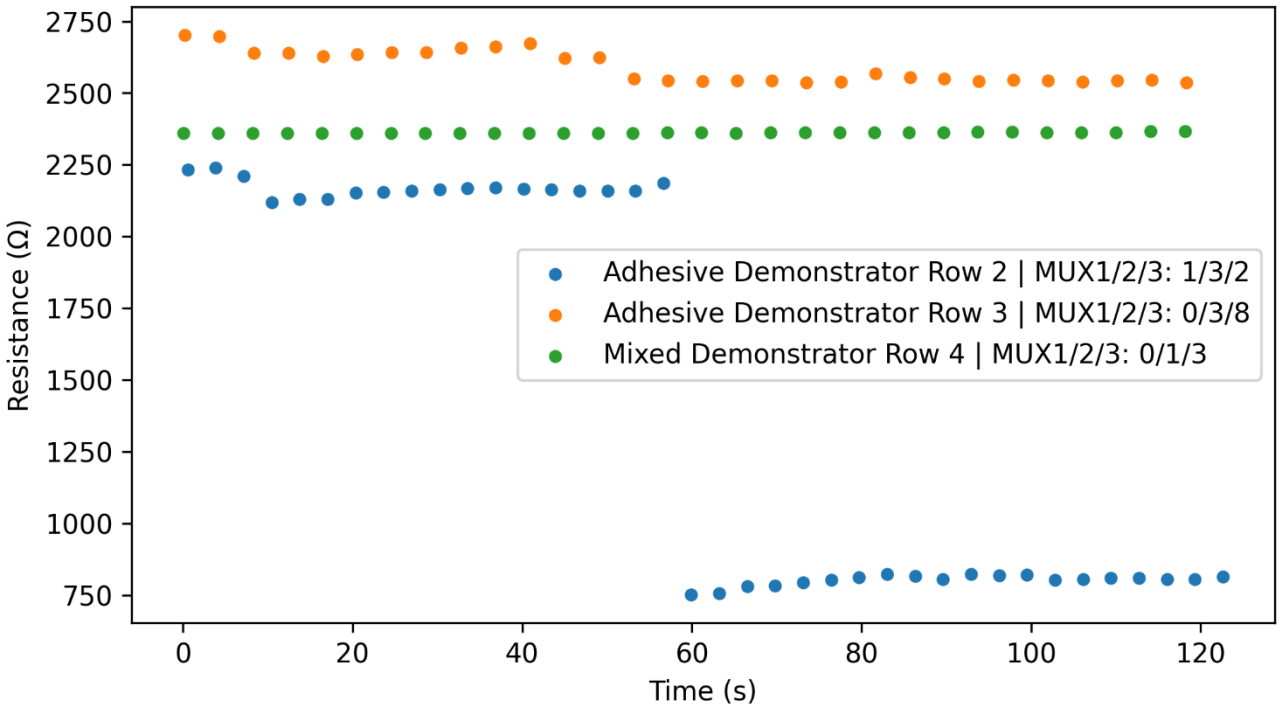

Figure 6-17 – Time vs resistance for three different measurements

The resistance for most of the different channels is steady throughout the test like the results for the mixed demonstrator row 4. However, some channels display fluctuations often with a decrease in the resistance, i.e. adhesive demonstrator row 3. Tests where this fluctuation was extreme, i.e. Adhesive demonstrator row 2, were redone while making no changes to the test setup. This often times resulting in no fluctuation in the second measurement. During the tests the demonstrator was placed on a table which was isolated during the experiment. Thus, mechanical outside influence can reasonably be excluded. However other influences from

sources such as the power supply, electromagnetic interference or warming of the demonstrator is not accounted for. The cause of the fluctuations should be further investigated as the eventual SHM system would need to work continually for many years without intervention and such fluctuations could trigger false damage alarms leading to unneeded maintenance.

Additionally, there are negative values being measured for many channels. The cause of this can be the high difference between the true resistance and the reference resistance used. These should be within the same order of magnitude however as all combinations were tested this is not always the case. A small error when measuring a point with an expected resistance ~20 Ω using a reference resistance of 10 kΩ can easily result in a measured value that is negative. Another cause for error is the reference voltage, during the tests a constant reference voltage of 5 V is assumed. Small fluctuations in the voltage can occur, due to power supply variability, small capacitors and the continually changing resistances of the measurement path (switching between measurement paths every 10 ms). An improvement to the system which could be implemented is the logging of the voltage during the testing for the resistance calculation or improving the power supply.

The multiplexer channels are connected as shown in Figure 6-18 to the demonstrator.

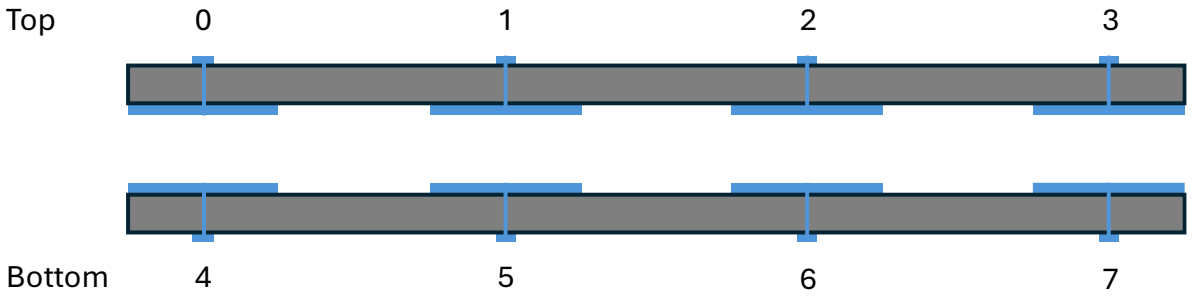

Figure 6-18 – MUX channel connection to the demonstrator

These raw results are averaged for each measurement path. These have been filtered before averaging according to the method described in section 5.6 so that only values within one order of magnitude from the reference resistance are used for the calculation. In Figure 6-19 this is shown for a representative row (row 3 of the cohesive demonstrator). While the relative standard deviation (RSD) is shown in Figure 6-20.

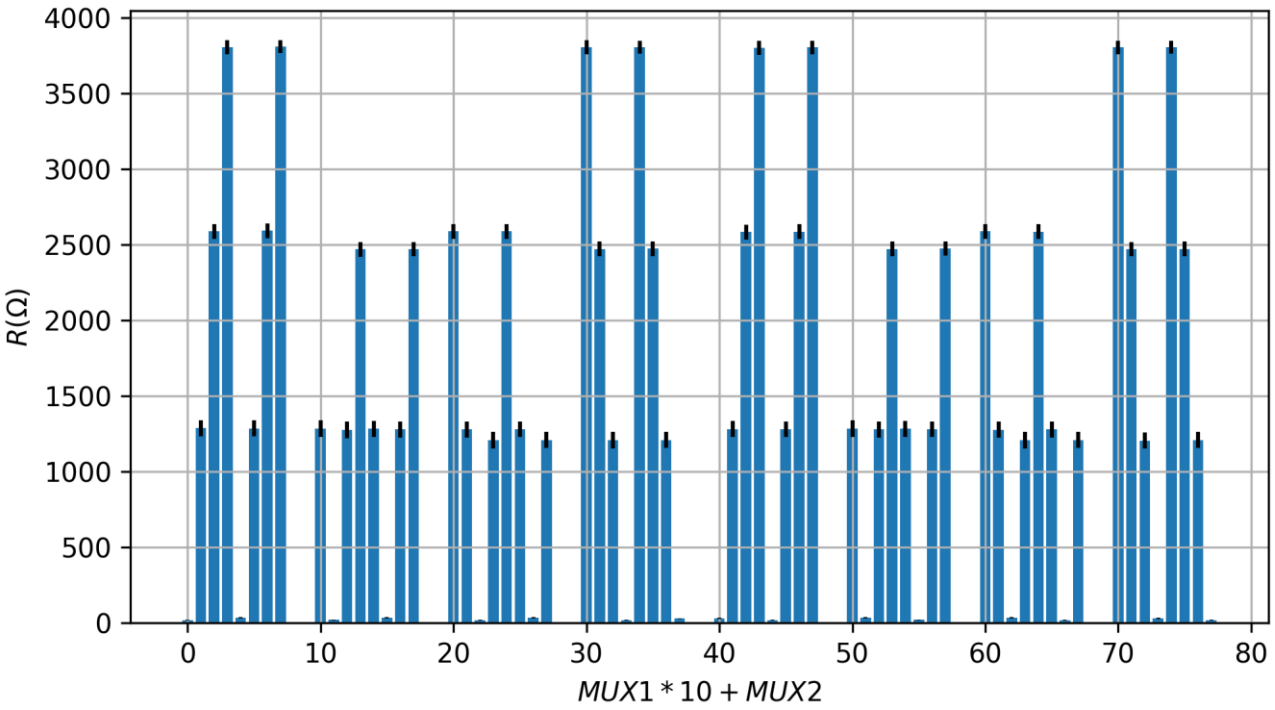

Figure 6-19 – Resistance for all measurement paths (MUX1 and MUX2 combination) of row 3 of the cohesive demonstrator

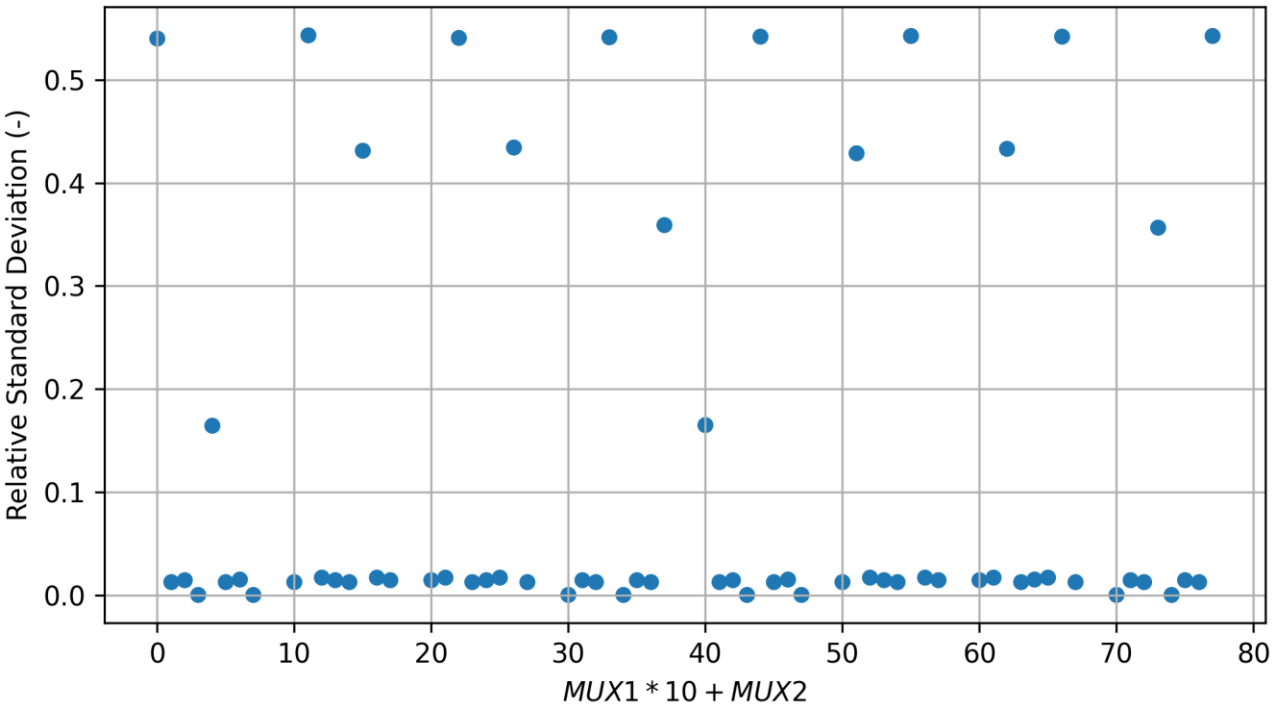

Figure 6-20 – Relative standard deviation for all measurement paths (MUX1 and MUX2 combination) of row 3 of the cohesive demonstrator

The measurements with different distances between the contacts can be easily identified by the clustering around the resistance of 0, 1250, 2500 and 3750 Ω. The standard deviation for path 1 measurements has a significantly higher and variable relative standard deviation, while all other measurement paths had standard deviations of between 44 and 55 Ω or a relative standard deviation of around 2.9 %. This shows that the measurement system is not significantly affected by the reference resistors and that there is a wide margin for choosing the resistors for measurement paths with a high resistance. Though the references should be chosen carefully when measuring path 1, and internal resistances in the device from for examples the multiplexers influence the results.

To better visualize these results heatmaps are generated were the resistance between MUX1 and MUX2 are shown. In Figure 6-21 the results for row 3 of the cohesive demonstrator is shown. This row was picked for this evaluation to have a best-case scenario for the multiplexer device as it has a large area damage which is easier to detect according to the multimeter experiments, as well as a location to determine a reference resistance for both opposite and adjacent contacts.

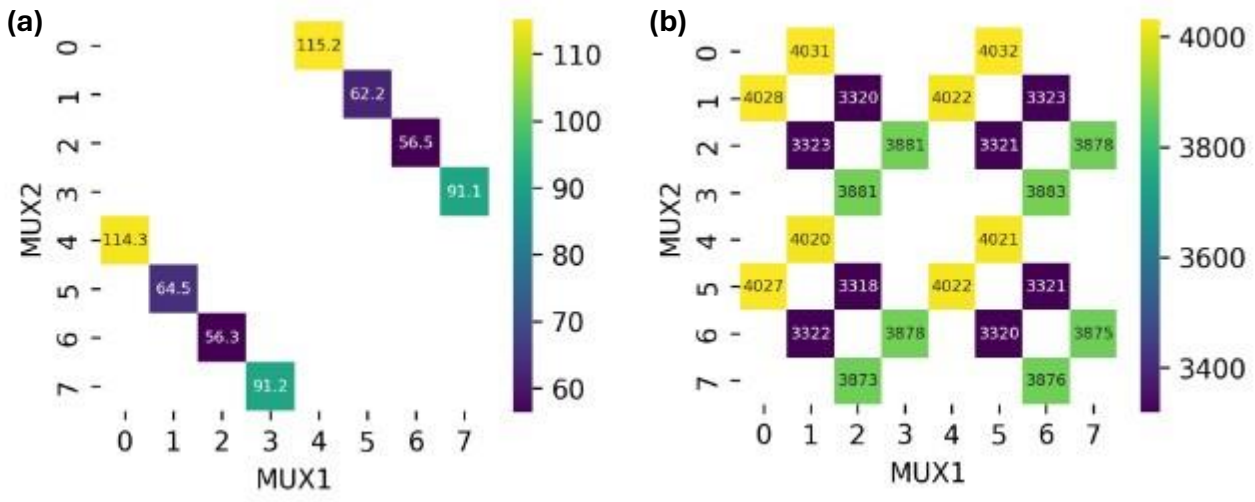

Figure 6-21 – Resistance between MUX1 and MUX2 of row 3 of the cohesive demonstrator, a) opposite contacts, b) adjacent contacts

Firstly, it can be noticed that the measurement direction through the part does not significantly affect the measured resistance, as can be seen when comparing for measurements across the diagonal, for example the measurements between 0 to 1 and 1 to 0 of MUX1 and MUX2 respectively. This shows that no diode was created in the demonstrator.

The reference resistance is calculated for path 1 to be 63 Ω and for the other paths to be 3321 Ω. The evaluation of the two different damage cases in this adhesive can be seen in Table 6.6.

Table 6.6 – Analysis of two damage cases within the cohesive demonstrator measured using the multiplexer system

Damage Case	Comments
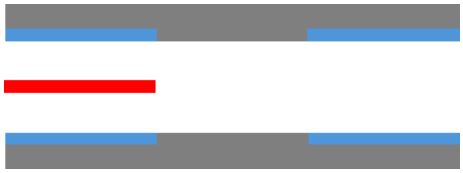	Path 1: double the reference resistance can be detected Path 2-5: slightly higher resistance
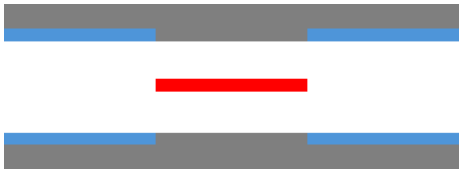	Path 1: not detected on the left, however on the right around 50 % increase in resistance Path 2-5: slightly higher resistance, not significant

Overall, the demonstrator measurements demonstrate the feasibility of using resistance-based monitoring for the detection and localization of damage within adhesive joints, as well as demonstrate the potential of a SHM system. The multimeter investigations showed that large damage can be reliably detected when the damage interrupts the direct electrical path between opposing contacts (measurement path 1). Smaller defects and cracks oriented parallel to the electrical path proved difficult to identify. Measurements between adjacent contacts generally showed lower sensitivity and were often not detected. The multiplexer-based system successfully acquired a large number of resistance measurements; however signal fluctuations, sensitivity to reference resistor selection, and measurement noise highlighted the need for further optimization of the power supply stability, and internal resistance before measurement path 1 can be used reliably. Nevertheless, large damage could still be detected successfully using the current setup.

7 Conclusion

This study investigated the influence of embedded metallic wire meshes on the mechanical behaviour of adhesive bonds and damage detection in an adhesive bond layer using resistance measurements. The work focused on two main objectives: evaluating the effect of conductive contact systems on the mechanical performance of bonded joints and assessing the feasibility of detecting and localizing different damage modes within adhesive layers.

First, the sensitivity of the previously developed conductive adhesive was investigated for different adhesive layer thicknesses. An inverse relationship between adhesive thickness and measurement sensitivity was identified. Using this the thickness for the demonstrators was chosen.

To evaluate the influence of embedded meshes on bond performance, fracture toughness experiments were conducted using G2C fracture toughness tests. Due to difficulties in determining a consistent crack onset point, the evaluation was based primarily on the maximum force reached during testing. Within the investigated geometry range, the mesh open area showed no measurable influence on bond strength. In contrast, larger wire diameters tended to reduce the maximum load-bearing capability of the bond, although the statistical significance of this trend remains limited because of the high deviations in the measurements. Literature recommendations suggesting that the ratio between open area and wire diameter influences joint strength could neither be confirmed nor rejected conclusively.

The influence of wire material was investigated using meshes with different young’s moduli. A significant increase in bond strength was observed for stiffer wire materials. To identify the underlying mechanism, the stiffness of the bonded specimens was analysed. Although samples containing stiffer meshes also exhibited higher overall stiffness, this could be rules out as the cause. Consequently, it was concluded that the young’s moduli of the mesh, rather than a global stiffening effect of the specimen, is likely responsible for the increased bond strength.

Analysis of the fracture surfaces revealed distinct failure characteristics depending on the loading mode and mesh material. In the mode II load region, all specimens exhibited cohesive substrate failure. Under mode I dominated loading conditions, adhesive failure became predominant, with two notable exceptions. Aluminium meshes showed adhesion failure between the mesh and adhesive, indicating insufficient interfacial bonding and the need for additional surface treatment before aluminium can be considered a viable contact material. In contrast, the nickel-chromium mesh specimens displayed exclusively cohesive substrate failure, suggesting a strengthening of the adhesive layer.

Fatigue behaviour was investigated through single-lap-shear (SLS) tests performed on two references without embedded mesh and one with embedded meshes. No significant differences in the S–N curves or displacement envelopes were identified between the investigated series. All specimens showed predominantly cohesive substrate failure. Overall, the results suggest that the adherend material governed failure in the present experiments and that the adhesive layer itself only played a secondary role. Consequently, future investigations should employ stronger adherend materials and a broader range of mesh geometries to better isolate the influence of the conductive meshes on fatigue performance. Although in several samples, partial failure occurred along the stainless-steel mesh interface, indicating that the mesh may locally act as a weak point within the bond.

The detectability and localization of damage were evaluated using three demonstrator parts representing adhesion, cohesion, and mixed failure modes. Initial measurements performed using a multimeter demonstrated that large damage located between opposite contacts could be reliably detected and approximately localized in all demonstrators. However, smaller defects and damage located between adjacent contacts proved more difficult to identify. The distance between the measurement location and the damage did not show a significant influence on detectability. Measurements on the cohesion and mixed-failure demonstrators exhibited higher variability, especially between adjacent contacts, making reliable localization more challenging.

Subsequently, the demonstrators were investigated using a dedicated multiplexer system which could be further developed into a SHM system with varying reference resistances. The experiments highlighted that the internal resistance introduces higher variability for shorter electric paths. The reference resistance should ideally be determined individually for the undamaged structure prior to operation to account for voids or other imperfections in the part. In addition, fluctuations in the supplied voltage were found to influence the calculated resistance values and should therefore be monitored and compensated for in future systems. Despite these limitations, the system was able to reproduce the key result obtained with the multimeter measurements: large damage between opposite contacts could be reliably detected.

The results of this work demonstrate the potential of both the embedded mesh and multiplexer system. At the same time, several challenges remain unresolved before such systems can be applied in practical wind turbine or aerospace structures. Important open questions concern the optimal electrode spacing for balancing sensitivity, localization capability and cost/complexity, the most suitable electrode configurations for random damage scenarios, the minimum detectable damage size, and the influence of mesh geometry and contact arrangement on both

mechanical and electrical performance. Environmental effects such as moisture absorption and temperature variations must also be investigated, particularly because wind turbine blades are exposed to humid operating conditions that may alter the electrical properties of the adhesive and potentially lead to short-circuiting effects through condensation.

From a mechanical perspective, additional research is required to determine the relationship between mesh geometry and bond strength with greater certainty. Future work should therefore investigate a wider range of wire diameters, open areas, and mesh architectures and ideally use strong adherend material. Should the G2C tests be redone it is advised to start with the G1C tests to gain a more complete picture on failure patterns under varying loading modes. Dynamic testing needs to further investigated as the results of this study are not useful in this regard, for example the most promising mesh material, copper due to its high electrical conductivity, was not tested in the SLS tests. Notch testing with varying notch radii could provide further insight into whether the reduction in bond strength observed for larger wire diameters is related with classical notch effects, as the observed effects do not support this currently. Complementary finite element simulations of wire–adhesive systems under different loading conditions may additionally help identify the dominant stress concentrations and failure mechanisms governing the observed behaviour.

Regarding SHM implementation, future investigations should focus further developing the system. The individual parts of the measuring system have been studied; however, the combination of multiplexer system and metal mesh has not been tested. In this regard a solution for the connection between adhesive mesh and measurement device must be found. Local electronics and multiplexing concepts could reduce the number of required wires and simplify integration into large structures. Redundancy within the sensor network should also be considered, as the failure of a single contact currently limits the ability to monitor the associated region. In the long term, prepregs with integrated sensor networks and contact interfaces may represent an attractive industrial solution for large-scale manufacturing and repair applications.

An additional benefit which could be realised is the integration of SHM functionality into existing lightning strike protection systems. Since these systems already employ conductive meshes embedded within composite laminates, they could potentially serve a dual purpose by simultaneously providing lightning protection and structural health monitoring capabilities. Furthermore, alternative measurement methods such as impedance or capacitance-based approaches using inductive driver and pickup coils may eliminate the need for direct electrical contacts altogether. Such concepts have already shown promising results in electrically

conductive glass fibre reinforced polymers and may also prove applicable to conductive adhesive systems in future developments.

8 Bibliography

[AGR+13] Arronche, L.; Gordon, K.; Ryu, D.; La Saponara, V.; Cheng, L., Investigation of galvanic corrosion between AISI 1018 carbon steel and CFRPs modified with multi-walled carbon nanotubes,
Journal of Materials Science 48 (2013), H. 3, S. 1315-1323.

[BAG+20] Bregar, T.; An, D.; Gharavian, S.; Burda, M.; Durazo-Cardenas, I.; Thakur, V.K.; Ayre, D.; Słoma, M.; Hardiman, M.; McCarthy, C.; Yazdani Nezhad, H., Carbon nanotube embedded adhesives for real-time monitoring of adhesion failure in high performance adhesively bonded joints,
Scientific reports 10 (2020), H. 1, S. 16833.

[CBL+24] Cao, D.; Bouzolin, D.; Lu, H.; Griffith, D.T., Enhanced joining strength in additive-manufactured polylactic-acid structures fused by embedded heated metallic meshes,
Journal of Manufacturing Processes 121 (2024), S. 100-120.

[CBN+21] Cavalcanti, W.L.; Brune, K.; Noeske, M.; Tserpes, K.; Ostachowicz, W.; Schlag, M. [Hrsg.]:
Adhesive bonding of aircraft composite structures. Non-destructive testing and quality assurance concepts, Springer, Cham 2021.

[CCM22] Cusati, V.; Corcione, S.; Memmolo, V., Potential Benefit of Structural Health Monitoring System on Civil Jet Aircraft,
Sensors 22 (2022), H. 19, S. 7316.

[CG13] Chapetti, M.D.; Guerrero, A.O., Estimation of Notch Sensitivity and Size Effect on Fatigue Resistance,
Procedia Engineering 66 (2013), S. 323-333.

[DCC+21] Ding, J.; Cheng, L.; Chen, X.; Chen, C.; Liu, K., A review on ultra-high cycle fatigue of CFRP,
Composite Structures 256 (2021), S. 113058.

[DHG+12] Dubé, M.; Hubert, P.; Gallet, J.N.; Stavrov, D.; Bersee, H.E.N.; Yousefpour, A., Metal mesh heating element size effect in resistance welding of thermoplastic composites,
Journal of Composite Materials 46 (2012), H. 8, S. 911-919.

[DIN95] DIN EN ISO 10365, Stand: 1995-08, Bezeichnung der wichtigsten Bruchbilder.

[Doo18] Doobe, M.:
Kunststoffe erfolgreich kleben, Springer Fachmedien Wiesbaden, Wiesbaden 2018.

[DZJ+20] Du, Y.; Zhou, S.; Jing, X.; Peng, Y.; Wu, H.; Kwok, N., Damage detection techniques for wind turbine blades: A review,
Mechanical Systems and Signal Processing 141 (2020), S. 106445.

[FSA+26] Fulghum, N.; Suarez, W.; Altieri, K.; Rangelova, K., Global Electricity Review 2026. Solar surge halts fossil generation rise as clean power meets all demand growth and renewables overtake coal. 2026.

[GH19] Gedde, U.W.; Hedenqvist, M.S.:
Fundamental Polymer Science,
Springer eBook Collection, 2nd ed. 2019, Springer International Publishing; Imprint Springer, Cham 2019.

[Hab09] Habenicht, G.:
Kleben, Springer Berlin Heidelberg, Berlin, Heidelberg 2009.

[Hab16] Habenicht, G.:
Kleben - erfolgreich und fehlerfrei, Springer Fachmedien Wiesbaden, Wiesbaden 2016.

[Hau16] Hau, E.:
Windkraftanlagen. Grundlagen, Technik, Einsatz, Wirtschaftlichkeit, 6. Auflage, Springer Vieweg, Berlin 2016.

[IAL12] Ireland, R.; Arronche, L.; La Saponara, V., Electrochemical investigation of galvanic corrosion between aluminum 7075 and glass fiber/epoxy composites modified with carbon nanotubes,
Composites Part B: Engineering 43 (2012), H. 2, S. 183-194.

[Kin87] Kinloch, A.J.:
Adhesion and Adhesives, Springer Netherlands, Dordrecht 1987.

[KPN21] Katsaprakakis, D.A.; Papadakis, N.; Ntintakis, I., A Comprehensive Analysis of Wind Turbine Blade Damage,
Energies 14 (2021), H. 18, S. 5974.

[Kup01] Kupke, M.:
Entwicklung elektrisch leitfähiger Glasfaserverbundwerkstoffe mittels Kohlenstoff-Nanopartikel, 1. Aufl., Cuvillier, Göttingen 2001. Zugl.: Hamburg-Harburg, Techn. Univ., Arbeitsbereich Kunststoffe und Verbundwerkstoffe, Diss., 2001.

[KVD+11] Kühn, P.; Vinzenz Dennis Brune; Doron Callies; Stefan Faulstich; Gerd Füller; Sandra Abril Lopez; Philipp Lyding; Renate Rothkegel, Wind Energy Report Germany 2010. 2011, Kassel Germany.

[KZM08] Kaufmann, M.; Zenkert, D.; Mattei, C., Cost optimization of composite aircraft structures including variable laminate qualities,
Composites Science and Technology 68 (2008), H. 13, S. 2748-2754.

[Lei23] Leishman, J.G.:
Introduction to aerospace flight vehicles, Embry-Riddle Aeronautical University, Daytona Beach, Florida 2023.

[LFH+09] Lyding, L.; Faulstich, S.; Hahn, B.; Callies, D., Offshore~WMEP – Monitoring offshore wind energy use. 2009.

[LST+18] Li, X.; Sun, J.; Tao, N.; Feng, L.; Shen, J.; He, Y.; Zhang, C.; Zhao, Y., An Effective Method to Inspect Adhesive Quality of Wind Turbine Blades Using Transmission Thermography,
Journal of Nondestructive Evaluation 37 (2018), H. 2.

[Mar25] Markus, M., Funktionalisierung von Klebstoffharzen durch Matrixadditive für sensorische Anwendungen in Windrotorblättern. 03.03.2025.

[MB13] Moller; Björn P.:
Herstellung, Charakterisierung und Weiterverarbeitung von Carbon Nanotube Dispersionen, Südwestdeutscher Verlag für Hochschulschriften, Saarbrücken 2013.

[MET] METALCOR GmbH, Datenblatt: 2.4851 Alloy 601. https://www.metalcor.de/datenblatt/110/ .

[MIM+24] Matsunaga, W.; Imai, S.; Mizutani, Y.; Todoroki, A., Measurement of through-thickness electrical properties of carbon fiber reinforced thermoplastics using transmission method based on electromagnetic induction testing,
NDT & E International 147 (2024), S. 103202.

[MS20] Mlikota, M.; Schmauder, S., A Newly Discovered Relation between the Critical Resolved Shear Stress and the Fatigue Endurance Limit for Metallic Materials, Metals 10 (2020), H. 6, S. 803.

[MT06] MATSUZAKI, R.; Todoroki, A., Wireless detection of internal delamination cracks in CFRP laminates using oscillating frequency changes, Composites Science and Technology 66 (2006), H. 3-4, S. 407-416.

[Mül15] Müller, C.: Zur statistischen Auswertung experimenteller Wöhlerlinien 2015.

[NPR22] Naik, R.K.; Panda, S.K.; Racherla, V., Failure analysis of metal-polymer-metal sandwich panels with wire mesh interlayers: Finite element modeling and experimental validation, Composite Structures 280 (2022), S. 114813.

[OAS11] Oliva-Avilés, A.I.; Avilés, F.; Sosa, V., Electrical and piezoresistive properties of multi-walled carbon nanotube/polymer composite films aligned by an electric field, Carbon 49 (2011), H. 9, S. 2989-2997.

[Pal93] Palmer, R., Techno-economic requirements for composite aircraft components, NASA. Langley Research Center, FIBER-TEX 1992: The Sixth Conference on Advanced Engineering Fibers and Textile Structures for Composites (1993).

[PFV+25] Pinello, L.; Fernández Sánchez-Romate, X.X.; Vescovini, A.; Cinquemani, S.; Scaccabarozzi, D.; Libonati, F.; Suárez, A.J.; Ureña, A.; Sbarufatti, C., In-situ monitoring of impact dynamics, indentation, and compression after impact (CAI) on CNT-doped GFRP panels by means of electrical monitoring, Structural Health Monitoring (2025).

[PYG+22] Pawlik, M.; Yu Cheah, L.Y.; Gunputh, U.; Le, H.; Wood, P.; Lu, Y., Surface engineering of carbon fibre/epoxy composites with woven steel mesh for adhesion strength enhancement, International Journal of Adhesion and Adhesives 114 (2022), S. 103105.

[Ras12] Rasche, M.: Handbuch Klebtechnik, Hanser, München, Wien 2012.

[RLD20] Rohart, V.; Laberge Lebel, L.; Dubé, M., Improved adhesion between stainless steel heating element and PPS polymer in resistance welding of thermoplastic

composites,
Composites Part B: Engineering 188 (2020), S. 107876.

[RSN21] Rocha, H.; Semprimoschnig, C.; Nunes, J.P., Sensors for process and structural health monitoring of aerospace composites: A review,
Engineering Structures 237 (2021).

[SAE16] SAE Aerospace & Defense™ Technology, Simulating Thermal Expansion in Composites with Expanded Metal Foil for Lightning Protection. 2016.

[Sak09] Sakai, T., Review and Prospects for Current Studies on Very High Cycle Fatigue of Metallic Materials for Machine Structural Use,
Journal of Solid Mechanics and Materials Engineering 3 (2009), H. 3, S. 425-439.

[Sch09] Schijve, J.:
Fatigue of Structures and Materials, Springer Netherlands, Dordrecht 2009.

[SF13] Stephan Andreas; Frömmel:
Untersuchungen zum mechanischen Verhalten von Klebverbindungen unter Berücksichtigung von Grenzflächendefekten, Universitätsbibliothek der Universität der Bundeswehr München, Neubiberg 2013.

[SJD+04] Sørensen, B.F.; Jørgensen, E.; Debel, C.P.; Jensen, F.M.; Jensen, H.M.; Jacobsen, T.K.; Halling, K., Improved design of large wind turbine blade of fibre composites based on studies of scale effects (phase 1) - summary report. 2004, Roskilde.

[SL99] Seo, D.-C.; Lee, J.-J., Damage detection of CFRP laminates using electrical resistance measurement and neural network,
Composite Structures 47 (1999), H. 1-4, S. 525-530.

[SN25] Scarselli, G.; Nicassio, F., Machine Learning for Structural Health Monitoring of Aerospace Structures: A Review,
Sensors 25 (2025), H. 19, S. 6136.

[SR05] Sheth, N.A.; Roach, D.P., Composite Structure Utilization - Commercial Airplanes. 03.10.2005.

[SS94] Sahini, M.; Sahimi, M.:
Applications Of Percolation Theory, CRC Press, London 1994.

[SSH87] Sims, C.T.; Stoloff, N.S.; Hagel, W.C.:
[High-temperature materials for aerospace and industrial power],
Superalloys / ed. by Chester T. Sims 2, Wiley, New York, NY 1987.

[Sur04] Suresh, S.:
Fatigue of materials, 2. ed., reprint, Cambridge Univ. Pr, Cambridge 2004.

[Thu20] Thumann, P. [Hrsg.]:
Laserbasierte Klebflächenvorbereitung für CFK Strukturbauteile,
Light Engineering für die Praxis, Springer Berlin Heidelberg, Berlin, Heidelberg 2020.

[Thya] Thyssenkrupp, Stainless-steel-1.4301-304. https://www.thyssenkrupp-materials.co.uk/stainless-steel-304-14301.html .

[Thyb] Thyssenkrupp, Werkstoffdatenblatt Aluminiumlegierung. https://datenblaetter.thyssenkrupp.ch/en_aw_5754_0717.pdf .

[Thyc] Thyssenkrupp, Werkstoffdatenblatt ReinKupfer. https://datenblaetter.thyssenkrupp.ch/kupfer_CW008A.pdf .

[TTS01] Todoroki, A.; TANAKA, Y.; SHIMAMURA, Y., Composite Materials. Electric Resistance Change Method for Identification of Embedded Delamination of CFRP Plates,
Journal of the Society of Materials Science, Japan 50 (2001), H. 5, S. 495-501.

[TTS05] Todoroki, A.; Tanaka, M.; Shimamura, Y., Electrical resistance change method for monitoring delaminations of CFRP laminates: effect of spacing between electrodes,
Composites Science and Technology 65 (2005), H. 1, S. 37-46.

[Wor26] World Wind Energy Association, WWEA Annual Report 2025. 2026.

[Zel23] Zellmann, A., Herstellung und Charakterisierung von funktionalisierten Klebstoffen zur Schadensüberwachung an Rotorblättern von Windenergieanlagen. 04.09.2023.

9 Appendix

9.1 Speed Mixer

Procedure:

1. Day before mixing take out resin or hardener out of freezer
2. Start the vacuum pump. If it is struggling to start allow some air into the hoses so it doesn't have to struggle against the pressure. Let it run for 30 minutes before using.
3. Check if the Speed Mixer is dirty and if the sealing rings (O-ring) are in working condition
4. Fill the two components into the containers using a scale, such that as little material touches the sides as possible.
5. Seal the container using tape around the lid and once or twice for large containers around the height. Puncture a hole into the top of the Container to let out air during the mixing.
6. Place the container into the correct adapter
7. Check the weight of the Container and adapter combination if it is between 250g and 700g and place in the speed mixer closing lid and vacuum lid.
8. Select or make a new program on the speed mixer.
9. Open the needle valve on the Speed mixer it should get down to around 3 millibar.
10. Start the Speed mixer
11. During operation check that it doesn't vibrate excessively should it do so adjust the rpm up or down. Should that not help stop the machine. If the problem stays the same after checking the machine for problems. consulting with Jux.
12. Take the Container out and check temperature it shouldn't get to warm.
13. If there was material on the sides of the container during placing in the container spatula it and place in the bottom and repeat the mixing. Otherwise done.

9.2 EDX inspection of metal mesh materials

EDX of aluminium wire mesh

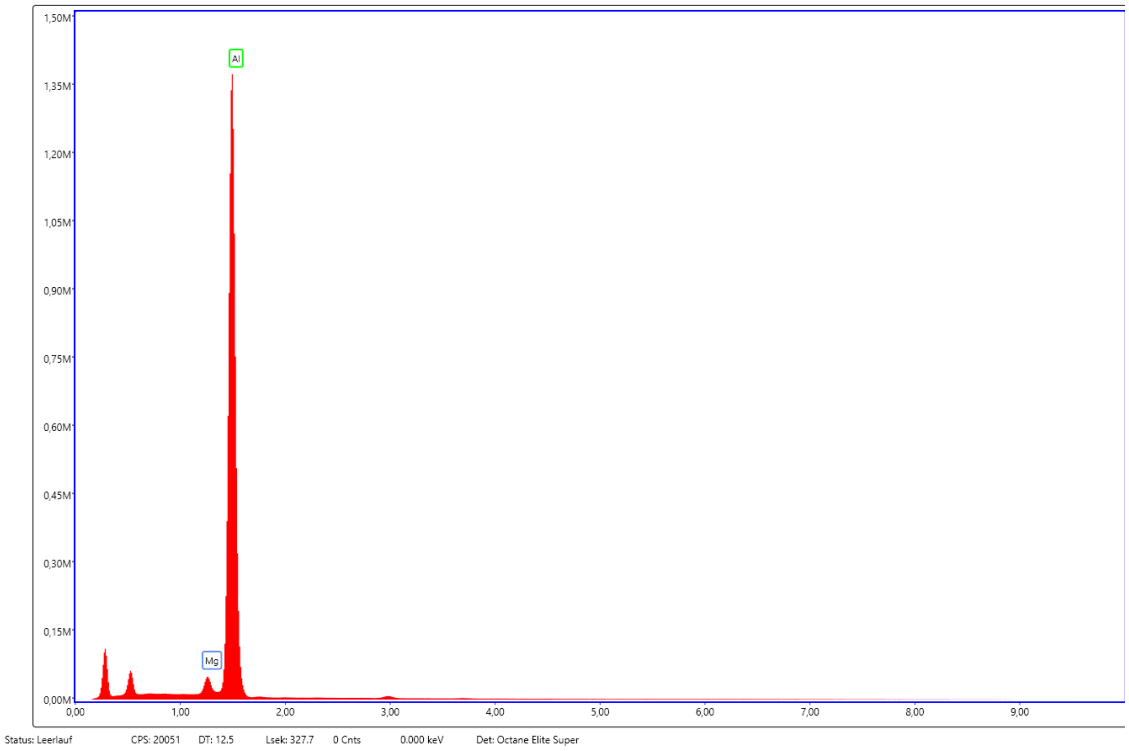

Element	Mass%	Atom%	Net. Int.	Error %	Kratio	Z	A	F
MgK	2.67	2.95	1009.60	2.70	0.0285	1.0406	0.9749	1.0522
AlK	97.33	97.05	31655.90	2.24	0.9568	0.9989	0.9841	1.0000

EDX of copper wire mesh

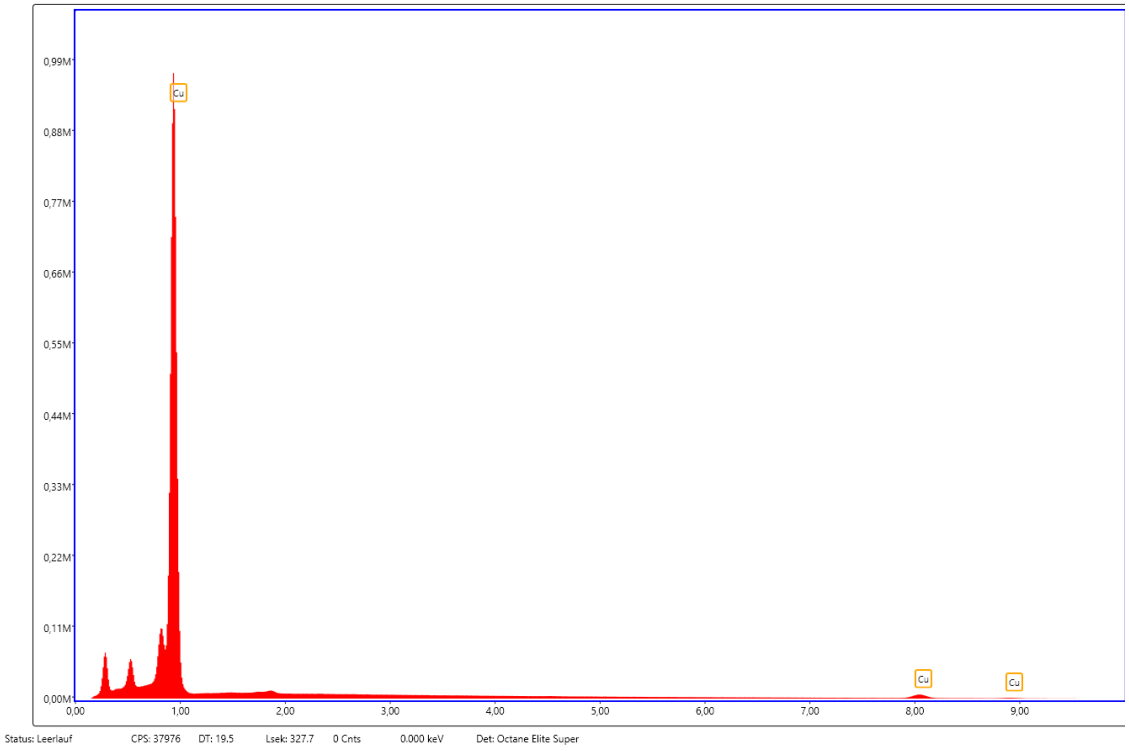

Element	Mass%	Atom%	Net. Int.	Error %	Kratio	Z	A	F
CuL	100.00	100.00	17885.00	1.95	1.0001	1.0000	1.0000	1.0000

EDX of Nickel-Chromium wire mesh

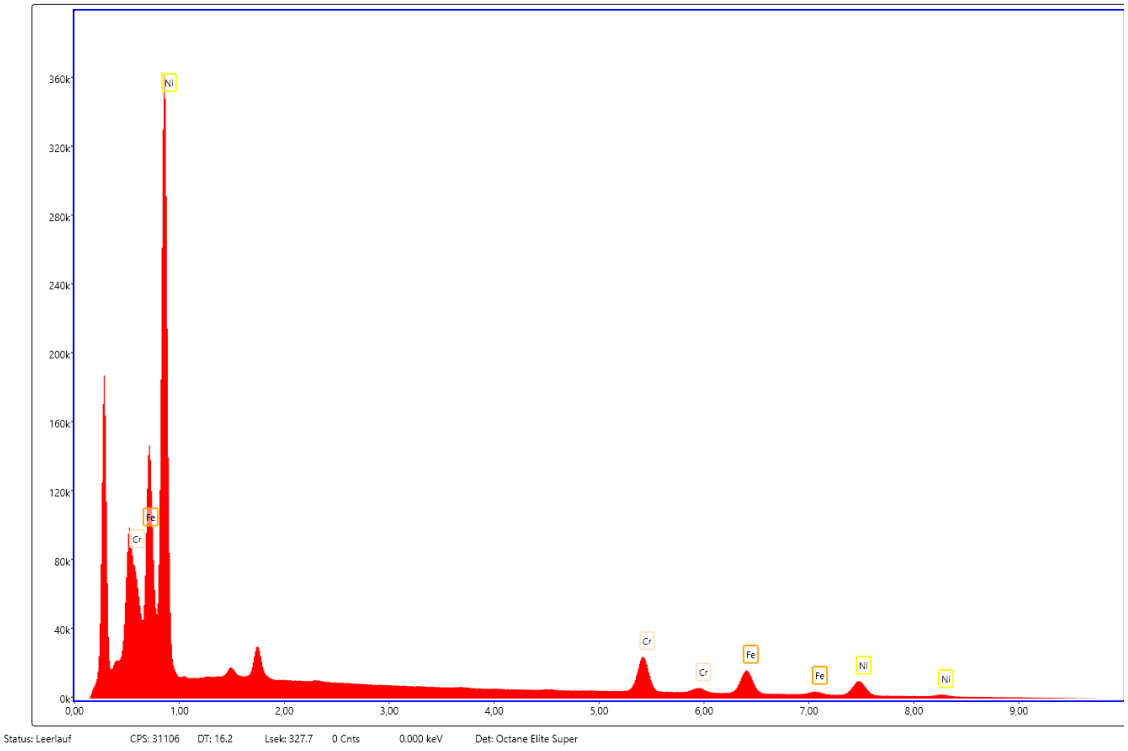

Element	Mass%	Atom%	Net. Int.	Error %	Kratio	Z	A	F
FeL	15.19	15.39	1395.00	4.70	0.1097	0.9912	0.7286	1.0000
NiL	61.79	59.56	5926.40	5.24	0.4171	1.0044	0.6720	1.0000
CrK	23.02	25.05	823.70	5.09	0.2465	1.0033	0.9955	1.0722

EDX of 304 stainless steel wire mesh

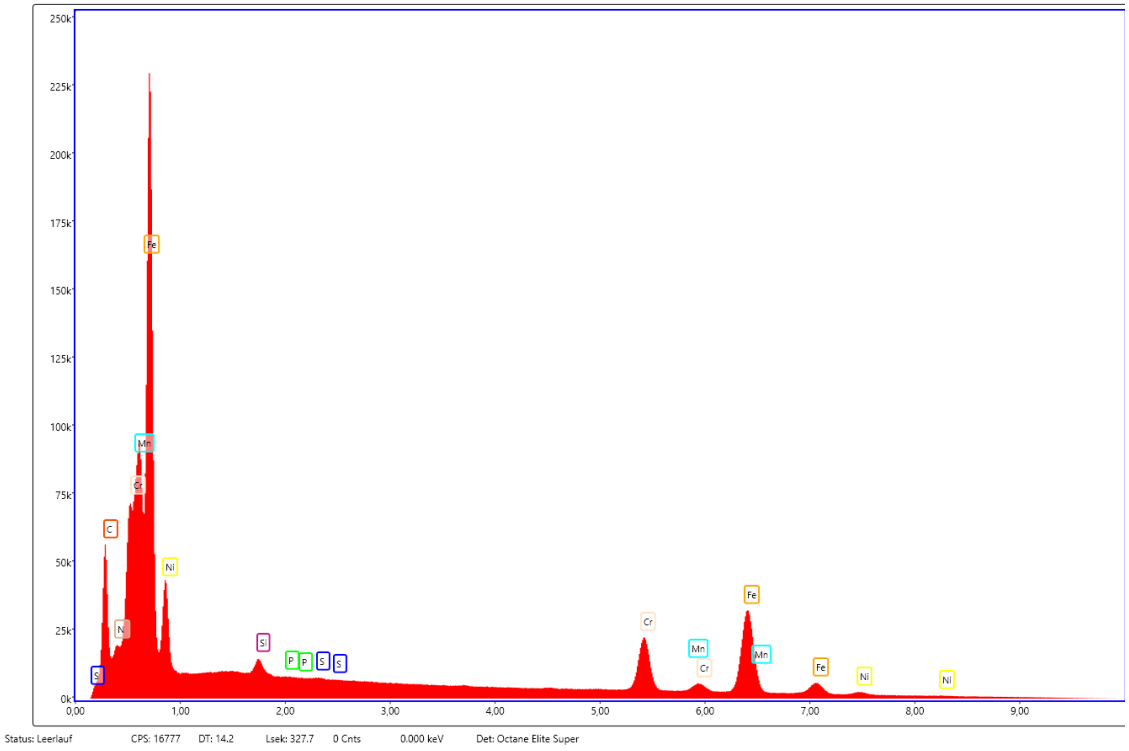

Element	Mass%	Atom%	Net. Int.	Error %	Kratio	Z	A	F
C K	7.75	26.76	752.00	8.41	0.0379	1.3548	0.3611	1.0000
N K	1.26	3.73	157.10	8.18	0.0074	1.3186	0.4454	1.0000
FeL	51.96	38.59	3169.60	5.81	0.3061	0.9609	0.6130	1.0000
NiL	9.43	6.66	483.90	7.73	0.0418	0.9735	0.4555	1.0000
SiK	0.79	1.17	157.90	5.96	0.0071	1.1547	0.7681	1.0031
P K	0.13	0.18	20.10	22.69	0.0012	1.1075	0.8392	1.0055
S K	0.17	0.22	25.40	13.50	0.0017	1.1276	0.8917	1.0090
CrK	27.22	21.72	780.30	5.07	0.2857	0.9635	0.9986	1.0908
MnK	1.28	0.97	24.50	19.10	0.0125	0.9402	0.9987	1.0410

9.3 Mixing nozzle with an extrusion width of 4mm

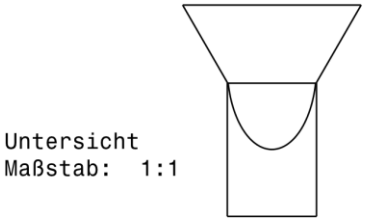

Untersicht
Maßstab: 1:1

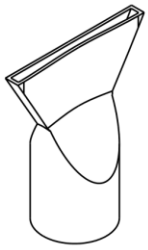

Isometrische Ansicht
Maßstab: 1:1

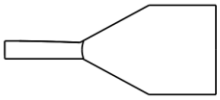

Seitenansicht rechts
Maßstab: 1:1

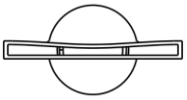

Vorderansicht
Maßstab: 1:1

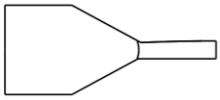

Seitenansicht links
Maßstab: 1:1

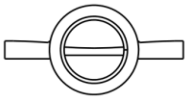

Rückansicht
Maßstab: 1:1

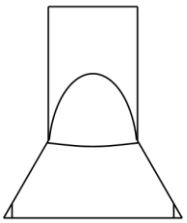

Draufsicht
Maßstab: 1:1

9.4 Fracture pattern of G2C samples

Fracture patterns for the G2C samples analysed in the two different loading mode regions.

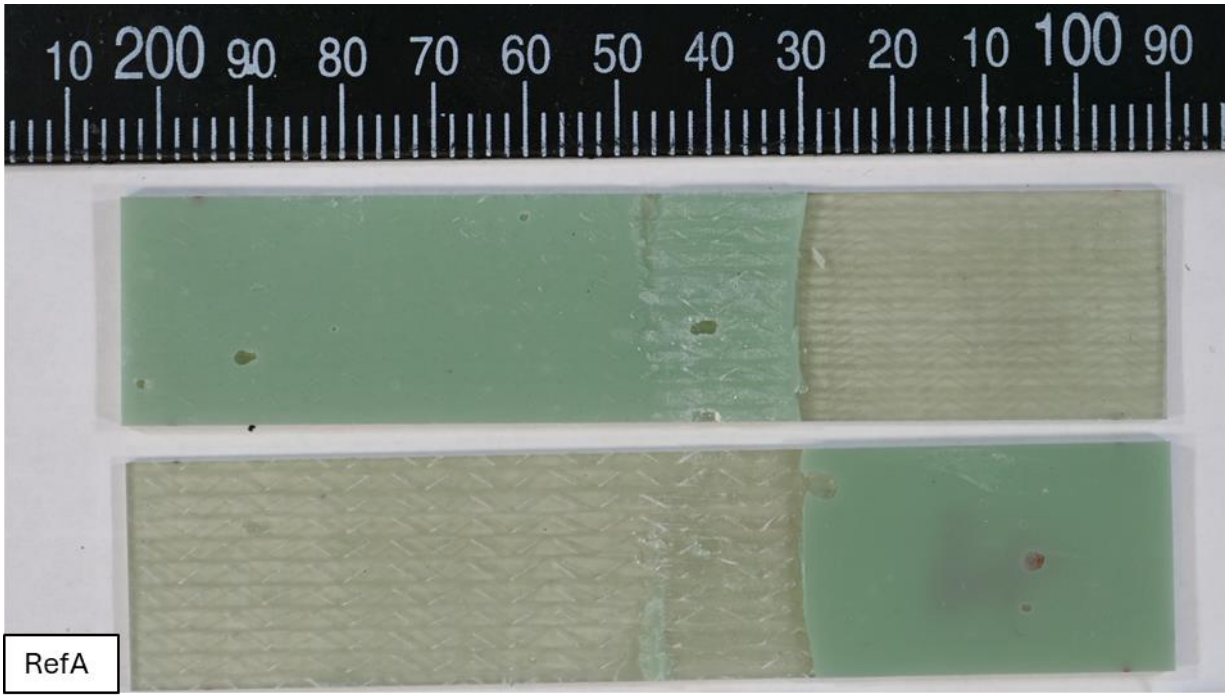

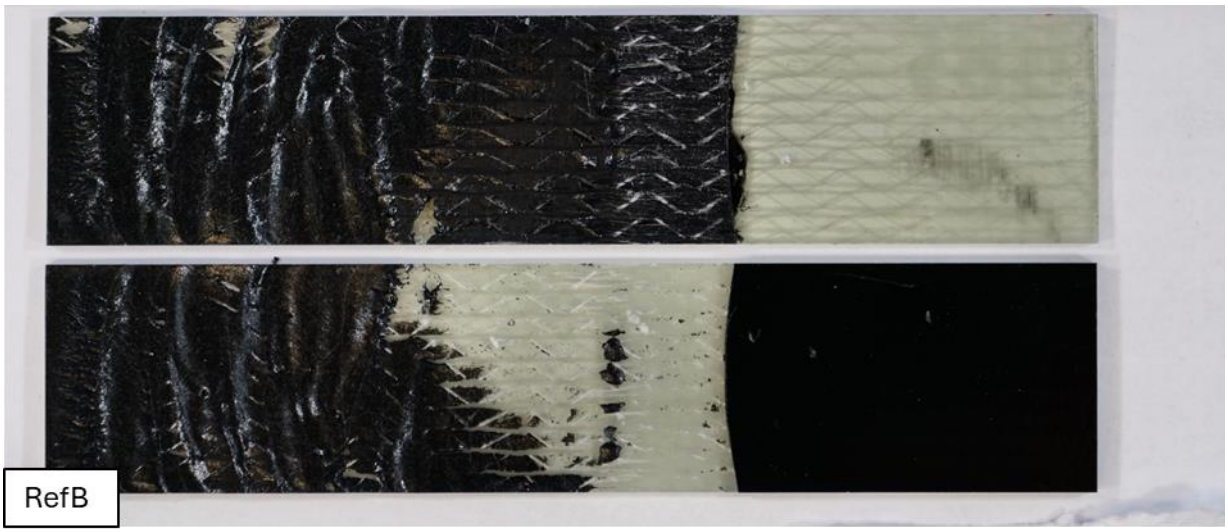

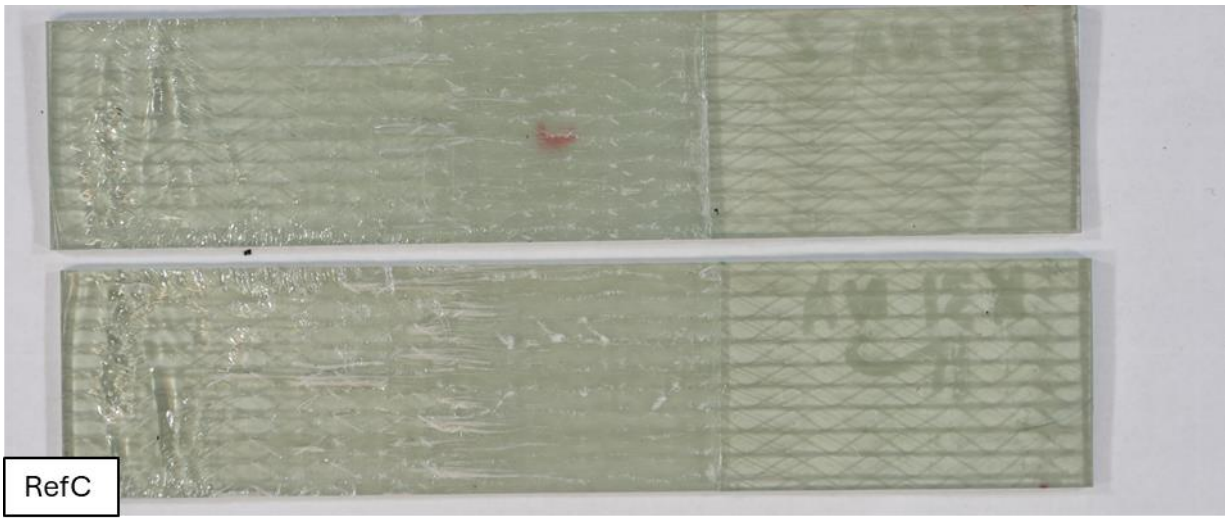

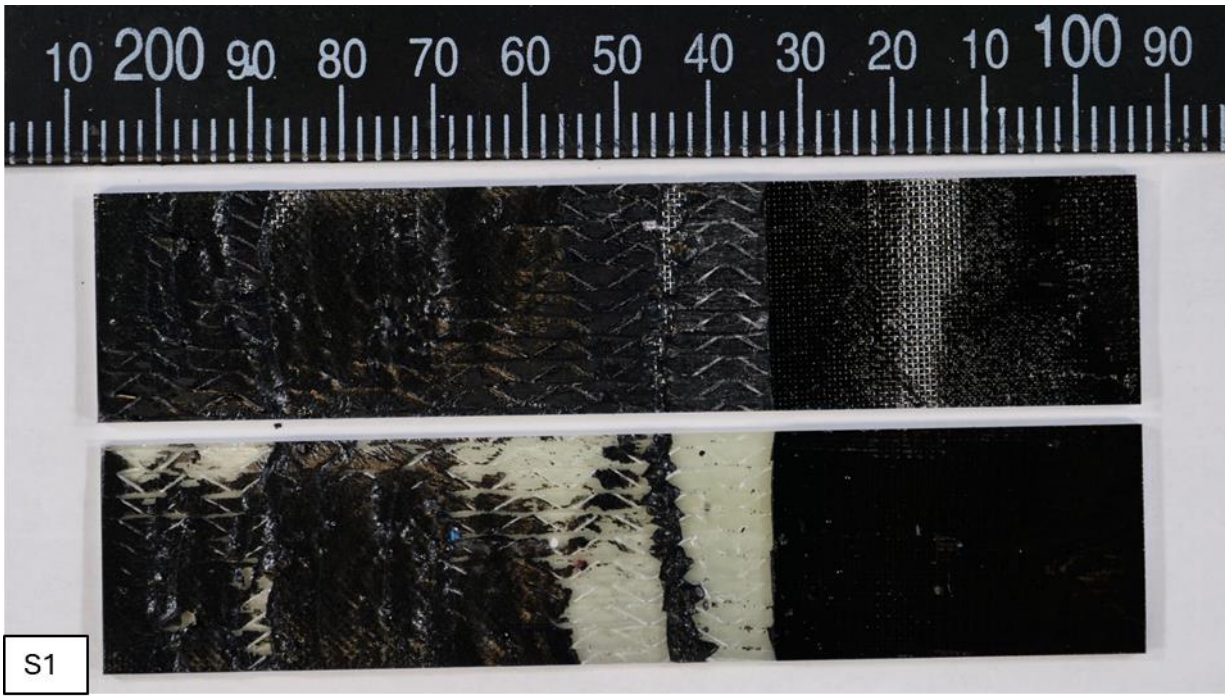
10 200 90 80 70 60 50 40 30 20 10 100 90
S1

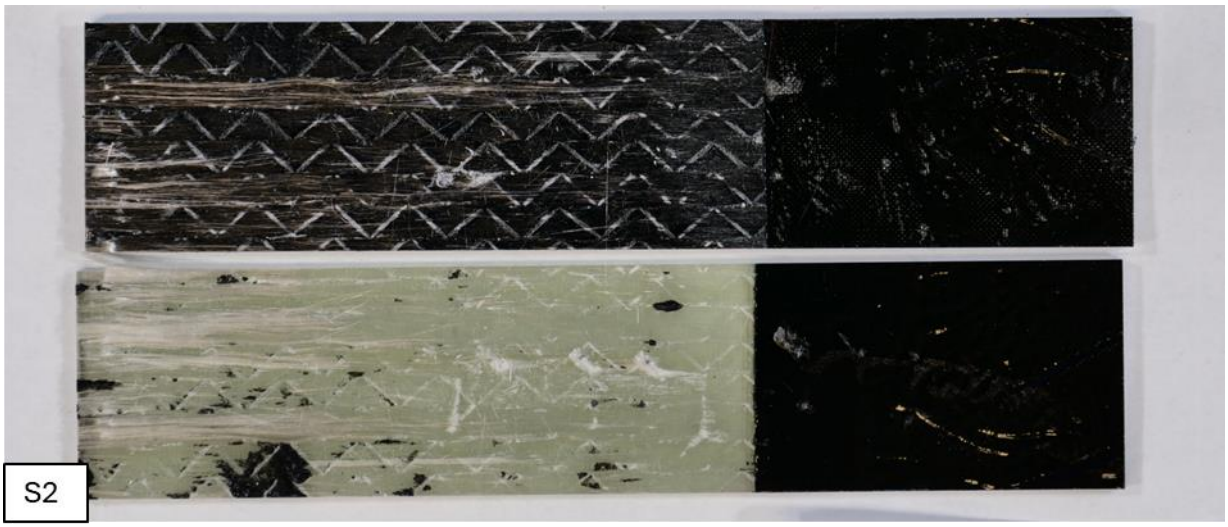
S2

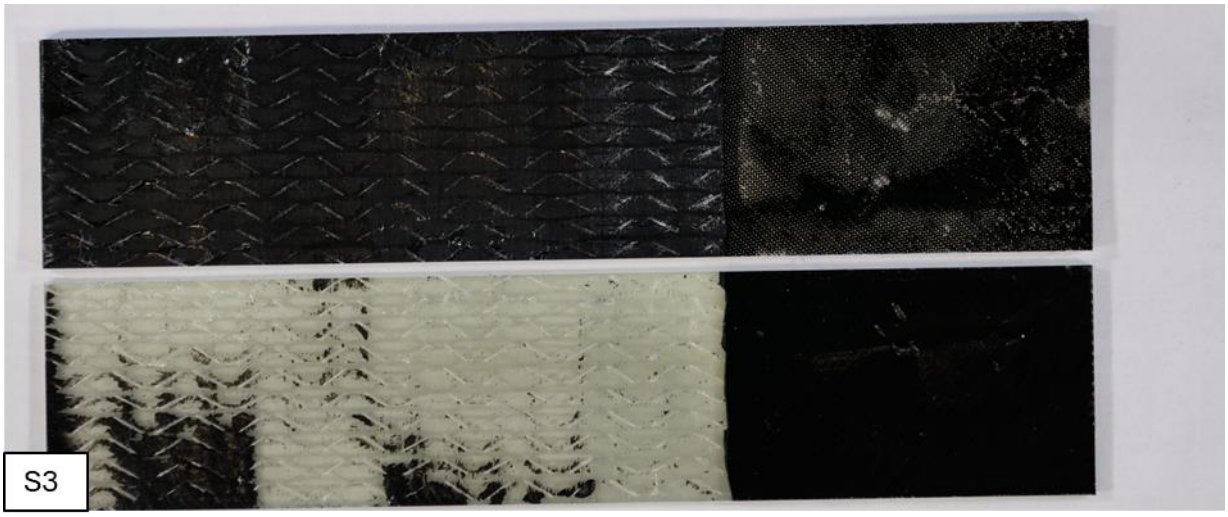
S3

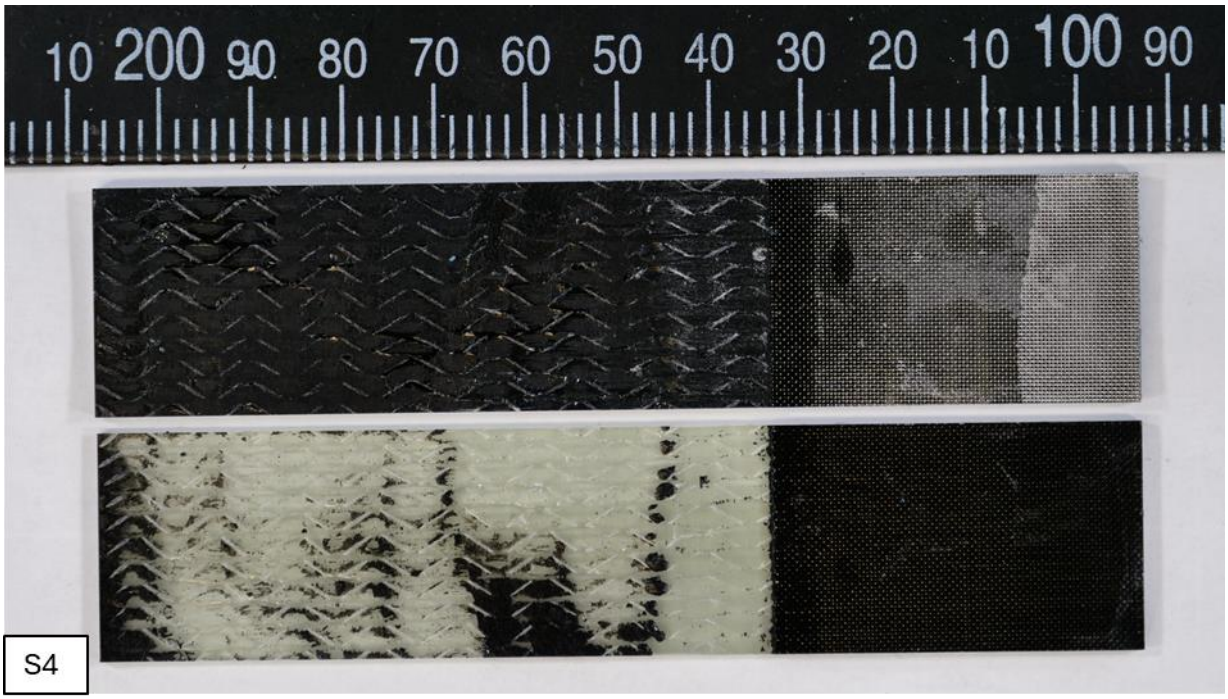
10 200 90 80 70 60 50 40 30 20 10 100 90
S4

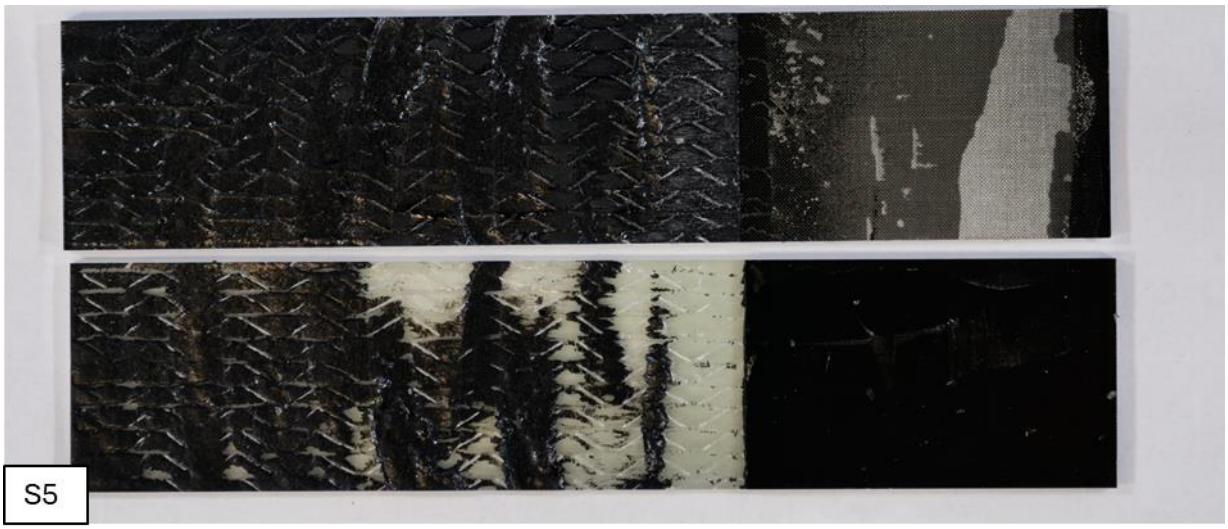
S5

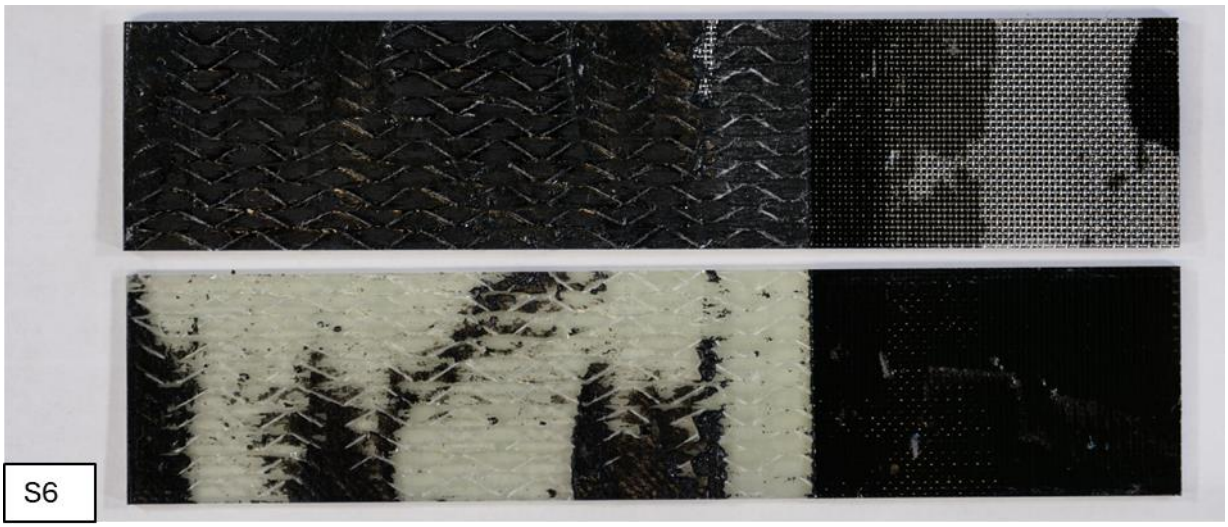
S6

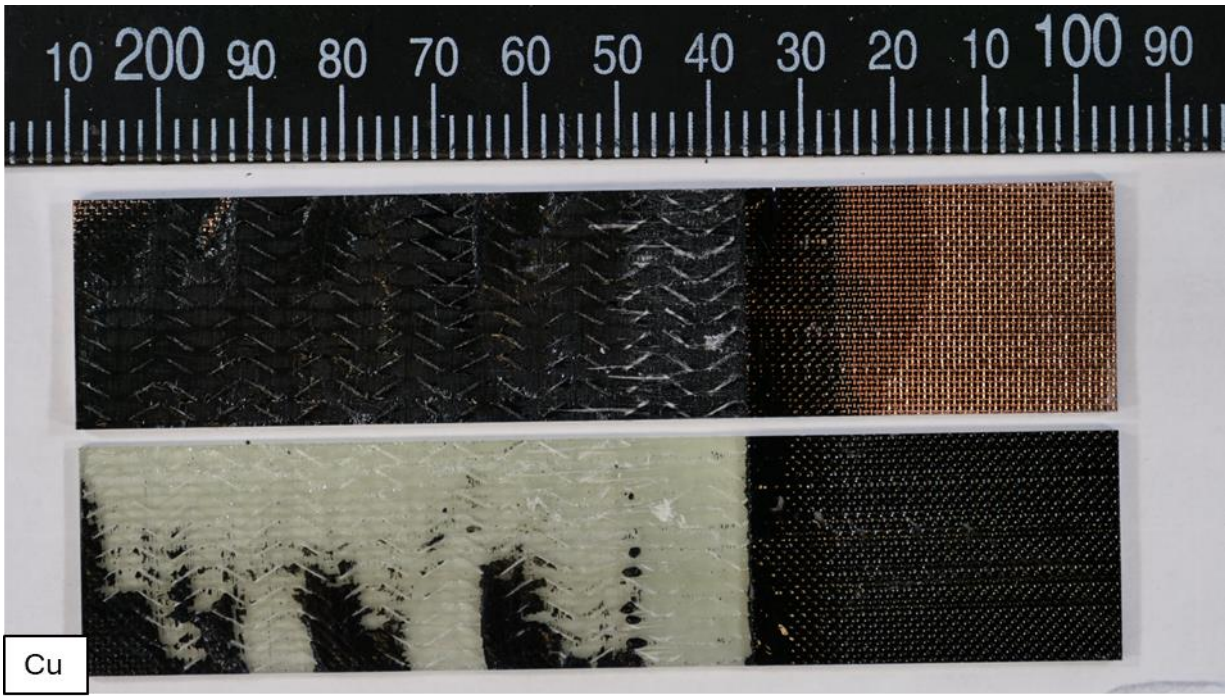

Two alumnium fracture patterns are shown due to the adhesive – mesh adhesive failure

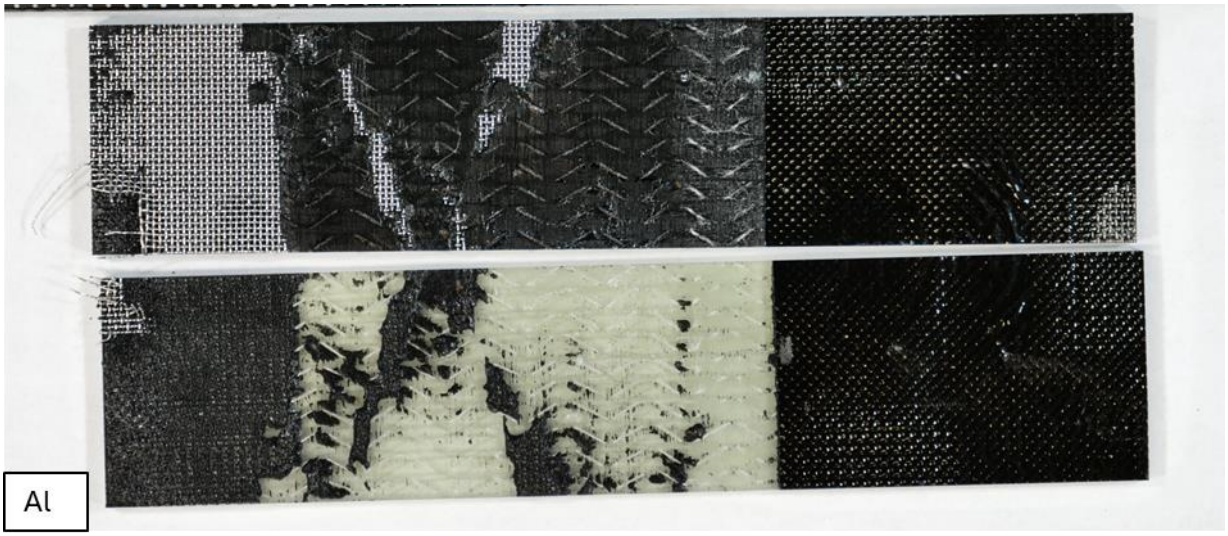

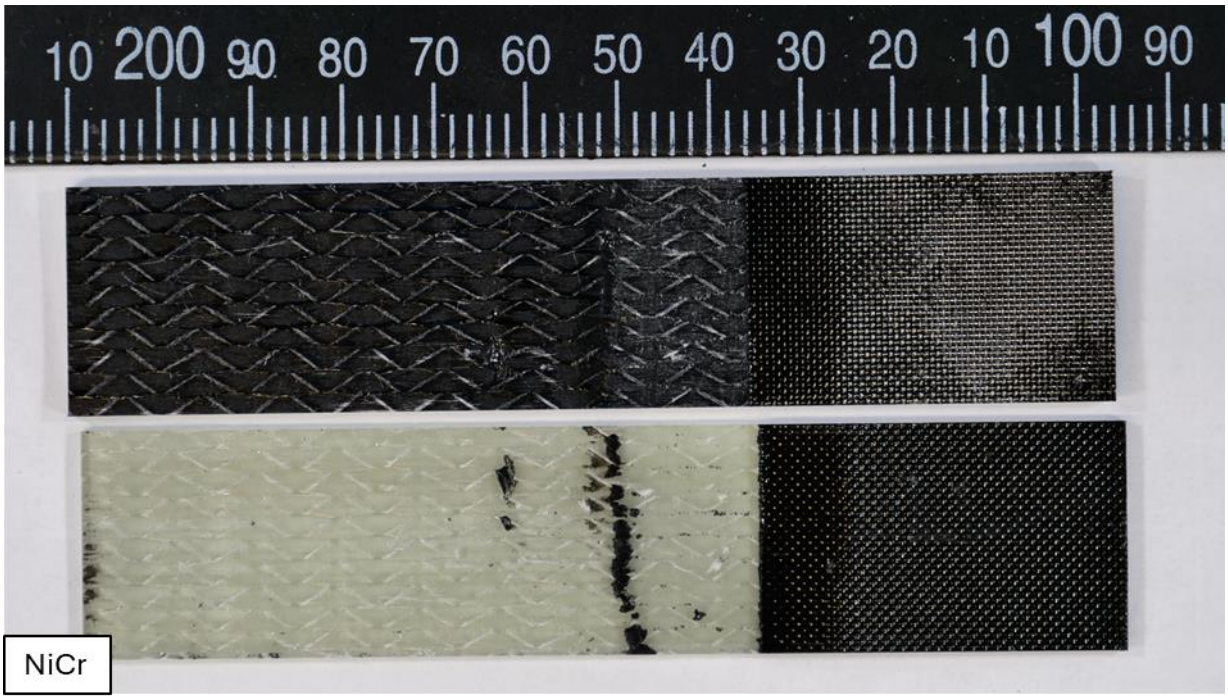

9.5 Maximum force development during dynamic SLS tests

Maximum force vs. Normalized Cycles for the RefA SLS series

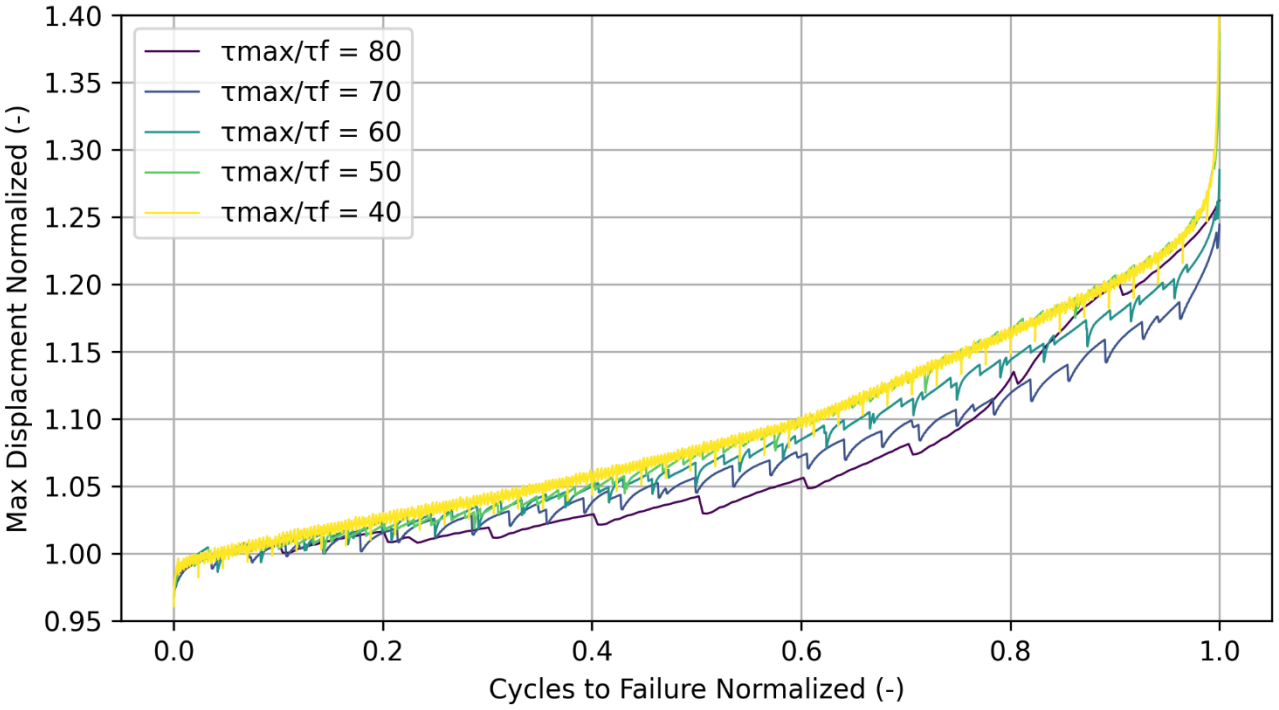

Maximum force vs. Normalized Cycles for the RefB SLS series

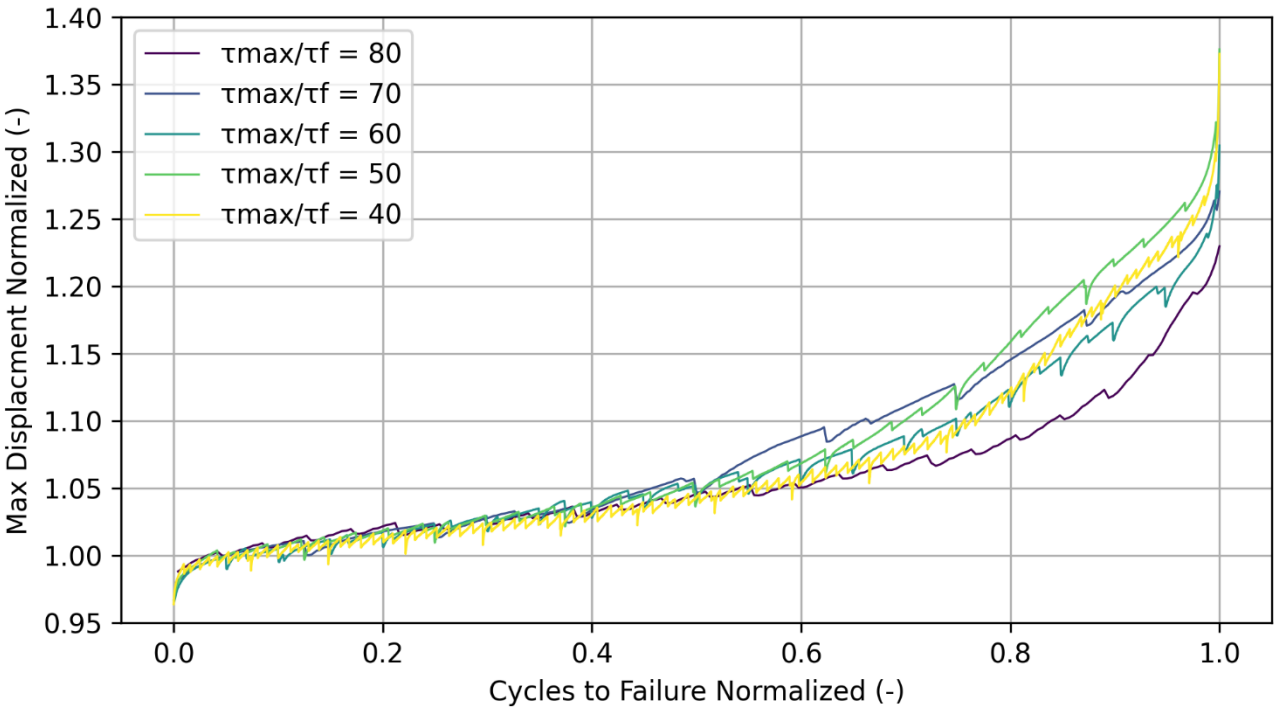

Maximum force vs. Normalized Cycles for the S6 SLS series